Magic-Angle-Spinning Solid-state NMR Studies of the Membrane Binding Heme Protein Nitrophorin 7 (NP7) from *Rhodnius prolixus*

Inaugural-Dissertation

zur

Erlangung des Doktorgrades der

Mathematisch-Naturwissenschaftlichen Fakultät

der Heinrich-Heine-Universität Düsseldorf

vorgelegt von

Sabu Varghese

aus **Kerala**

December, 2012

Aus dem Institut für Physikalische Biologie

der Heinrich-Heine Universität Düsseldorf

Gedruckt mit der Genehmigung der

Mathematisch-Naturwissenschaftlichen Fakultät der

Heinrich-Heine-Universität Düsseldorf

Referent: **Prof. Dr. Henrike Heise**

Koreferent: **Prof. Dr. Jörg Pietruszka**

Tag der mündlichen Prüfung: **19.12.2012**

Table of Contents

Abbreviations

1D, one-dimensional

2D, two-dimensional

3D, three-dimensional

BMRB, biological magnetic resonance data bank

C_α, alpha carbon atom

CP, cross-polarization

CPMAS, cross polarization magic-angle spinning

CPMG, Carr-Purcell-Meiboom-Gill pulse sequence

DEA/NO, diethylamonium (*Z*)-1-(*N*,*N*-diethylamino)diazen-1ium-1,2-diolate

DLS, dynamic light scattering

DOSY, diffusion ordered spectroscopy

DREAM, dipolar recoupling enhancement by amplitude modulation

FWHM, full-width at half-maximum

HSQC, heteronuclear single quantum correlation

ImH, imidazole

INEPT, insensitive nuclei enhanced by polarization transfer

INEPTMAS, insensitive nuclei enhanced by polarization transfer magic angle spinning

INEPT-TOBSY insensitive nuclei enhanced polarization transfer-through bond correlation spectroscopy

kDa, kilo Dalton

MDa, mega Dalton

MALDI MS, matrix-assisted laser desorption/ionization mass spectrometry

MAS, magic-angle spinning

NP1–4, nitrophorins 1–4 from *Rhodnius prolixus*

NP7, nitrophorin 7 from *Rhodnius prolixus*

NO, nitric oxide

PCS, pseudo contact shift

PC/PS, phosphatidyl choline/phosphatidyl serine

PRE, paramagnetic relaxation enhancement

PDSD, proton driven spin diffusion

RMSD, root-mean-square deviation

SPC-5, supercycled POST-C5

SPINAL, small phase incremental alteration

SQ-DQ, single quantum-double quantum

ssNMR, solid-state nuclear magnetic resonance

$T_{1,}$ spin-lattice relaxation time

$T_{1ir,}$ spin-lattice relaxation time measured by inversion-recovery

$T_{2,}$ spin-spin relaxation time

TOBSY, total through bond correlation spectroscopy

TPPM, two-pulse phase-modulation

[U-^{13}C,^{15}N\(K,V)]NP7, ^{13}C and ^{15}N labeled NP7 with Lys and Val in natural abundance

[U-^{13}C,^{15}N\(K,F,Y)]NP7, ^{13}C and ^{15}N labeled NP7 with Lys, Phe, and Tyr in natural abundance

Abstract

The nitrophorins (NPs) comprise a group of NO transporting ferriheme *b* proteins found in the saliva of the blood sucking insect *Rhodnius prolixus*. In contrast to other nitrophorins (NP1-4), the recently identified membrane binding isoform NP7 tends to form oligomers and well-ordered aggregates at higher concentrations in solution. Hence, we used solid-state NMR (ssNMR) to investigate structural and dynamical insights from the NP7 aggregates and membrane bound NP7. The two electronic spin states with $S = ½$ and $S = 0$ at the ferriheme iron can be generated by the complexation with imidazole and NO, respectively. Spectral overlapping in homo- and hetero-nuclear correlation spectra was minimized by two different reverse labelling approaches. The ssNMR spectra of both forms are well resolved and identical. Comparison of the spectra of the two electronic spin states allowed the determination of paramagnetically shifted cross peaks due to pseudocontact shifts (PCS) which assisted in assigning of residues close to the heme center. Importantly, the ssNMR spectra demonstrate that aggregation does not affect the protein fold. Furthermore, INEPT-TOBSY spectra allowed the identification of certain highly dynamic residues in the NP7 aggregates. The ssNMR spectra of liposome bound NP7 and the aggregates were almost identical, indicating that overall structure of the NP7 is almost the same in both sample states. The highly dynamic residues observed in the NP7 aggregates are found to have significant influence in molecular recognition and membrane binding. The NP7-membrane interaction is mainly mediated by the rear end of the heme pocket and is in good agreement with the previous reports on NP7-membrane interaction studies. Overall, this study demonstrates that ssNMR can be used as an important tool to gain structural insight into the interaction between NP7 and phospholipid membranes and the consequences on the protein structure.

Zusammenfassung

Die Nitrophorine (NPs) sind eine Gruppe von Stickstoffmonoxid (NO)-transportierenden Ferrihäm *b*-Proteinen, die im Speichel des Blut-saugenden Insekts *Rhodnius prolixus* vorkommen. Im Vergleich zu anderen NPs (NP1-4) bildet die kürzlich identifizierte Isoform NP7 bei höheren Konzentrationen immer hochmolekulare Oligomere und Aggregate. Daher verwendeten wir Festkörper-NMR, um strukturelle und dynamische Erkenntnisse aus den NP7-Aggregaten und Membran-gebundenem NP7 zu gewinnen. Die beiden elektronischen Spinzustände mit $S = ½$ und $S = 0$ des $Fe^{(III)}$ der Ferrihäm-Gruppe können durch die Komplexierung mit Imidazol und NO hergestellt werden. Spektrale Überlappung in homo- und heteronuklearen Korrelationsspektren wurde durch zwei unterschiedliche Ansätze zur reversen Isotopenmarkierung minimiert. Die NMR-Spektren der beiden Formen sind gut aufgelöst und identisch. Der Vergleich der Spektren in beiden elektronischen Spinzuständen erlaubt die Bestimmung der Aminosäurereste in der Nähe des Häm-Zentrums anhand von Pseudokontakt- Verschiebungen (PCS). Die NMR-Spektren zeigen, dass die Aggregation die Proteinfaltung nicht beeinflusst. Das INEPT-TOBSY-Spektrum ermöglicht die Identifizierung von bestimmten hochdynamischen Resten in den NP7-Aggregaten. Die NMR-Spektren von Liposom-gebundenem NP7 und von NP7-Aggregaten waren fast vergleichbar, was darauf hindeutet, dass die allgemeine Struktur von NP7 gut erhalten und fast die gleiche in beiden Probenzuständen ist. Das Vorhandensein hochdynamischer Reste in den NP7-Aggregaten hat außerdem einen Einfluss auf die molekulare Erkennung sowie auf die Bindung an die Membran. Die NP7-Membran-Interaktion wird hauptsächlich durch das hintere Ende der Häm-Bindungstasche vermittelt, was in guter Übereinstimmung mit früheren Berichten über die NP7-Membran-Interaktion ist. Insgesamt zeigt die Studie, dass Festkörper-NMR als robustes Werkzeug zur Gewinnung struktureller Informationen auf atomarer Ebene eingesetzt werden kann und zum Verständnis der NP7-Phospholipidmembran-Interaktion und deren Einfluß auf die Proteinstruktur beiträgt.

List of Figures

List of Tables

1 General Introduction

1.1 Structural biology and solid-state NMR

In depth knowledge of three-dimensional (3D) structure and the conformational dynamics of biomacromolecules (for example, DNA, RNA, Proteins, and lipids) are of vital importance for understanding their underlying biological functions and the diseases associated with them. Among them, proteins characterize an extremely diverse class of organic biomacromolecules, and play a critical role in the process of structure-based drug design[1]. Structural biology has made significant contributions towards the understanding of the 3D structures and functions of bio-molecules using two most important biophysical methods such as single crystal X-ray diffraction (XRD) and Nuclear Magnetic Resonance (NMR).

XRD is a method of determining the arrangement of atoms within a crystal based on observing the scattered intensity by short wavelength electromagnetic radiation (X-rays) from a crystalline lattice and can provide information in atomic resolution. However, well-ordered and diffractable single crystals form one of the preliminary requirements for obtaining high resolution structures using XRD methods. As a result, it is eventually limited to macromolecular systems that show a high degree of long-range order. Even though it accounts for the vast majority of well resolved 3D structures in the Protein Data Bank (PDB)[2], its potential is severely limited due to the complexities in obtaining diffractable crystals from membrane-proteins, protein aggregates and fibrillar proteins. On the other hand, for bio-macromolecules that cannot be studied by XRD, solution-state NMR can be applied to gain atomic level structural and dynamical insights. However, one of the main limiting factors for studying biomacromolecules by solution-state NMR is associated to their molecular size, which limits the rate of Brownian tumbling for high

molecular weight proteins. As a result, structural calculations using solution-state NMR becomes increasingly difficult with increase in molecular weight, and has been restricted to low molecular weight biomolecular systems (<30 kDa). Even though solution-state NMR studies on proteins above the molecular weight of 30 kDa are feasible[3], they require specialized isotopic labeling schemes involving extensive deuteration and tailored pulse sequences like transverse-relaxation optimized (TROSY)[4] NMR methods.

Despite the success of XRD and solution-state NMR in solving the 3D structures of bio-macromolecules, a vast majority of biomolecular systems are not easily accessible by the above methods. The most significant class of such biomolecular systems includes high molecular weight protein aggregates, membrane proteins, fibrillar proteins (amyloid fibrils), protein-protein and protein-ligand complexes. Furthermore, protein misfolding and aggregation are connected to various neurodegenerative disorders (Parkinson's disease, Alzheimer's disease and Huntington's disease) where the protein undergoes a structural transition from native globular or unfolded conformation into well-ordered aggregates[5,6]. On the other hand, such "intricate" and demanding systems can be studied in atomic level details using solid-state NMR (ssNMR) spectroscopy[7-9]. ssNMR does not require the system under consideration to form crystalline or soluble samples, and can thus be applied to a diverse class of biomolecular systems including membrane proteins[9], precipitates[10], micro/nanocrystals[11], protein aggregates (prions, amyloid, etc)[7], transiently sedimented proteins[12], bacteriophages[13,14], silk fibers[15] and nucleic acids[16], just to mention a few among them. However, ssNMR spectra of such static samples generally lack resolution, consisting of broad resonances that emerge from individual crystal orientations. The resulting static spectra are generally referred to as "powder patterns" and arise due to the presence of strong anisotropic interactions (dipolar couplings & chemical shift anisotropy) which

are not averaged out by random molecular motions as in the case of solution-state NMR spectroscopy.

These problems arising from lack of resolution due to orientation dependent anisotropic interactions can be minimized by mechanically spinning the sample at magic angle (54.7°) with respect to the external magnetic field $\vec{B}_0$ and are commonly referred to as "magic angle spinning solid-state NMR" (MAS ssNMR)[17-19]. In this research work, we have mainly employed "MAS ssNMR" as the method of choice for gaining structural information and for overcoming the problems arising from poor spectral resolution and sensitivity.

1.2 Nitrophorins

Nitrophorins (nitro = NO, phorin = carrier) are a group of NO transporting *ferriheme b* proteins found in the saliva of blood sucking insect *Rhodnius Prolixus*[20]. These insects feeds on the blood of rodents and larger mammals, including humans and is found to be the vector of "Chagas disease[21]". The insect is commonly referred to as "kissing bug", and the saliva of the blood-sucking bug contains at least seven homologous nitrophorins, designated NP1 to NP7[20,21]. The insect expresses mainly four nitrophorins (NP1-4) in the adult phase and are labeled in the order of their abundance[20,21]. Recently, a novel isoform NP7 was identified in a cDNA library obtained from the salivary glands of *R. prolixus*[22-24]. NP1-4 are each about 20 kDa in size and a comparison of their sequences reveal 90% sequence similarity between NP1 and NP4 and 79% between that of NP2 and NP3[25]. Overall, the four nitrophorins display 38% sequence similarity[25]. The overall three-dimensional structures of all the NPs (NP1-4) determined using X-ray crystallographic methods are almost same and reveals a common lipocalin type fold[26]. Even though lipocalins are primarily characterized as transport proteins, they are also well-known for their wide range of functionalities, in which molecular-recognition forms a distinguishable

feature[27,28]. X-ray crystal structures of nitrophorins (NP1-4) from the *R. prolixus* reveal lipocalin-like eight-stranded β-barrel, three α-helices and two disulfide bonds, with heme inserted into one end of the barrel[25]. The heme iron is coordinated by a His residue, where the 6th coordination site is open for the coordination of various small ligands[20].

The biological function of the NPs is the storage, transport and delivery of NO from the insect saliva to the host tissue where NO acts as a vasodilator and a platelet aggregation inhibitor, both of which benefit the insect during feeding. Nitrophorins (NP1-4) are stored in the adult insect saliva at low pH, with NO bound to a ruffled heme cofactor. The radical NO (*in vivo*, $t_{½} \approx 100$ ms) is preserved through coordination to the heme iron inside the insect saliva[29]. When the bug saliva containing the NP7-NO complex is injected to the victim's tissue, the protein experiences a significant pH change when subjected from the acidic pH of the saliva (between 5 and 6) to that of the blood plasma (~7.4); consequently, the affinity for NO is decreased, so that NO release occurs in the host tissues[30]. Downstream binding of the released NO by soluble guanylate cyclase (sGC) results in vasodilation, reduced platelet aggregation and improved blood feeding for the insect[31]. The immune response due to the insect bite results in the release of histamine (Hm), which is released by the victim in response to tissue damage[32]. Once the NO is released, Hm occupies the 6th free coordination site of the iron resulting in anti histamine effects and reducing the inflammation[33]. To summarize, the insect bite is followed by a cascade of biochemical events in the victim's tissue which are mainly assisted by the NPs and opens a unique means of obtaining a blood meal.

1.3 Nitrophorin 7 and ssNMR

As mentioned in the previous paragraphs, another Nitrophorin (NP7) has been recently reported, which was found to be expressed in the earlier life stages of *R. prolixus.* Amino acids that were

conserved in NP1-4 were very much different from NP7, but showed approximately 60% similarity with that of NP2 and NP3[24]. NP7 was found to be unique, since it was found to bind to l-α-phosphatidyl-l-serine (PS) containing phospholipid membranes which was not observed in the case of other nitrophorins (NP1-4)[23,24]. NP7 has a high number of positively charged Lys residues and the majority of these residues are clustered at the protein's surface opposite to the heme pocket[23]. This positively charged surface of the NP7 enables it to bind to anionic phospholipids membranes such as phosphatidylserine with high affinity[23,24,34].

Even though a preliminary X-ray crystallographic analysis of NP7 has been very recently reported[35], high-resolution structural studies on NP7 have not yet been reported. When compared to other nitrophorins (NP1-4), solution-state NMR studies of NP7 were also not successful due to the formation of high molecular weight aggregates in solution[36,37]. It has been hypothesized that, in solution, dipolar charge-charge interactions between the NP7 molecules result in the formation of larger aggregates of various sizes with reduced molecular tumbling. The reduced molecular tumbling accelerated T_2 relaxation times and thereby broadening the lines beyond detection during solution NMR measurements[36,37]. This was further supported by dynamic light scattering (DLS) experiments, where the apparent hydrodynamic diameters of the wild-type NP7 were reported to be of the order of ~250−400 Å[36]. Hence ssNMR was used as the method of choice for gaining atomic level structural information from the high molecular weight aggregates of NP7 and for understanding the structural changes upon membrane binding.

1.4 Nuclear Magnetic Resonance (NMR): Origin of the signal

A method for measuring the nuclear magnetic moment in a molecular beam of lithium chloride (LiCl) was first reported by Rabi et al. in 1938[38]. Later this method was independently expanded to other states of matter by Purcell in the case of solid paraffin and by Bloch in the case of liquid

water[39,40]. Nowadays, Nuclear Magnetic Resonance (NMR) is used as a versatile and indispensible tool for investigating the structure and dynamics of molecules. Since all the three main subatomic particles (electrons, protons and neutrons) posses the intrinsic property of spin, most of the atomic nuclei also have a "spin" which is a quantum mechanical property. The number of available quantum states for a nucleus is determined by the nuclear spin quantum number I and is equal to (2I+1). In the absence of a static external magnetic field, these nuclear energy levels are degenerate. However, when a static external magnetic field is applied, these energy levels become non-degenerate and the splitting of the energy levels is called the Zeeman effect[41]. For example, in the case of spin-½ nuclei (relevant in this thesis), there can be only two possible values of m_z, +½ and -½ or traditionally called "α" and the "β" states[42,43]. The nuclear spin quantum number I is also accompanied by a magnetic moment, given as:

$$\vec{\mu} = \gamma \cdot \hbar \cdot \vec{I} \tag{1.1}$$

Where $\hbar$ is the Planck's constant (h divided by 2π), and the gyromagnetic ratio γ is an isotope-specific constant which relates the nuclear spin to the magnetic moment of the nucleus. In the presence of a static external magnetic field, the nuclear magnetic moments couple with the external magnetic field, described by the Zeeman Hamiltonian,

$$\hat{H}_Z = -\vec{\mu} \cdot \vec{B}_0 = -\gamma \cdot \hbar \cdot \vec{I} \cdot \vec{B}_0 = -\gamma \cdot \hbar \cdot m_Z \cdot \left|\vec{B}_0\right| \tag{1.2}$$

The energy difference between two nuclear spin states (ΔE) can therefore be given as:

$$\Delta E = \gamma \hbar B_0 = h\nu_L \tag{1.3}$$

In the above equation, ν_L is the Larmor frequency expressed in Hertz. Transitions between the nuclear spin states are induced by irradiating the ensemble of nuclear spins using radio-frequency (RF), and thereby satisfying the resonance condition[42,43].

At equilibrium, the net magnetization vector lies along the direction of the applied static external magnetic filed $B_{0,}$ and is called as the equilibrium magnetization M_z which equals M_0. A simple 1-pulse (90° pulse) NMR experiment involves the rotation of the equilibrium magnetization M_z into the transverse plane (x-y plane) by a short RF-pulse and detecting through a RF-receiver coil aligned in the x-y plane. The oscillating electric current induced by the precessing transverse (x-y plane) magnetization is called the free-induction decay (FID). The FID is a time dependent signal which is later digitized and Fourier transformed into the frequency domain NMR spectrum. The laws of motion governing the magnetization vector components were derived by Felix Bloch and are called Bloch equations[40]. The Bloch equations are characterized by longitudinal (T_1) and transverse (T_2) relaxation time constants. The spin-lattice relaxation rate ($R_1=1/T_1$) describes the recovery of the longitudinal magnetization to thermal equilibrium, whereas the spin-spin relaxation rate ($R_2=1/T_2$) describes the decay of the transverse magnetization to zero. In the case of solution-state NMR, T_1 is greater than or equal to T_2. In the case of rigid solids, T_2 values are shorter when compared to the longer T_1 values which results in broadening of the lines. Furthermore in rigid solid samples, orientation dependent anisotropic interactions are not averaged out due to the lack of molecular tumbling, and thereby result in additional source for line broadening.

1.5 Solid-state NMR

Sine ssNMR deals with systems that have reduced or no molecular mobility, the spectra obtained from static samples are always broadened due to the influence of orientation dependent anisotropic interactions such as chemical shift anisotropy (CSA) and dipolar couplings as described in the following sections.

1.5.1 Chemical shift anisotropy (CSA)

Depending on the local symmetry at the nuclear site, the magnitude of the chemical shift will vary as a function of the orientation of the molecule with respect to the external magnetic field. This orientation dependence of the chemical shift is referred to as chemical shift anisotropy (CSA)[44]. For samples lacking molecular tumbling motion as in the case of solids, the observed chemical shift in an NMR spectrum is the sum of isotropic and anisotropic contributions and is given as,

$$\delta_{obs} = \delta_{iso} + \sum_{k=1}^{3} (3\cos^2 \theta_k - 1) \cdot \delta_{kk} \qquad 1.4$$

Where, θ_k is the angle between the k^{th} main axis of the tensor and the direction of the magnetic field. Principal components of the chemical shift tensor (δ_{11}, δ_{22}, δ_{33}) can be expressed in terms of the magnitude of the interaction, based on the parameters of isotropic chemical shift (δ_{iso}), reduced anisotropy (δ), and asymmetry (η) as given as,

$$\delta_{iso} = \frac{(\delta_{11} + \delta_{22} + \delta_{33})}{3} \qquad 1.5$$

$$\delta = \delta_{33} - \delta_{iso} \qquad 1.6$$

$$\eta = \frac{\delta_{22} - \delta_{11}}{\delta_{33} - \delta_{iso}} \qquad 1.7$$

In the standard convention, the principal components of the chemical shift tensor, (δ_{11}, δ_{22}, δ_{33}), are labeled according to the IUPAC rules[45], such that,

$$\delta_{11} \geq \delta_{22} \geq \delta_{33} \qquad 1.8$$

Different molecular orientations in NMR can cause different electronic shielding to the observed nuclei. In a non-oriented sample, where each orientation occurs with equal probability, a broad powder pattern is obtained (fig. 1.1). In the case of isotropic liquids, fast molecular tumbling results in the motional averaging of anisotropic interactions and the observed chemical shift is the average of the three the principal components. As a result, the spectra obtained from the

solution-state NMR are well resolved with narrow line shapes, while CSA contributes significantly to the large line-widths in the case of static ssNMR spectra of rigid solids.

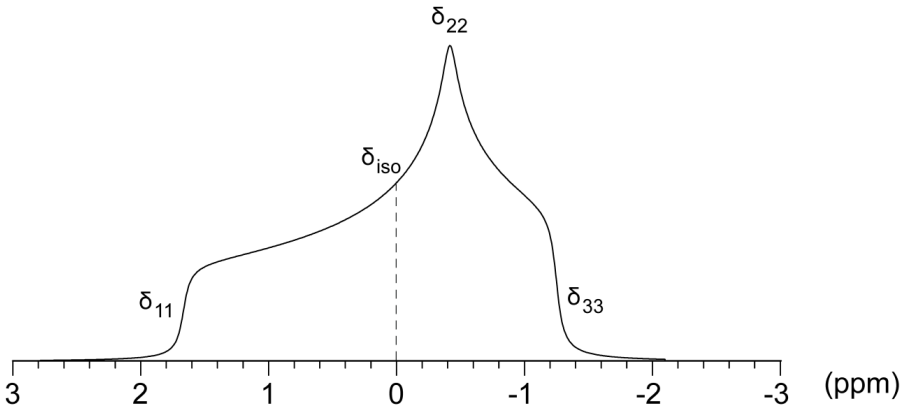

Fig. 1.1: Typical static-powder ssNMR spectra simulated at a ^{1}H Larmor frequency of 600 MHz using isotropic chemical shift of δ_{iso} = 0 ppm, δ_{aniso} = 1.6 ppm, and η= 0.5 corresponding to chemical shift principal elements of δ_{11} = 1.6 ppm, δ_{22} = -0.4 ppm, and δ_{33} = -1.2 ppm. Simulations were done using the Simpson[46] simulation program.

1.5.2 Dipolar couplings (Through-space interactions)

Nuclear spins posses a magnetic moment and interaction of these spins through space is called dipolar coupling and the dipolar interaction Hamiltonian can be expressed as,

$$\hat{H}_{dd} = -\left(\frac{\mu_0}{4\pi}\right)\frac{\gamma_I\gamma_S\hbar}{r^3}\left[A+B+C+D+E+F\right] \qquad 1.9$$

where, A, B, C, D, E, and F are called the dipolar alphabet,[44] γ_I and γ_S are the gyromagnetic ratios of the nuclear spins *I* and *S* respectively. Since the Zeeman interaction is larger than the dipolar interactions, only terms that commute with Zeeman interactions remain and are not truncated, forming the "static" or secular part of the dipolar Hamiltonian. The terms *C*-*F* forms the non-secular part of the dipolar Hamiltonian and are essentially zero and can be neglected. For

heteronuclear spins, the A term commutes with the Zeeman Hamiltonian and the dipolar Hamiltonian simplifies as[44]

$$\hat{H}_{dd}^{hetero} = -d(3\cos^2\theta - 1)\hat{I}_z\hat{S}_z \tag{1.10}$$

In the case of homonuclear spin pairs, both the terms A and B contribute to the spectra due to the presence of "flip-flop" operator in B and the dipolar Hamiltonian can be written more succinctly as[44]

$$\hat{H}_{dd}^{homo} = -d\frac{1}{2}(3\cos^2\theta - 1)\left[3\hat{I}_z\hat{S}_z - \hat{I}\cdot\hat{S}\right] \tag{1.11}$$

Where $\hat{I}\cdot\hat{S} = \hat{I}_x\hat{S}_x + \hat{I}_y\hat{S}_y + \hat{I}_z\hat{S}_z$ and d is the dipolar coupling constant (rad s^{-1}) and is given as

$$d = \hbar\left(\frac{\mu_0}{4\pi}\right)\frac{\gamma_I\gamma_S}{r^3} \tag{1.12}$$

From the above equation it can be seen that the magnitude of the dipolar coupling is directly proportional to the product of the gyromagnetic ratios of the coupled nuclei and the inverse third power of the distance between them. Hence, dipolar couplings between two nuclei can be used as constraints for molecular structure determination and also serve as a means of polarization transfer between the nuclei. For an isolated spin pair in a single crystal, the dipolar interaction induces two transitions for one orientation to the external magnetic field. But for powder samples with different crystallite orientations, an envelope of all possible contributions results in the so called "Pake doublet[47]" pattern (fig. 1.2).

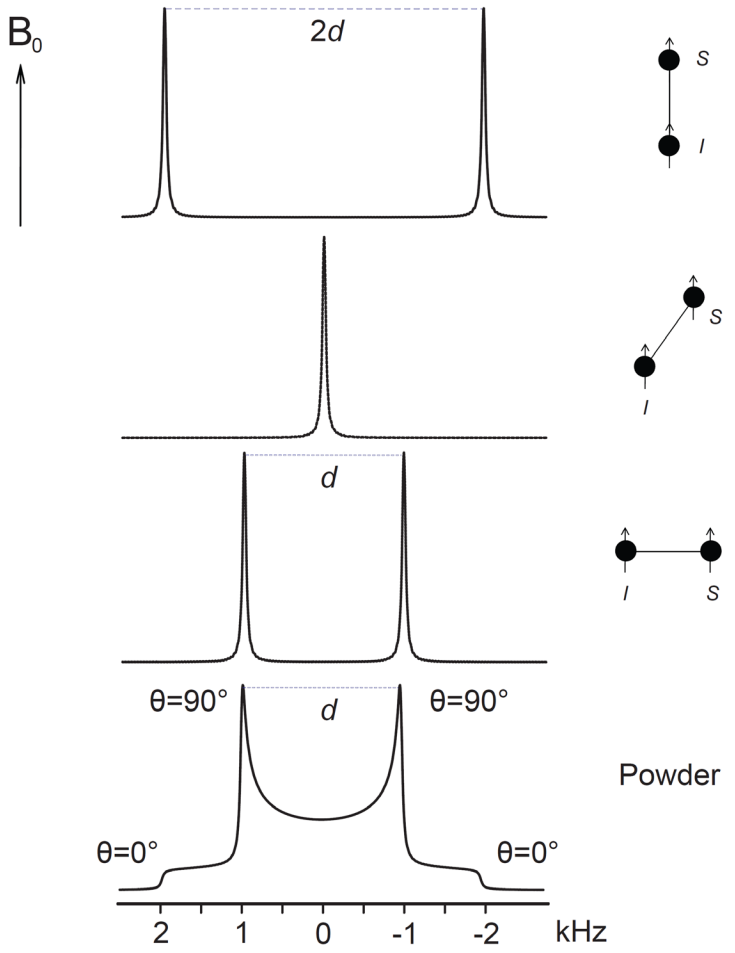

Fig. 1.2: Simulated NMR spectra for two spins *I* and *S* which interact with one another by the direct dipolar interaction. From top to bottom: simulated spectra for three orientations of the internuclear vector in the applied magnetic field $\vec{B}_0$ for θ=0°, 54.7° (magic angle) and 90° respectively. The bottom spectrum is the "Pake powder pattern" which results from a sum of spectra of individual crystallites which are randomly distributed in the sample. Simulations were done using the Simpson[46] simulation program using a dipolar coupling constant of 2000 Hz.

1.5.3 Basic techniques in ssNMR spectroscopy

Since all anisotropic interactions contain the angular term ($3\cos^2\theta$-1), where θ is the angle between the tensor main axis and the external magnetic field $\vec{B}_0$, the most efficient and robust method is to partially emulate the motional averaging effects by rapid spinning (1-60 kHz) of the solid NMR sample. In the following section, basic methods for gaining resolution and sensitivity in ssNMR are discussed, which were employed for the research work presented in this thesis.

1.5.4 Magic angle spinning (MAS)

In the case of solution-state NMR, angular dependent anisotropic interactions ($3\cos^2\theta$-1) are averaged out due to Brownian motion, resulting in well-resolved isotropic peaks. In the case of solid samples, the averaging effect is mimicked by mechanically spinning the sample at an angle θ as given as

$$\theta = \cos^{-1}\left(\sqrt{\frac{1}{3}}\right) = 54.74° \qquad 1.13$$

Spinning of a solid-state sample at an angle of 54.74º with respect to the external static magnetic field to $\vec{B}_0$ leads to a time-averaging of the anisotropic spin-interactions and is termed Magic Angle Spinning (MAS)[17]. Anisotropic interactions can only be efficiently averaged out if the MAS frequency (ω_r) is much larger than the magnitude of the anisotropic interaction. As a result, an isotropic peak can be observed in the resulting spectra as the anisotropic contributions are "spun" away. If the MAS rate is smaller than the anisotropic interaction, the resulting spectra are manifested by the presence of "spinning sidebands" (SSBs) (fig. 1.3). Since the isotropic chemical shift is a property of the nucleus due to its surrounding electronic environment, it remains at the same position at any given MAS frequency and can be identified by spinning the sample at various frequencies.

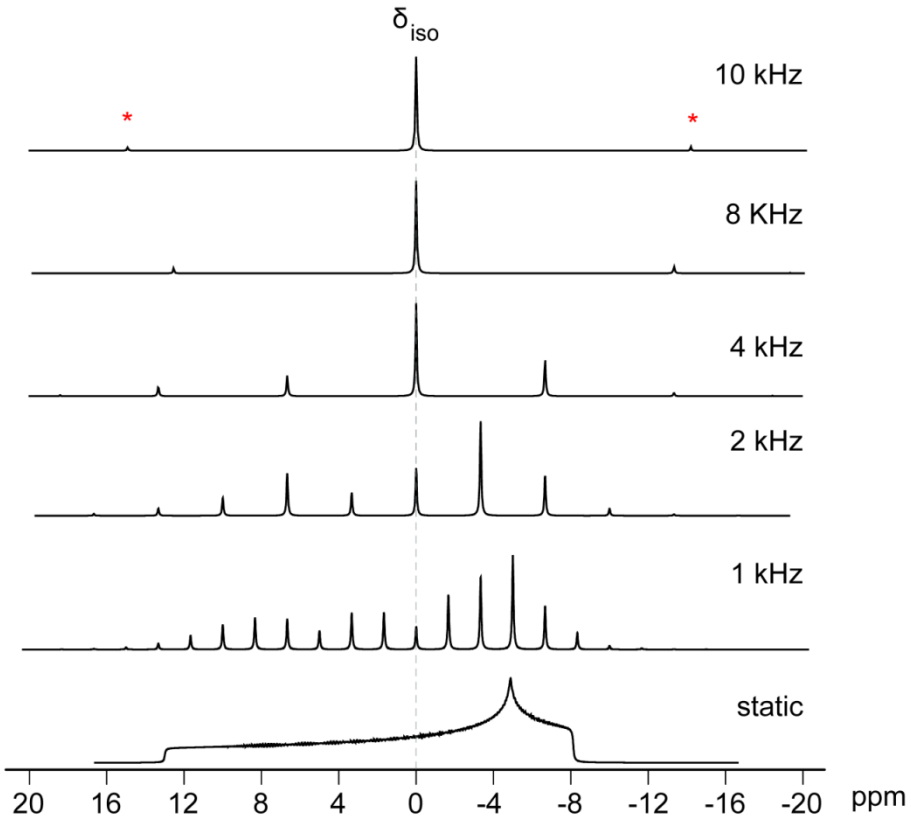

Fig. 1.3: Illustration of the averaging effect of chemical shift anisotropy (CSA) in ssNMR by means of magic angle spinning under static and increasing MAS frequencies (from bottom to top). Simulations were performed using the Simpson[46] simulation program using anisotropic chemical shift of δ_{aniso} = 13 ppm, and asymmetry η= 0.25 at a ^{1}H Larmor frequency of 600 MHz. The isotropic chemical shift at 0 ppm which remains unchanged irrespective of the MAS frequency is shown by a dotted grey line. First order spinning side bands from the spectrum obtained at a spinning frequency of 10 kHz is shown by red asterisks.

1.5.5 Cross-polarization (CP)

Biochemically relevant NMR nuclei such as ^{13}C (1.1%) and ^{15}N (0.03%) suffer from problems arising from low sensitivity in addition to their low gyromagnetic ratio. In ssNMR, sensitivity enhancement can be accomplished by polarization transfer mediated by dipolar couplings from

the abundant *I* spins (^{1}H) to the dilute spins *S* (^{13}C, ^{15}N) by a technique called cross-polarization (CP)[19,48]. Polarization transfer is possible when the nutation frequencies of both abundant (*I*) and dilute spins (*S*) are made equal by properly adjusting the RF fields so as to match the Hartmann-Hahn condition[49],

$$B_1^I \cdot \gamma_I = B_1^S \cdot \gamma_S \qquad 1.14$$

Where B_1^I and B_1^S are the RF field amplitudes of the *I* and *S* channels, γ_I and γ_S are the gyromagnetic ratios of the *I* and *S* spins respectively. CP in combination with MAS (CPMAS) along with high-power heteronuclear decoupling forms the basic building block for the most of the pulse sequences used in this research work. The advantages of CPMAS over direct excitation on dilute spins are (1) increased sensitivity as determined by the ratio of the gyromagnetic ratios of the *I* spins to that of the *S* spins, (2) relaxation delay between the scans can be chosen based on the T_1 of the *I* spins (^{1}H) rather than the T_1 of the dilute isotope. Since CP is based on heteronuclear dipolar couplings, any motions that may average dipolar couplings may also result in the reduced efficiency of polarization transfer and can be used to monitor molecular dynamics in solids[50].

1.5.6 Spin decoupling

Achieving high spectral resolution is an important prerequisite for the application of ssNMR to biological samples. Even though MAS is an efficient way to partially remove the anisotropic interactions, homonuclear and heteronuclear dipolar interactions are usually too high to be averaged out completely at the accessible MAS frequencies (1-60 kHz). Therefore in addition to MAS, heteronuclear spin decoupling is usually employed in ssNMR for gaining spectral resolution. In the case of a dipolar-coupled ^{1}H-^{13}C spins, the process involves applying continuous high power RF irradiation at the frequency of the proton resonance called Continuous

Wave (CW) irradiation. However, at high MAS rates, CW decoupling does not lead to better resolution, unless extremely high RF-fields are applied, which is not ideal for biological samples due to sample heating. The two-pulse phase-modulated (TPPM)[51] decoupling sequence was the first multiple-pulse decoupling method for solid organic samples under MAS that gave significant improvements in both line width and line intensity. A variation of this concept is the small phase incremental alteration (SPINAL),[52] which uses super cycles of a basic sequence with additional phase increments α and β and showed significant improvements in the offset behavior compared to TPPM in liquid crystalline samples. Even though several other improved decoupling methods have been developed and is in use, SPINAL is used as the method of choice for heteronuclear spin decoupling (^{1}H-^{13}C/^{15}N) in this research work.

1.5.7 Recoupling

Valuable structural information encoded as distance restraints from the dipolar couplings and electronic environment from the CSA are averaged out due to MAS. However, this information can be regained while retaining high resolution by employing the so-called *recoupling* method to recover the anisotropic interactions during the ssNMR experiment. The selective restoration of the dipolar interaction can be achieved mechanically (*rotational resonance*)[53], or by the application of *RF*-pulses. The *rotational resonance* (RR)[53,54] condition is achieved by adjusting the rotor frequency (ν_r) as a multiple (n) of the difference frequency of the isotropic chemical shift values ($\Delta\nu$) of two chemically different homonuclear spins.

$$n \cdot \nu_r = \Delta\nu = (\nu_1^{iso} - \nu_2^{iso}) \qquad 1.15$$

As a result, dipolar coupling between the nuclei is restored (via the 'flip-flop' term $I_{1+}I_{2-} + I_{1-}I_{2+}$ in the dipolar Hamiltonian), and 'line broadening' of the resonances at ν_1^{iso} and ν_2^{iso} is observed in addition to rapid oscillatory exchange of Zeeman magnetization. Dipolar

recoupling can also be achieved by the application of rotor synchronized RF-pulses and can be broadly classified as homo- and heteronuclear recoupling schemes. Among the homonuclear dipolar recoupling techniques, SPC-5 (supercycled POST-C5)[55] and DREAM (*d*ipolar *r*ecoupling *e*nhancement by *a*mplitude *m*odulation)[56,57] are mainly employed in this research work for reintroducing the dipolar couplings. The DREAM[56,57] experiment is an advanced, adiabatic version of the HORROR (homonuclear rotary resonance)[58] experiment. The most common technique used for heteronuclear recoupling and distance measurement is rotational-echo double resonance (REDOR)[59]. Irrespective of the methods employed, dipolar recoupling sequences can be successfully employed for the following applications, (1) determination of internuclear distances, (2) magnetization exchange, (3) determination of bond angles and torsional angles, (4) Excitation of multiple quantum coherences.

1.5.8 Spin diffusion

Spin diffusion[60] is a process in which spin polarization is propagated between equivalent spins of close proximity. During the process, the individual spins continually exchange energy with each other through the energy conserving *flip-flop* transitions of the Dipolar Hamiltonian. In a network of dipolar-coupled spins (^{1}H), homonuclear flip-flop transitions and fast exchange between energy quanta in a random fashion results in homogenous line broadening. As a result, proton NMR spectra of fully protonated biomolecular solids are broadened even under ultra-fast MAS frequencies (60 kHz). Proton-driven spin diffusion (PDSD)[61,62]under MAS is one of the basic methods to enable spin diffusion for nuclei with low gyromagnetic ratio (^{13}C) making use of a densely coupled proton network. It is also used as an important technique in ssNMR to obtain distance constraints in uniformly or specifically labeled biomolecules[10,63-65]. For short mixing times, the corresponding 2D ^{13}C-^{13}C correlation spectra is dominated by the presence of

intra-residual cross peaks, while inter-residual cross peaks can also be observed for longer mixing times. When compared to other pulse sequences, PDSD is found to have the following advantages. (1) it can be easily implemented, (2) RF-field requirements are low, and (3) reduced sensitivity to dipolar-truncation[55,66] effects[63].

1.5.9 *J*-couplings (Through-bond correlations)

The indirect magnetic interaction of nuclear spins with the help of bonding electrons is known as the indirect spin-spin coupling, or *J*-coupling. Since closely related to local electronic and nuclear environments, *J*-coupling interaction is a very useful tool for the determination of chemical structure. The presence of strong dipolar couplings (kHz) from the abundant nuclei masks the weaker *J*-couplings (Hz). However, the advent of high-frequency MAS and high-power proton homo- and heteronuclear decoupling has made it possible to observe and utilize *J*-coupling in solid samples. Homonuclear through-bond ^{13}C-^{13}C correlation is solids can be achieved by sequences of RF-pulses that are synchronized with the MAS rotor and applied to the sample during the mixing time of a standard 2D correlation experiment. Two classes of rotor-synchronized pulse sequences have been proposed and developed for the isotropic mixing designated as CN_n^v and RN_n^v sequences respectively[67-74]. In both cases the choice of the symmetry numbers *N*, *n* and *v* determine which interactions are retained in the lowest-order average Hamiltonian via a set of selection rules. In the presence of highly dynamic local motions, where orientation dependent anisotropic interactions are sufficiently averaged out, the combination of pulse sequences like refocused INEPT[75] and TOBSY (INEPT-TOBSY, *insensitive nuclei enhanced by polarization transfer–total through bond correlation spectroscopy*) could be employed in ssNMR for discriminating the rigid and flexible parts of the protein[76,77] and also has been applied in this research work.

1.6 Secondary chemical shifts & protein secondary structure

The resonance frequency of specific spins connected to the protein backbone is strongly correlated with the secondary structure of the protein[78,79]. After the backbone resonance assignments, the assigned resonance frequencies can be compared with their respective average ('random coil') chemical shift from Biological Magnetic Resonance Bank (BMRB)[80] to gain information about the secondary structure. The secondary chemical shifts (Δδ), are calculated based on the formula given as,

$$\Delta\Delta\delta_{C\alpha,C\beta} = \left(\omega_{\exp}^{C\alpha} - \omega_{BMRB}^{C\alpha}\right) - \left(\omega_{\exp}^{C\beta} - \omega_{BMRB}^{C\beta}\right) \quad (2.1)$$

Negative values of secondary chemical shift (Δδ) are indicative of β-strand conformation, while positive values indicate α-helical conformation[79,81].

1.7 Relevance of studying paramagnetic metalloproteins using ssNMR

Even though isotropic chemical shifts can be used for estimating the secondary structure of the protein, calculation of the tertiary structure requires a large number of unambiguous internuclear distances[10]. In the case of ssNMR, distance information can be obtained from PDSD experiments or other proton-mediated dilute spin correlation experiments[10,82-84]. However, one of the main outstanding problems in biomolecular ssNMR is still related to the problems of obtaining unambiguous long-range structural restraints. The measurement of such distance restraints in fully ^{13}C-enriched samples is often hindered by dipolar truncation effects[55,66]. The presence of intrinsic or extrinsic paramagnetic centers in proteins can be of immense help in this regard, because of their intrinsic magnetic field leading to significant alterations of the chemical shifts of the nuclei in close proximity (Fermi contact shifts, "pseudocontact shift" (PCS) and/or by paramagnetic relaxation enhancement (PRE)[85-87]. The key aspects of nuclei and unpaired electron spin-spin interactions that are important for the understanding some of the experimental

results are described in the following sections. Detailed aspects of electron-nucleus interactions and the consequences can be found in several outstanding textbooks and reviews[86,88].

1.7.1 Electron-nucleus interactions

Free electrons possess an angular momentum and a magnetic moment. In the case of a paramagnetic centre having a single unpaired electron (S = ½), the presence of a strong static external magnetic field $\vec{B}_0$, will result in the splitting of the spin states of the unpaired electron spin into two energy levels ($2S$+1) according to the Boltzmann distribution. Due to their large magnetic moment, ($|\gamma_e/\gamma_H|$~660), the unpaired electron or electrons containing a paramagnetic moiety could couple very strongly to the neighboring nuclear spins. Since the electrons relax several orders of magnitude higher than the coupling frequency, the nucleus sense only an average spin state of the electron manifesting itself in a temperature-dependent frequency shift. In paramagnetic systems there are mainly three NMR experimental observables that yield long-range structural information: changes in chemical shifts (Fermi contact shifts[89], pseudocontact shift (PCS))[90], paramagnetic relaxation enhancements (PREs)[91], and residual dipolar couplings (RDCs). The PREs can be detected in any paramagnetic system, whereas PCSs and RDCs can only be observed in systems with an anisotropic electron g-factor[92].

1.7.2 Hyperfine shift

The NMR lines affected by the presence of unpaired electrons may experience an extra contribution to the chemical shift, which is called as the hyperfine shift. Hyperfine shifts, in turn, have two major contributions; the Fermi contact shift (δ_{con}), and the electron-nuclear dipolar or pseudocontact shift (δ_{pcs}). The observed chemical shift (δ_{tot}) is the sum of all the three contributions as given as[90],

$$\delta_{tot} = \delta_{con} + \delta_{pcs} + \delta_{dia} \qquad 1.16$$

1.7.3 Contact shift (Fermi contact shift)

The contact contribution is due to non-zero unpaired electron spin density delocalized on the observed resonating nuclei. It mainly involves the *s* orbitals, which have non-zero electron density at the nucleus. Spin density is mainly transferred through chemical bonds and the "Fermi contact" contribution[89] to the NMR resonance frequency is given by,

$$\delta^{con} = \left(\frac{A}{\hbar}\right)\left(\frac{g_e \mu_B S(S+1)}{3\gamma_I K_B T}\right) \qquad 1.17$$

Where $\hbar$ is the Planck's constant, S is the spin quantum number for the paramagnetic center, γ_I the nuclear gyromagnetic ratio, K_B is the Boltzmann constant, and A is the contact coupling constant expressed in terms of fundamental constants and the electron spin density at the nucleus, ρ:

$$A = \left(\frac{\mu_0}{3S}\right)\left(\hbar \gamma_I g_e \mu_B \rho\right) \qquad 1.18$$

Where μ_0 is the magnetic permeability of vacuum, g_e is the Lande factor, μ_B is the Bohr magneton and the other symbols as described before in the previous paragraph. This shift contains structural information, but is hidden inside the particular mechanisms of unpaired-electron delocalization and no general protocols are available so far for structural determination[86].

1.7.4 Pseudocontact shift (PCS)

The electron magnetic moment is constituted by both spin (isotropic) and orbital (anisotropic) contributions. In the presence of significant orbital contributions to the electron magnetic moment, the induced magnetic moment changes in intensity upon molecular rotation in an external magnetic field and the magnetic susceptibility tensor (χ) associated with the molecule becomes anisotropic. Under these circumstances, the dipolar shift provided by the magnetic field

generated by the electron does not average to zero, and the average magnetic field that is added to the external magnetic field and can be approximated based on the electronic g-tensor as[94]:

$$\delta^{pcs} = \left(\frac{\mu_0}{4\pi}\right)\left(\frac{\mu_B^2 S(S+1)}{18K_B T}\right)\left(\frac{1}{r^3}\right)\left\{\left[2g_{zz}^2 - \left(g_{xx}^2 + g_{yy}^2\right)\right]\left(3\cos^2\theta - 1\right) + 3\left(g_{xx}^2 - g_{yy}^2\right)\sin^2\theta\cos 2\Omega\right\} \quad 1.19$$

Generally speaking, each nucleus in a paramagnetic protein may experience a sum of contact shifts and PCSs. However, if the number of chemical bonds separating the nucleus from the metal ion is larger than four and involves no π-bonds, the contribution from contact shifts can be considered to be negligible and any observed hyperfine shift can be considered to be PCSs in nature[86].

1.7.5 Paramagnetic Relaxation Enhancement (PRE)

In addition to contact and pseudocontact shifts of the NMR resonance frequencies, the electron-nucleus interactions could also lead to enhanced nuclear spin relaxation rates. Nuclear spins are relaxed by two principle mechanisms: (i) the stochastic interaction with the electron spin ("Solomon-Bloembergen" dipolar and contact mechanisms)[91], and (ii) by interaction with the net magnetic moment (Curie spin) in thermal equilibrium created by the very short electronic relaxation time (Curie mechanism)[95].

1.7.6 Curie relaxation

Since the dynamics of electron relaxation and precession is several orders of magnitude faster than the NMR timescale, the electron spin *S* detected in the NMR experiment reduces to the so-called "Curie spin" $\langle S_z \rangle$ averaged over different Zeeman states. In the case of solution-state NMR, the average electronic magnetic moment $\langle \mu_s \rangle$ generates field fluctuations on the nucleus due to the stochastic reorientation of the molecule described by the rotational correlation time τ_r, and is called as "Curie relaxation" or magnetic susceptibility relaxation[95]. The Curie contribution to nuclear spin relaxation rates can be described by the following equations:

$$R_{1M}^{Cur} = \left(\frac{2}{5}\right)\left(\frac{\mu_0}{4\pi}\right)^2 \frac{\omega_I^2 g_e^4 \mu_B^4 S^2 (S+1)^2}{(3K_B T)^2 r^6}\left[\frac{3\tau_r}{1+\omega_I^2 \tau_r^2}\right] \quad 1.20$$

$$R_{2M}^{Cur} = \left(\frac{1}{5}\right)\left(\frac{\mu_0}{4\pi}\right)^2 \frac{\omega_I^2 g_e^4 \mu_B^4 S^2 (S+1)^2}{(3K_B T)^2 r^6}\left[\frac{3\tau_r}{1+\omega_I^2 \tau_r^2} + 4\tau_r\right] \quad 1.21$$

Where R_{1M} and R_{2M} are the longitudinal and transverse Curie relaxation rates, and the other variables have been defined as above. However, ssNMR signals of paramagnetic systems (rigid solid samples with no or reduced molecular tumbling) are not subject to Curie line broadening[96], which is one of the limiting factors in the study of large paramagnetic molecules by solution-state NMR.

1.7.7 Solomon-Bloembergen relaxation

Since the electron relaxation lifetime is comparable to or shorter than the rotational correlation time of a macromolecule, Solomon-Bloembergen theory makes the simplifying approximation that electron relaxation is not coupled to molecular tumbling. Therefore, longitudinal (T_1) and transverse (T_2) paramagnetic relaxation enhancement can be conveniently expressed by the Solomon-Bloembergen equations as,[88,91,97,99]

$$T_1 \approx \left(\frac{2}{15}\right)\left(\frac{\mu_0}{4\pi}\right)^2 \frac{\gamma_I^2 g_e^2 \mu_B^2 S(S+1)}{r^6}\left[\frac{3\tau_{c1}}{1+\omega_I{}^2 \tau_{c1}^2} + \frac{7\tau_{c2}}{1+\omega_S{}^2 \tau_{c2}^2}\right] \quad 1.22$$

$$T_2 \approx \left(\frac{1}{15}\right)\left(\frac{\mu_0}{4\pi}\right)^2 \frac{\gamma_I^2 g_e^2 \mu_B^2 S(S+1)}{r^6}\left[4\tau_{c1} + \frac{3\tau_{c1}}{1+\omega_I{}^2 \tau_{c1}^2} + \frac{13\tau_{c2}}{1+\omega_S{}^2 \tau_{c2}^2}\right] \quad 1.23$$

Where μ_0 is the permeability of free space, γ_I is the nuclear gyromagnetic ratio, g_e is the electron g-value, μ_B is the Bohr magneton, S is the electron spin quantum number, r is the electron-nucleus distance and ω_I and ω_S are the nuclear and electron Larmor frequencies. In general, the correlation times τ_{c1} and τ_{c2} contain contributions from longitudinal (T_{1e}), transverse (T_{2e})

electron spin relaxation, rotational correlation time (τ_r) and chemical exchange correlation time (τ_M) and are given by:

$$\frac{1}{\tau_{c1}} = \frac{1}{T_{1e}} + \frac{1}{\tau_r} + \frac{1}{\tau_M} \quad 1.24$$

$$\frac{1}{\tau_{c2}} = \frac{1}{T_{2e}} + \frac{1}{\tau_r} + \frac{1}{\tau_M} \quad 1.25$$

In the case of rigid solid samples, τ_r and τ_M terms can be typically be neglected, so that $\tau_{c1} = \tau_{c2} = T_{1e}$ could be used in the above equations. Furthermore, single electronic relaxation time, $T_{1e} = T_{2e}$, can often assumed to be a reasonable approximation[99].

1.7.8 Paramagnetic effects in Nitrophorin 7

Paramagnetic effects in NPs can be exploited by incorporating different external ligands into the vacant 6th coordination site of the Fe^{III} centre in the heme group. A schematic illustration of modifying the electronic spin states of Fe^{III} in the heme pocket of NP7 is shown in fig. 1.4. In the absence of any external ligands, 6th coordination site is occupied by weak field ligands like water molecule (H_2O) producing small crystal field splitting resulting in five unpaired electrons (S=5/2) and thereby forming a high spin (HS) complex. In the presence of strong-field ligands like cyanide or imidazole (ImH), electrons are preferentially paired in the t_{2g} orbitals leaving one unpaired electron (S=½) and thereby forming a low spin (LS) complex. In the case of diamagnetic complexes, sixth coordination site is ligated by nitric oxide radical (NO) leaving no unpaired electrons. Nitrophorins (NP1-4) have been extensively studied in the paramagnetic and the diamagnetic forms using solution-state NMR, to mention a few among them[36,37,100-104]. However, signals from the ^{1}H NMR spectra reported from previous solution-state NMR studies of NP7 were extremely broad and difficult to be assigned at pH 7.0[37]. This effect was ascribed to the dipolar nature of NP7, which in solution results in inter-molecular interaction between

different NP7 molecules and thereby resulting in the formation of high molecular weight aggregates. These high molecular weight aggregates tumble more or less slowly in the NMR sample tube resulting in decreased T_2 or spin-spin relaxation times and thereby broadening the lines. In the case of ssNMR, since line width is independent of molecular weight[105], it can be successfully employed to high molecular weight systems. Furthermore, in the limit of no or reduced molecular tumbling, Curie relaxation is found to be absent for solid samples thereby making ssNMR an ideal tool for exploiting paramagnetic effects[96]. Therefore ssNMR was used as an alternative and effective method of choice for exploiting paramagnetic effects from the NP7 aggregates. Further details about expression, purification and ssNMR characterization of NP7 in two electronic spin states are explained in detail in the following chapters.

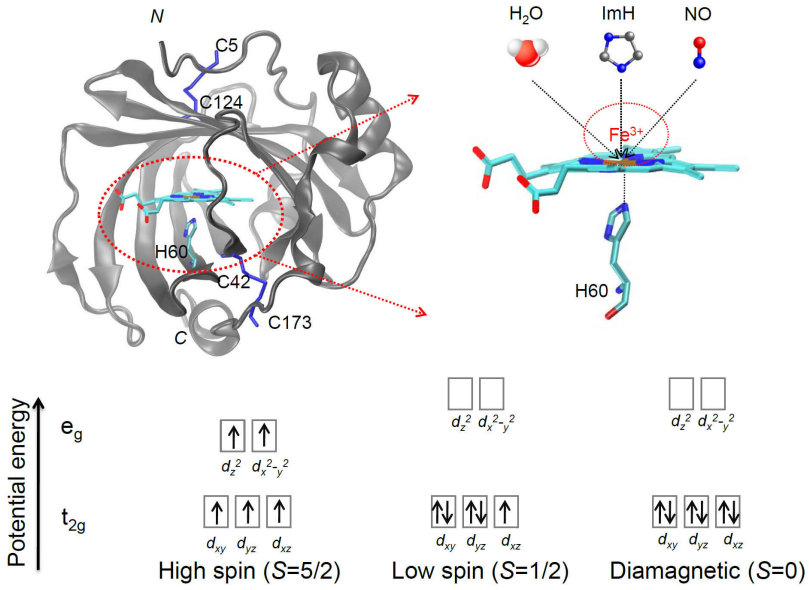

Fig. 1.4: Schematic illustration of the tuning of paramagnetic effects in NP7 using external ligands. (a) Modified cartoon representation of NP7. (b) Heme centre in the NP7 where the 5th coordination site is occupied by His60. (c) Splitting of d-orbitals and electron spin pairing in the presence of external ligands.

2 Materials and methods

2.1 Expression and purification of nitrophorin 7

Prior to recombinant expression, $pNP7^{Kan}$ was transformed into *Escherichia coli* strain BL21 (DE3) (Novagen). Natural abundance NP7 was expressed in LB medium (1% (w/v) tryptone, 0.5% (w/v) yeast extract, and 1% (w/v) NaCl) at 37°C as described previously[24]. The medium was supplemented with 30 mg L^{-1} kanamycin A and 0.005% (v/v) Antifoam 204 (Sigma-Aldrich).

2.2 Reverse isotopic labeling

When compared to solution-state NMR, protons in a solid samples form a dense network of dipolar-coupled spins, leading to homogeneous line-broadening and thereby resulting in very poor resolved spectra. Furthermore, owing to the low natural abundance of ^{13}C (1.1%) and ^{15}N (0.36%) nuclei, isotopic enrichment is a prerequisite for signal enhancement in most of the ssNMR applications. Several isotope labeling protocols like uniform, specific, selective, and reverse labeling have been introduced in NMR to increase sensitivity and resolution[106]. Uniform labeling (U-^{13}C, ^{15}N) is a very common form of isotopic labeling in which protein is produced by expression from *E-coli* which are grown on minimal medium supplemented with $^{15}NH_4Cl$ and $^{13}C_6$-glucose[106]. A cheaper and effective way of labeling only certain amino acids often called as "reverse labeling", involves expressing the protein in *E.coli* which are grown on minimal medium supplemented with $^{15}NH_4Cl$ and $^{13}C_6$-labelled glucose along with the unlabelled amino acids that are to be masked in the spectra[106]. Reverse labeling is used to reduce the spectral overlap and to monitor certain amino acids without interference from other signals[107,108] and is used as an effective method of choice in this research work.

For the expression of labeled protein, an overnight culture of 1 L was set up for growth at 37°C. For the expression culture, a minimal medium was prepared of the following composition: 6 g L^{-1} NaH_2PO_4, 3 g L^{-1} K_2HPO_4, 0.5 g L^{-1} NaCl, 8 mM $MgSO_4$, 0.8 mM $CaCl_2$, 2 g L^{-1} [U-$^{13}C_6$]-D-glucose, 1 g L^{-1} $^{15}NH_4Cl$. The pH of this solution was titrated with KOH to pH 7.5. One liter of this solution was further supplemented with 10 mL trace element solution, 1 mL 100 × BME vitamins (Sigma Aldrich), 50 µL Antifoam 204 (Sigma Aldrich), 1 mL of 10% (w/v) yeast extract, 5 mg $(NH_4)_2Fe(SO_4)_2 \times 7H_2O$, and 1 mL of 30 mg L^{-1} kanamycine A. One liter of the trace element solution contained 5g of Na_2EDTA, 4 mg of $NaMoO_4$, 50 mg of $ZnCl_2$, 10 mg of $CuCl_2$, 10 mg of $CoCl_2 \times 6H_2O$, 10 mg of H_3BO_3, and 400 mg of $MnCl_2 \times 4H_2O$. The overnight culture was centrifuged and the cells were resuspended in 0.9% (w/v) NaCl. Afterwards, 2 L of the expression culture were inoculated with the cells of the overnight culture and expression was immediately induced with 1 mM of Isopropyl-*β*-D-thiogalactopyranosid (IPTG). In case of the reverse-labeled samples (see below), either 100 mg L^{-1} each of L-lysine and L-valine or L-lysine, L-phenylalanine, and L-tyrosine were added, respectively.

The expression was performed on a shaker at 37°C. After harvesting the cells, they were broken using an Emulsiflex C-15 high pressure homogenizer (Aventis) with a pressure of 1500 bar. The protein was yielded as inclusion bodies, washed, and solubilized in 6 M GdmCl (Guanidinium chloride) essentially as was previously described[24]. Upon size exclusion chromatography (SEC), a novel chromatographic step using Chelating Sepharose was introduced.

2.3 Chelating sepharose chromatography

A 5 mL HiTrap Chelating Sepharose column, (GE Healthcare) was at first loaded with 100 mM $CaCl_2$ in 1% (v/v) CH_3COOH. Afterwards, the column was equilibrated with 50 mM MOPS/NaOH (pH 6.8), 2 % (v/v) glycerol. Combined fractions from SEC were then bound to

the column. Elution was performed with a linear gradient of 0-40 mM $CaCl_2$. In another experiment, the column was not charged with Ca^{2+} and elution was performed with a linear gradient of 0-40 mM L-glutamic acid. The elution profile was monitored by 280 nm absorption and fractions of 1 mL were collected.

2.4 Protein characterization

After preparation, the protein is routinely characterized by UV-vis spectroscopy, SDS PAGE and MALDI-TOF MS to be >95% pure. Prior to mass spectrometry, samples were concentrated and depleted of buffer components using $ZipTip_{C18}$ (Millipore) according to the supplier's protocol. Samples were eluted with 2 µL of 0.1% TFA, 75% CH_3CN and spotted on sinapinic acid. For comparison with the mass spectrometry results, expected masses were calculated with Isotopident[1].

2.5 Diffusion ordered spectroscopy (DOSY) experiments

Solution-state DOSY measurements were performed by Dr. V. Pacheco on a Varian INOVA 600 MHz spectrometer operating at 599.644 MHz. ^1H (^{13}C) DOSY measurements were conducted using the standard Varian $^1H^{13}C$-DOSY-HSQC pulse sequence without spinning and at 25°C[109,110]. The gradient was calibrated at 25°C with a deuterated methanol sample using diffusion values previously obtained by NMR, for CD_3OH ($D = 2.22\times10^{-9}$ m^2/s) and for CHD_2OD ($D = 2.18\times10^{-9}$ m^2/s)[111,112]. The gradient strength was incremented in 25 steps from 11.1 up to 59.3 G/cm. The diffusion time was 0.25 s with a gradient duration of 1000 µs. The water signal was suppressed using the WATERGATE sequence[113]. Measurements were performed with 0.25 mM of [U-^{13}C,^{15}N\(K,V)]NP7-NO in 30mM KH_2PO_4/KOH (pH 5.0) with 10% D_2O. Ensemble average of the molecular masses of the phosphate anions (Mr=96.98 Da)

[1] Available at http://education.expasy.org/student_projects/isotopident/htdocs/.

was used as an internal reference for approximating the molecular weights of the different NP7 oligomeric complexes. Further details about the theoretical and practical aspects of the procedure are given elsewhere[114,115].

2.6 Solid-state NMR experiments

For the ssNMR experiments, the protein samples were concentrated in ultrafiltration spin concentrators (Amicon Ultra 10 K, Millipore) where as a final step the buffer was exchanged to 30 mM KH_2PO_4/KOH, 2% (v/v) glycerol, 1 mM GSSG (pH 5.0). The final NP7 concentrations reached approx. 2 mM and precipitation was observed. NO loaded samples were prepared by the addition of a small molar excess of diethylammonium 2-(*N*,*N*-diethylamino)-diazenolate-2-oxide (DEA/NO) dissolved in 10 mM NaOH. Imidazole (ImH) loaded samples were prepared by the addition of 10 mM from a solution of 1 M ImH/HCl (pH 5.0). The protein aggregates were transferred by spatula and centrifuged down into a 3.2 mm diameter MAS rotor for the ssNMR experiments.

The ssNMR spectra were taken on a Varian NMR spectrometer equipped with a 3.2 mm HXY BIOMAS probe tuned in the $^{1}H/^{13}C$ mode or $^{1}H/^{13}C/^{15}N$ triple resonance mode operating at field strengths of 14.1 T (600 MHz ^{1}H frequency) and 18.8 T (800 MHz ^{1}H frequency). Spectra were recorded at MAS frequencies of 8, 11 and 15 kHz. Pulse sequences were implemented with linear-ramped cross-polarization (CP)[19] with small phase incremental alternation (SPINAL)[52] ^{1}H decoupling at ~83.3 kHz. The typical $\pi/2$ pulse widths were 3 μs on ^{1}H and 6 μs on ^{13}C. All multidimensional data were processed using NMRPipe[116] with forward & backward linear prediction in the indirect dimension, zero filled and apodized with a combination of an exponential and a Gaussian function (GMB) for both dimensions before Fourier transformation. Additional acquisition and processing parameters for each spectrum are provided in the figure

captions. Chemical shifts were referenced externally to adamantane[117]. Temperature calibration was achieved using nickelocene as an external reference[118]. All multi-dimensional spectra were analyzed using Sparky version 3.115 (T. D. Goddard and D. G. Kneller, University of California, San Francisco) and CCPN (Collaborative Computing Project for NMR)[119,120].

2.7 Resonance assignments

In the case of NMR, the first step towards three-dimensional structural calculation involves recording a series of homo- and hetero-nuclear 2D and 3D correlation spectra using selective magnetization transfer schemes. For example, heteronuclear NCA/NCO spectra are obtained by transferring magnetization from ^{1}H to ^{15}N using cross-polarization and then selectively from ^{15}N to C_{α} of the same residue or from ^{15}N to $C'_{(i-1)}$ of the previous residue respectively using CP (SPECIFIC CP)[121,122] steps. An extension of the above sequences is made by transferring the magnetization to the nearby ^{13}C nuclei as in the case of NCACX/NCACB and NCOCX using PDSD[60-62], DREAM[56,57] or DARR[64,65] mixing schemes. Sequential information can also be gained from CANCO/CANCOCX[123] spectra and can act as a complementary tool to the above spectra. In this case, intraresidual magnetization transfer is established from ^{1}H to C_{α} and then selectively to ^{15}N of the same residue using specific CP. This is followed by another specific CP step, in which magnetization is transferred to the C' of the previous residue.

Spin system identification and intraresidual assignments are done mainly based on the homonuclear ^{13}C-^{13}C correlation and heteronuclear NCACX/NCACB spectra. This is followed by inter-residual sequential assignments which aid in establishing sequential links between the identified i^{th} and (i-1) residues using NCO/NCOCX, CANCO/CANCOCX spectra. It has been demonstrated that sequential resonance assignments can also be obtained from (^{13}C, ^{13}C) correlation spectroscopy from uniformly labeled protein under weak coupling conditions[124].

Weak inter-residual ($C'_{(i-1)}$, $C_{\alpha\ (i)}$) coupling conditions were created by adjusting the MAS rate close (not exact) to the rotational resonance condition (n=2)[124]. Schematic representation of magnetization transfer schemes employed for intra- and inter-residual assignments used in this research work is displayed in figure 2.1.

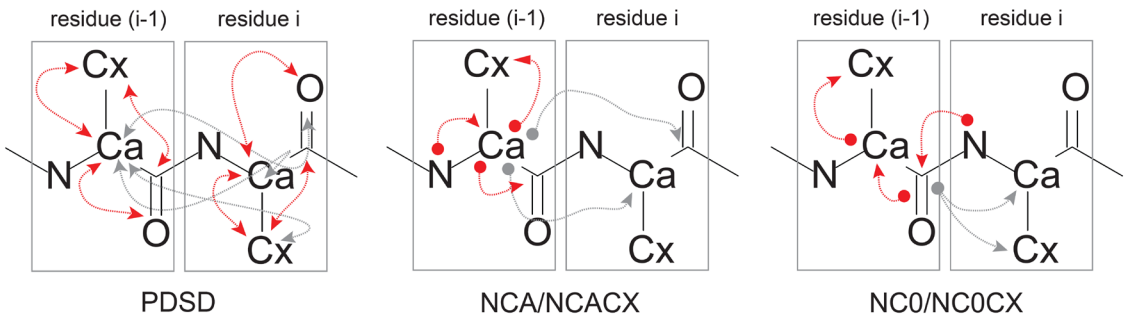

Fig. 2.1: Schematic representation of magnetization transfer schemes achieved using PDSD mixing for aiding intra- and inter-residual assignments. Predominant magnetization transfer pathways under weak coupling conditions and short mixing times are shown by dotted red arrows. Inter-residual magnetization transfers during long mixing times are shown by dotted gray arrows.

3 Expression, Purification and Solid-state NMR Characterization of the Membrane Binding Heme Protein Nitrophorin 7 in two Electronic Spin States

We report the expression and purification of ^{13}C, ^{15}N isotopically labeled protein together with the first ssNMR characterization of NP7. Because the size of NP7 (21 kDa) still provides a challenge for ssNMR, the samples were reverse-labeled with Lys and Val to reduce the number of cross-peaks in two-dimensional spectra. The two electronic spin states with S=½ and S=0 at the ferriheme iron were generated by the complexation with imidazole and NO, respectively. ssNMR spectra of both forms are well resolved, allowing for sequential resonance assignments of 22 residues. Importantly, the ssNMR spectra demonstrate that aggregation does not affect the protein fold. Comparison of the spectra of the two electronic spin states allows the determination of paramagnetically shifted cross-peaks due to pseudocontact shifts (PCSs) which assists the assignment of residues close to the heme center.

3.1 Protein expression and purification

The recombinant expression of the ^{13}C, ^{15}N double labeled NP7 was performed in minimal medium supplemented with [U-$^{13}C_6$]-D-glucose and $^{15}NH_4Cl$. The yield of protein in the minimal medium was slightly lower compared to LB medium (approx. 5 mg L^{-1}) indicating, however, that sufficient amounts of protein can be obtained. The successful incorporation of ^{13}C and ^{15}N into the protein was demonstrated by MALDI-TOF MS (Table 3.1).

Two further samples reverse-labeled with unlabeled Lys and Val (termed [U-^{13}C,^{15}N\(K,V)]NP7) and for Lys, Phe and Tyr (termed [U-^{13}C,^{15}N\(K,F,Y)]NP7) were produced by adding L-lysine and L-valine or L-lysine, L-phenylalanine, and L-tyrosine in natural abundance to the medium in excess. Where the final yield of the protein was similar to that of the fully labeled protein, MALDI-TOF MS indicated the successful isotopic distribution (Table 3.1). The deviation of molecular mass by 63 Da in [U-^{13}C,^{15}N\(K,V)]NP7 from the expected value is probably due to isotopic scrambling between Val and Leu[125]. Likewise, de novo synthesis of the reversely labeled residues Lys and Val is not completely suppressed: In the INEPT-TOBSY spectrum, which displays only signals from mobile fractions or monomers. However, in the double-quantum spectrum, which displays only rigid parts of the sample, where the shift dispersions between different amino acids of the same type is larger, a complete side chain walk could not be established for the Lys and Leu residues (Fig. 3.1, 3.9). Thus, addition of Lys and Val in natural abundance strongly suppresses but not completely prevents de novo synthesis from glucose.

	$[M + H]^+$	
	Observed (Da)	Calculated (Da)
NP7	20,969 ± 20	20,966
[U-^{13}C,^{15}N]NP7	22,154 ± 20	22,153
[U-^{13}C,^{15}N/(K,V)]NP7	21,796 ± 20	21,859
[U-^{13}C,^{15}N/(K,F,Y)]NP7	21,741 ± 20	21,746

[a] Sinapinic acid was used as matrix. [b] Calculated with Isotopident.

Table 3.1: Molecular Masses of the Various NP7 Isotope Labeling States Generated in This Study Determined by MALDI-TOF MS[a].

Where the purity of the protein at this stage is sufficient for most spectroscopic experiments[24,36,126,127] as judged by SDS-PAGE and MALDI-TOF MS, for the case of NMR spectroscopy and X-ray crystallography maximum purity is required[35]. This was achieved by an additional chromatographic step. Because of the strong basicity of NP7, cation exchange chromatography should be feasible. However, attempts to purify the protein on common cation exchange media resulted in loss of protein due to denaturation. We ascribe this to the instability of the fold in high ionic strength, which is required for protein elution. A method was developed using Chelating Sepharose HP, which provides iminodiacetic acid groups for binding. The protein readily binds to the resin and can be eluted with glutamic acid. Glutamic acid is used as an eluent because it contains two carboxylates so that lower concentrations of eluent are required, i.e., less ionic strength. Furthermore, from the purification protocol it is known that glutamate stabilizes the protein[24]. The elution profile demonstrates that some contaminants are well separated from the protein.

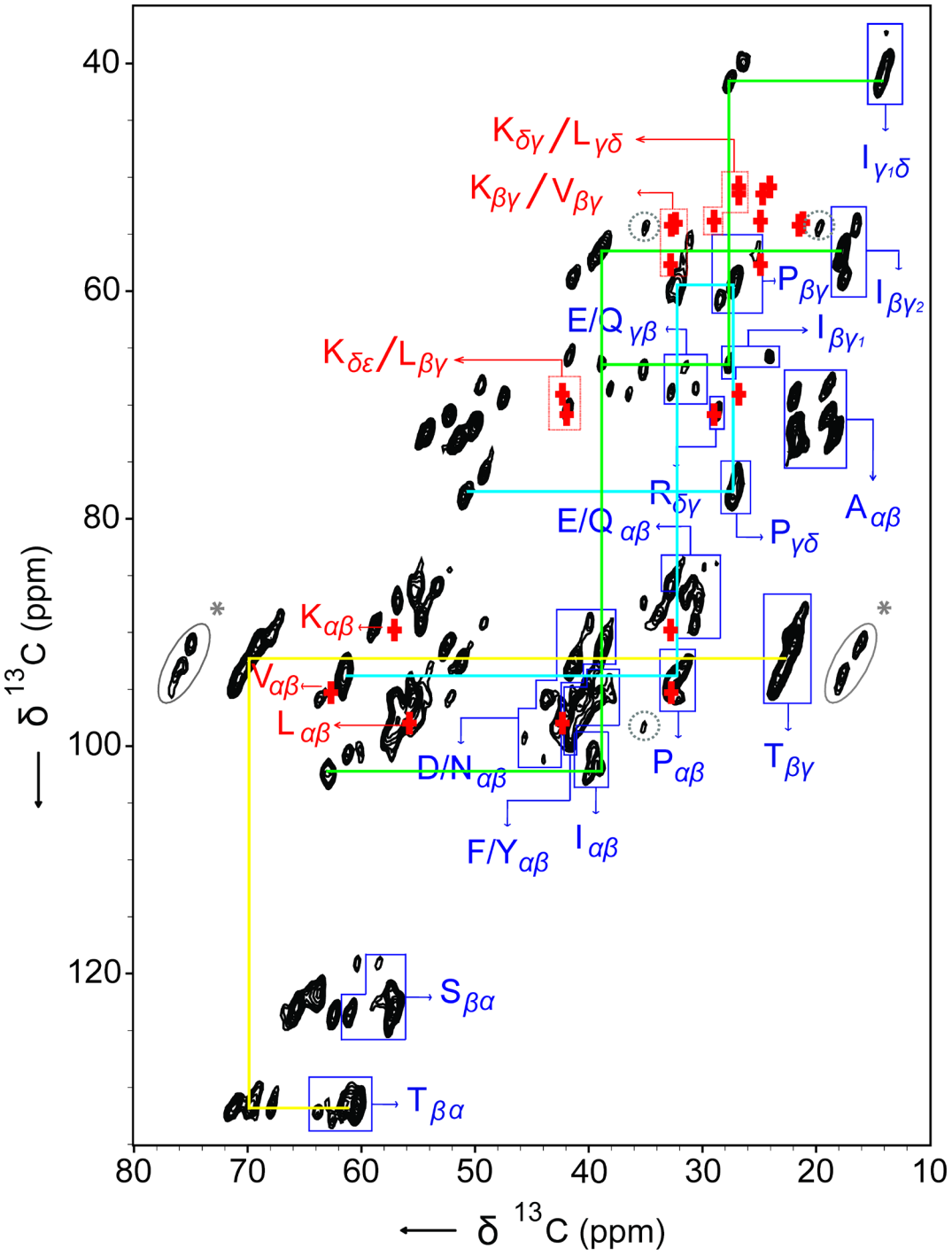

Fig. 3.1: Overlay of the aliphatic region of the 2D DQ-SQ ^{13}C-^{13}C correlation spectrum of [U-^{13}C,^{15}N\(K,V)]NP7-ImH with the average random coil chemical shift values for the Lys, Val and Leu residues from BMRB (red crosses). The spectrum was acquired at a ^{1}H Larmor frequency of 600 MHz. The double quantum coherence was excited by SPC-5 recoupling scheme. The data

were collected at -30°C and 8 kHz spinning frequency. The other acquisition parameters are 0.6 ms ^{1}H-^{13}C CP contact time, 83 kHz ^{1}H SPINAL decoupling, 3 ms acquisition time in the indirect dimension with States detection, 13.75 ms acquisition time in the direct dimension and 2 s recycle delay. The data were processed with combination of an exponential and a Gaussian function (-150 Hz exponential, Gaussian factor 0.2), zero filled to 512 (F2) × 4096 (F1) complex points with a linear base line correction in the direct dimension. Spinning side bands are shown in gray ovals with asterisks. Identified spin systems are displayed in blue with the intra residual side chain assignments shown for Ile (green), Pro (cyan) and Thr (yellow). The peaks in the dashed grey circles indicate the possible cross peaks (~63/35/20) from the Val residues.

Losses of NP7 could be further minimized by charging the column with Ca^{2+} prior to the protein binding step. When the protein is loaded onto the column, NP7 and Ca^{2+} supposedly compete for the resin-carboxylates, which is indicated by a broader distribution of the red color at the top of the resin. Fig. 3.2 shows an example where elution was performed with a linear gradient of $CaCl_2$ where essentially all of the applied protein was recovered. The elution profile indicates that the protein is well separated from impurities and is now ready for NMR experiment which is also confirmed by SDS-PAGE.

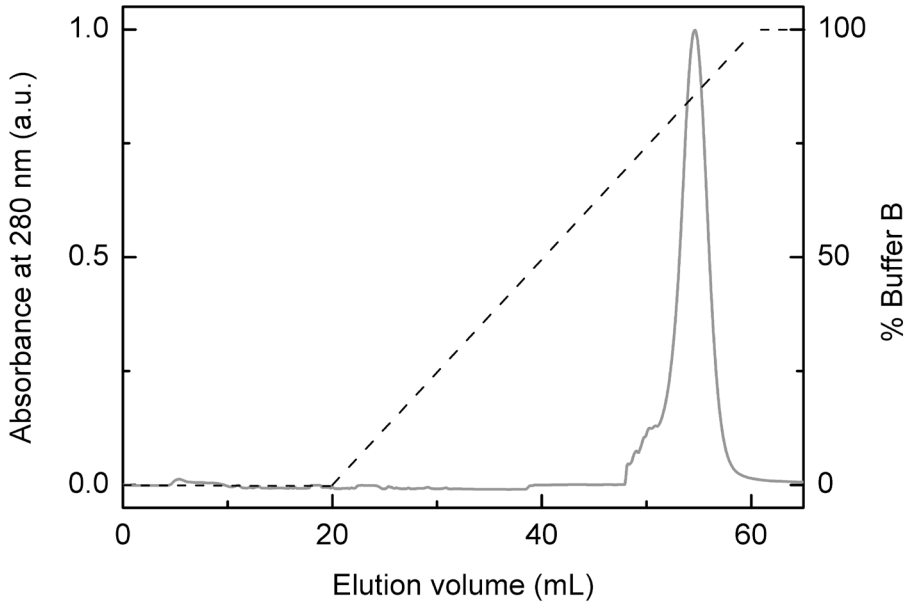

Fig. 3.2: Elution profiles of NP7 bound to Ca^{2+} charged Chelating Sepharose HP monitored by the absorbance at 280 nm. Elution was performed with a linear gradient of 0-40 mM of $CaCl_2$.

3.2 NP7 tends to oligomerize in solution

In previous solution NMR experiments of NP7 severe line broadening was observed when compared to NP1-4[36,37]. It was assumed that this is an effect of aggregation at the high concentrations required for NMR measurements (1-2 mM), which was strongly supported by dynamic light scattering measurements on NP7, where the apparent hydrodynamic diameters of the oligomers were of the order of ~250 - 400 Å, which corresponds to oligomers of approximately 6 to 10 units[36].

In order to acurately determine the state of oligomerization, DOSY experiments on [U-^{13}C,^{15}N\(K,V)]NP7-NO in solution were recorded at 25°C and at a ^{1}H Larmor frequency of 600 MHz by Dr. V. Pacheco. Fig. 3.3 displays the aromatic region of the pseudo 2D ^{1}H (^{13}C) DOSY spectra of [U-^{13}C,^{15}N\(K,V)]NP7-NO versus the corresponding self-diffusion coefficients of the

molecular species. The spread of signals in the DOSY plot indicates a mixture of NP7 oligomers. The diffusion coefficients obtained from the 2D plot were used for the calculation of molecular weights (Table 3.2). T_2 can be short for slowly tumbling high molecular weight oligomeric assemblies, and this can lead to a severe loss of signal[128]. Therefore, oligomers with molecular weight in excess of 50 kDa are difficult to measure by standard PFG-NMR methods using stimulated echoes[128,129]. For thermostable macromolecules, one simple solution to this problem is to increase the overall molecular tumbling rate by recording NMR spectra at elevated temperatures[130,131]. However, measurements at higher temperature of 35°C resulted in the irreversible precipitation of the protein in the NMR sample tube which is in good agreement with the thermal instability observed before[36].

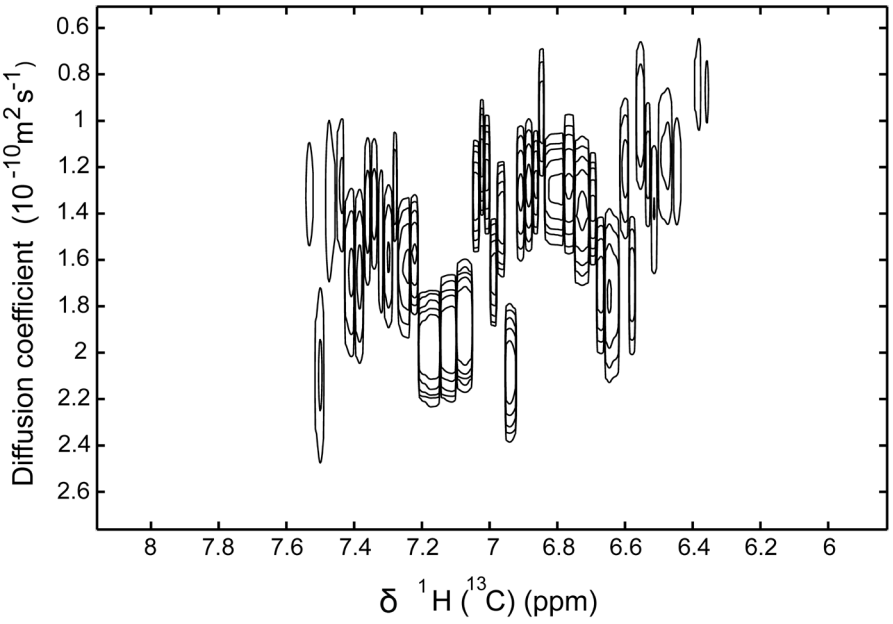

Fig. 3.3: Aromatic region of the 2D ^{1}H (^{13}C) DOSY NMR plot of [U-^{13}C,^{15}N\(K,V)]NP7-NO recorded at a field of 14.1 T (600 MHz ^{1}H frequency) at 25°C in KH_2PO_4 buffer prepared with a mixture of 10% D_2O at pH 5.0.

Observed Diffusion Co-efficient D_2 (10^{-10} m^2 s^{-1})	Calculated Molecular Weight M_2 (kDa)	Theoretical Molecular Weight (kDa)
1.40 ± 0.05	23.25	23.27 (monomer)
1.00 ± 0.04	63.79	63.86 (trimers)
0.80 ± 0.03	124.58	124.73 (hexamers)

[c] Gutz, I. G. R., CurTiPot – pH and Acid-Base Titration Curves: Analysis and Simulation software, version 3.6.1 http://www2.iq.usp.br/docente/gutz/Curtipot_.html

Table 3.2: Molecular masses of the various NP7 complexes calculated from the corresponding diffusion coefficients.

Molecular weights were calculated from the diffusion coefficients using the formula[115],

$$\frac{D_1}{D_2} = \sqrt[3]{\frac{M_2}{M_1}}$$

Ensemble average of the molecular mass of $H_2PO_4^-$ M_1 = 96.98 Da[c]

Diffusion coefficient of the Phosphate anions at 25°C D_1 = 8.7 ± 0.06 (10^{-10} m^2 s^{-1}) (Fig. 3.4.)

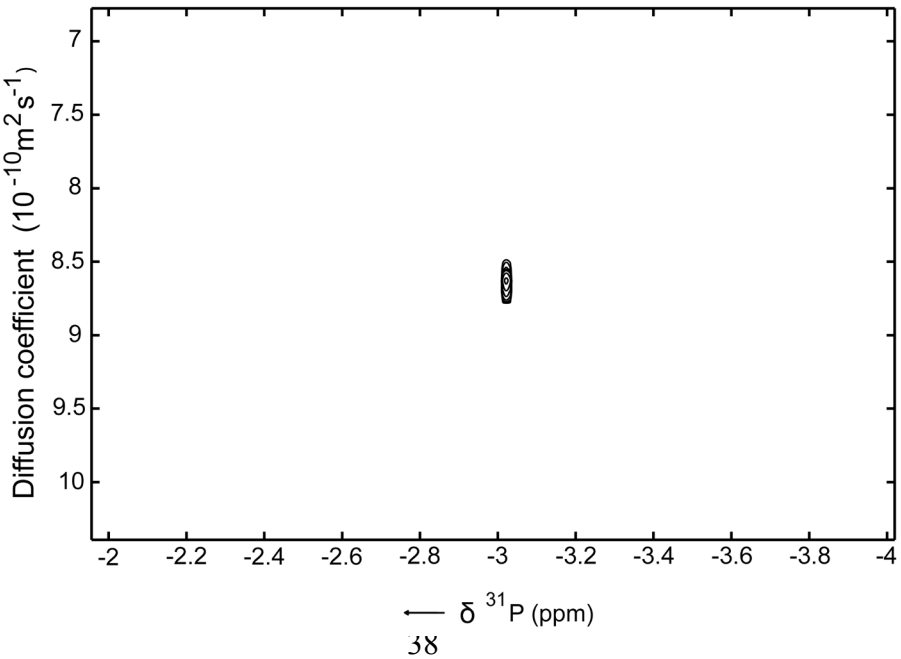

Fig. 3.4: 2D DOSY NMR plot of ^{31}P recorded at a ^{1}H Larmor frequency of 600 MHz at 25°C from the K_2HPO_4 buffer prepared with a mixture of 10% D_2O at pH 5.0.

3.3 NP7 precipitates at high concentrations

At concentrations required for NMR measurements (2 mM) the sample containing diamagnetic [U-^{13}C,^{15}N\(K,V)]NP7-NO was already completely precipitated. The resulting precipitate could directly be transferred into MAS rotors. In order to test whether the precipitate contained residual monomers or if certain regions of the protein are undergoing high amplitude motions at a time scale $<10^{-6}$ s, we investigated the dynamics of the sample in more detail.

Fig. 3.5 shows the temperature dependent one-dimensional ^{13}C spectra of [U-^{13}C,^{15}N\(K,V)]NP7-NO aggregates in the diamagnetic form recorded using CP[49] (black) and refocused INEPT[75] (red) based methods with and without MAS. The temperature was decreased from 10°C to -30°C in steps of 10°C and the process of freezing was monitored based on the line width change of the of the water signal. For a MAS frequency of 11 kHz, the freezing point of the solution was observed between nominal temperatures of -20°C and -25°C (Fig. 3.6). For the CP based experiments, the radio-frequency fields on ^{1}H and ^{13}C channels were matched to the zero quantum condition (42 kHz on both channels), so that the Hartmann-Hahn condition for the CP transfer[48] was nearly independent of the MAS frequency. For the INEPT based methods, the ^{1}H-^{13}C dephasing delay was set to 1.725 ms (1/4×J) corresponding to the characteristic J_{CH} coupling constant of around 145 Hz. Cross polarization relies on strong dipolar couplings, and is therefore an efficient transfer method for rigid samples, but not for solutions where molecules undergo rapid reorientation. On the other hand, regions with high mobility can be excited by INEPT magnetization transfer from protons to carbon[76,77]. In the case of NP7 at 10°C, the presence of signals in both INEPT and CP spectra are indicative of the presence of both rigid and

flexible moieties, which can, in principle, be explained by the presence of monomers as well as by flexible parts within the aggregates. (Fig. 3.5, top left). A further decrease in temperature from 10°C to -10°C did not show significant influence in signal intensities for CP and INEPT based methods. However, the CP spectra recorded at -30°C showed a drastic increase of CP signals by a factor of four in the absence and presence of MAS, due to the process of freezing within the temperature regime of -10°C to -30°C. The INEPT spectra of NP7 aggregates recorded at -30°C were devoid of any signals from the protein indicating the absence of residual dynamics at this temperature. Therefore, multidimensional ssNMR spectra based on CPMAS methods were performed at -30°C. MAS at 11 kHz improved the spectral resolution significantly for both CPMAS and INEPTMAS, as anisotropic interactions were efficiently averaged to yield well resolved resonance lines.

Fig. 3.7 shows a plot of the relative intensities from the representative regions of one-dimensional ^{13}C CPMAS and INEPTMAS spectra of [U-^{13}C,^{15}N\(K,V)]NP7-NO aggregates as a function of temperature. In the case of CPMAS, the C_α (55 ppm) regions from the protein backbone showed a 4-fold increase in intensity at decreasing the temperature from -10°C to -30°C. This effect is significant below -10°C as indicated by dotted grey lines. In the case of INEPTMAS, the signal intensities from the C_α resonances showed a 4-fold decrease in intensity below -10°C, and dissolved monomers were frozen in solution.

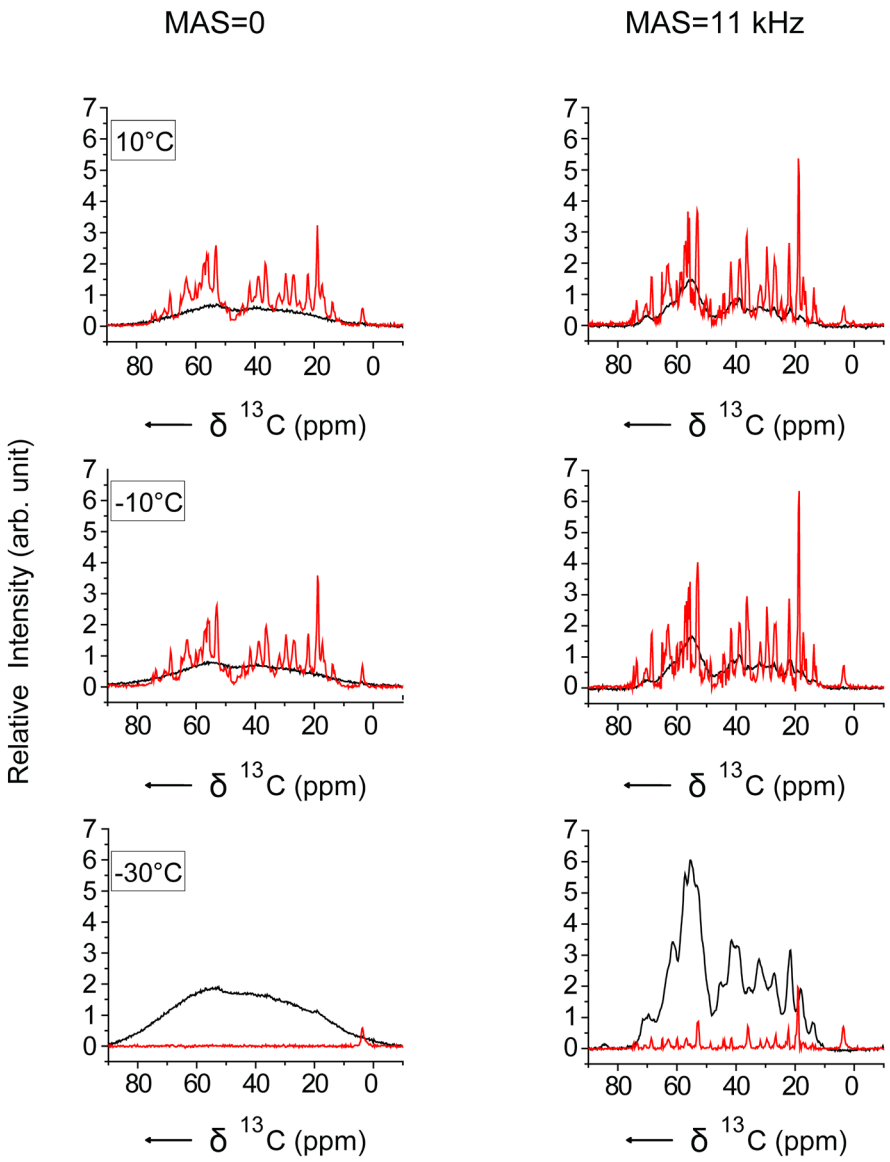

Fig. 3.5: Temperature dependent 1D ^{13}C spectra of [U-^{13}C,^{15}N\(K,V)]NP7-NO in the diamagnetic state recorded using CP (black) and INEPT (red) based methods with and without magic angle spinning. All the spectra were recorded at a ^{1}H Larmor frequency of 600 MHz and temperature was decreased from 10°C down to -30°C. For the INEPT based experiments, ^{1}H-^{13}C dephasing delay was set to 1.725 ms. All the spectra were processed with 10 Hz of line broadening.

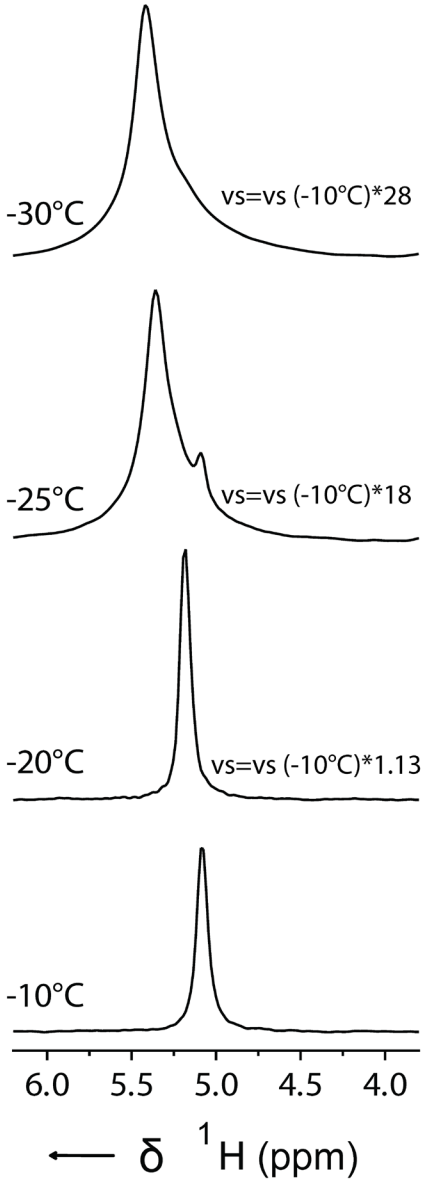

Fig. 3.6: 1D ^{1}H spectra of [U-^{13}C,^{15}N\(K,V)]NP7-NO aggregates from -10°C to -30°C. All the spectra were recorded at a ^{1}H Larmor frequency of 600 MHz at 11 kHz MAS. Data were processed with 10 Hz of line broadening and were fit to the same height.

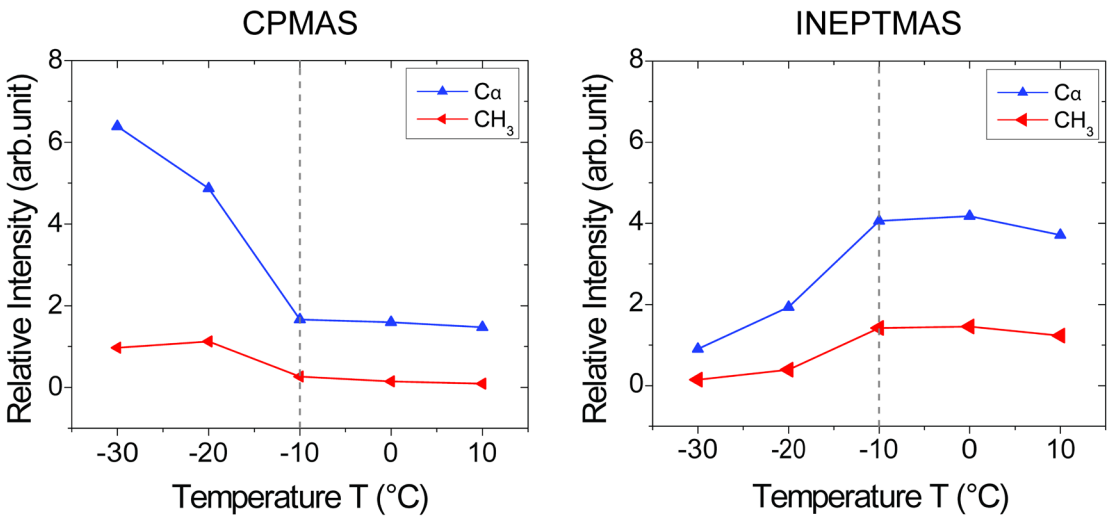

Fig. 3.7: Relative signal intensities from the representative regions of the 1D ^{13}C CPMAS and INEPTMAS spectra of [U-^{13}C,^{15}N\(K,V)]NP7-NO aggregates in the diamagnetic form plotted as a function of temperature. The representative regions correspond to the average chemical shifts for C_α (55 ppm) and Ile C_δ (14 ppm) respectively. The dotted grey lines at -10°C indicate the process of freezing below this temperature.

3.4 Aggregates are well ordered and yield resolved NMR spectra

To further elucidate the sample state and to probe structure and order of the protein aggregates, we recorded homo- and heteronuclear 2- and 3D CC and NCACB spectra of diamagnetic [U-^{13}C,^{15}N\(K,V)]NP7-NO. In figure 3.8, the aliphatic regions of the (a) 2D ^{13}C-^{13}C DREAM spectrum and (b) a 2D plane from the 3D NCACB spectrum of [U-^{13}C,^{15}N\(K,V)]NP7-NO are displayed. The 2D ^{13}C-^{13}C DREAM spectrum has excellent dispersion with ^{13}C line widths less than 1 ppm for the well resolved peaks. The easily identifiable spin systems from the aliphatic region of the 2D ^{13}C-^{13}C DREAM spectrum from Ala, Ile, Pro, Ser and Thr are represented in rectangles. Distribution of peaks and the dispersion of the cross-peaks especially in the Ala region display chemical shifts characteristic for the α-helices, random coil, and β-sheets

indicating that the fold of the NP7 is preserved. Since the biosynthesis of Leu involves Val as a precursor, thus resulting in deficient labeling of Leu, the spectrum is also lacking cross-peaks from the Leu residues[132-134]. This explains the observed mass difference of 63 Da between the recorded and the expected mass of [U-^{13}C,^{15}N\(K,V)]NP7 (Table 3.1). The 3D NCACB spectrum recorded at -30°C is also well resolved with good chemical shift dispersion in the ^{15}N dimension. Intra-residual assignments are shown from the finger print regions of the spectra for distinct Ala and Thr residues (dotted gray lines).

In order to clarify whether the INEPT signals arise from monomers present in the sample or from flexible parts of the aggregated proteins, we recorded a 2D ^{13}C-^{13}C INEPT-TOBSY (*i*nsensitive *n*uclei *e*nhanced by *p*olarization *t*ransfer-*to*tal through *b*ond correlation *s*pectroscop*y*)[69-71] spectrum (Fig. 3.9, red sub spectrum). Cross peaks for all spin systems of all amino acid types could be identified; however, most cross peaks show chemical shifts typical for random coil conformation (Table 3.3). Thus we can conclude that these resonances are either due to unfolded monomers or from flexible loop regions without defined secondary structure undergoing high amplitude fluctuations at time scales <10^{-6} s. A comparison with the DREAM spectrum as well as with chemical shifts predicted with SHIFTX2[135] (Fig. 3.9) demonstrates that the INEPT spectrum shows a different set of resonances with strongly reduced secondary chemical shifts for all observed amino acids, although some shift dispersion is observed for Pro, Thr and Ser.

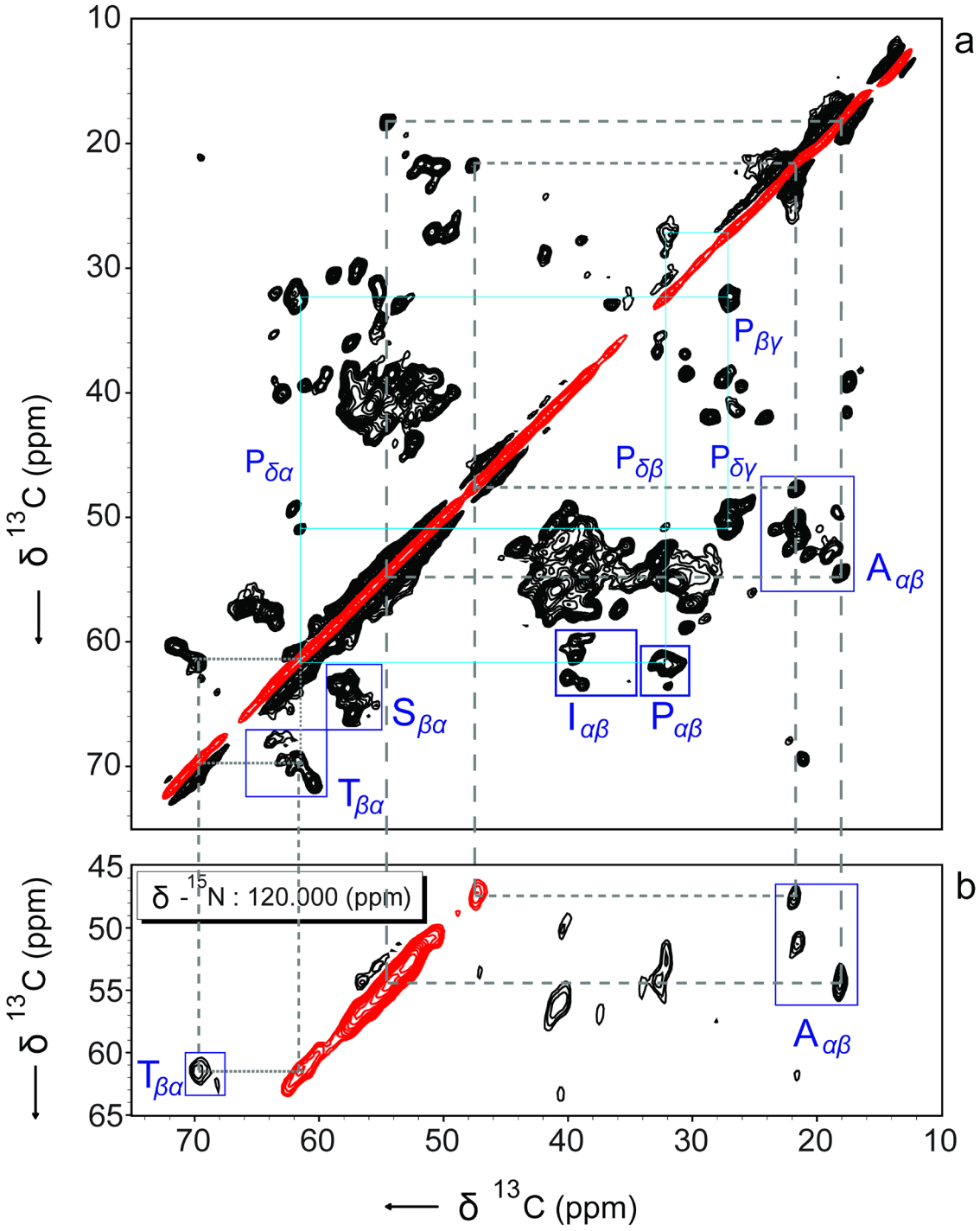

Fig. 3.8: Aliphatic regions of the (a) 2D ^{13}C-^{13}C DREAM and (b) 2D plane from 3D NCACB spectrum of [U-^{13}C,^{15}N\(K,V)]NP7-NO recorded using 15 kHz MAS and at -30°C. The DREAM transfer during the mixing unit was set to 1.6 ms. Data were processed with a combination of an exponential and a Gaussian function (-150 Hz exponential, Gaussian factor 0.2). Finger print

regions from Ala, Ile, Pro, Ser, and Thr are shown in blue rectangles with intra-residual assignments represented for the Ala and Thr residues using dotted grey lines. Side chain walk for the Pro residue is shown by colored lines (cyan).

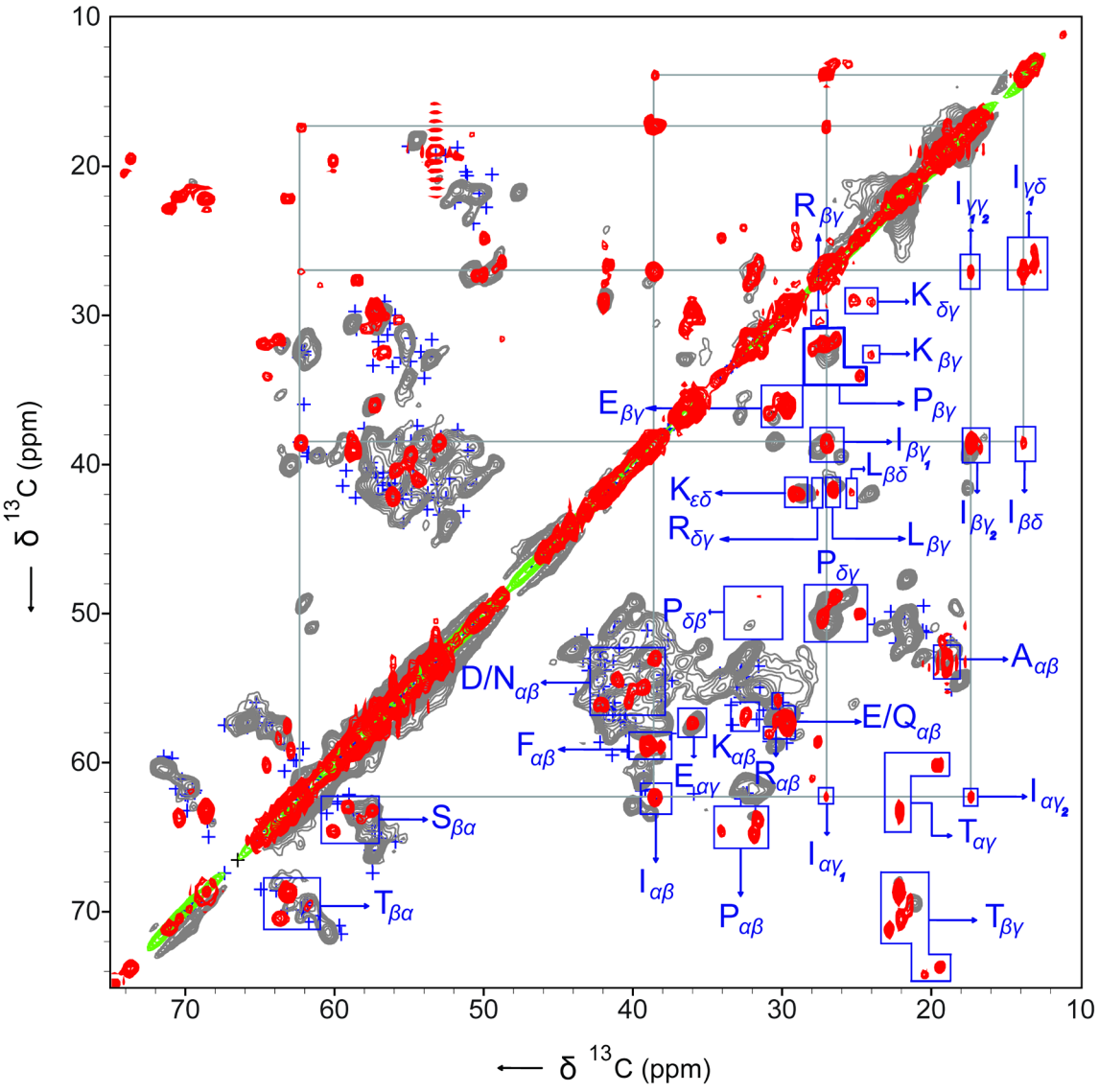

Fig. 3.9: Overlay of the aliphatic regions of the 2D ^{13}C-^{13}C INEPT-TOBSY (red) and 2D ^{13}C-^{13}C DREAM (grey) spectra of the [U-^{13}C,^{15}N\(K,V)]NP7-NO aggregates onto the SHIFTX2 [135] predictions (blue crosses). Both the spectra were recorded at a ^{1}H Larmor frequency of 600 MHz (14.1 T) with 2 s recycle delay. The INEPT-TOBSY spectrum was recorded with 11 kHz MAS,

1.725 ms of ^{1}H-^{13}C dephasing delay and 6 ms ^{13}C–^{13}C TOBSY mixing time at 10°C. The ^{13}C-^{13}C DREAM spectrum was recorded with 15 kHz MAS, 1.6 ms of ^{13}C–^{13}C DREAM mixing at -30°C. Assignments from the representative regions of the INEPT-TOBSY spectra are shown in blue rectangles. One and two bond correlations from the Ile residue are marked by grey lines and the one bond correlation from the Arg residue is shown by green lines.

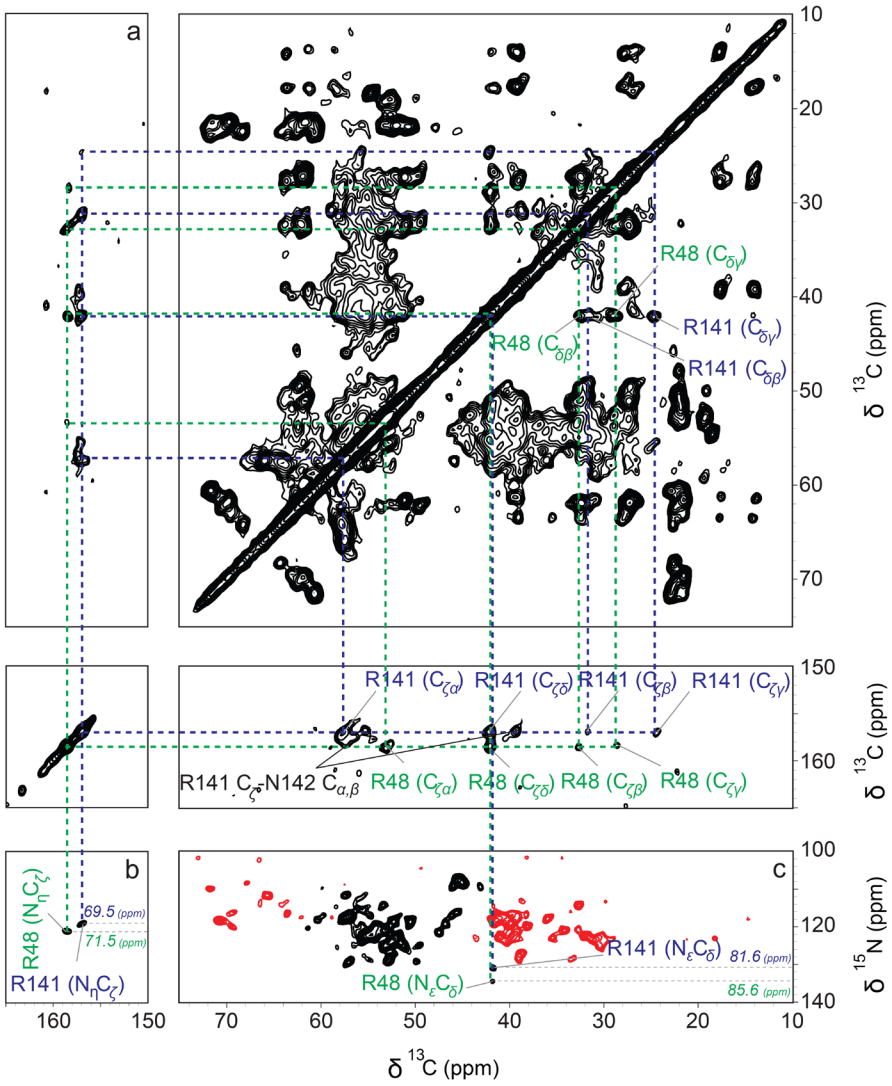

Fig. 3.10: Chemical shift assignments of R48 and R141 based on (a) homo-nuclear 2D ^{13}C-^{13}C PDSD spectrum and (b) heteronuclear 2D ^{15}N-^{13}C correlation spectrum from

U[^{13}C,^{15}N\(K,V)]NP7-NO. Inter-residual cross peaks between C_ζ of R41 and the C_α and C_β of N142 are shown in black letters.

Residue types	**Frequency of occurrence**	**INEPT-TOBSY**	**C_α (ppm)**	**C_β (ppm)**	**δC_α (ppm)**	**δC_β (ppm)**	**$\Delta\delta(C_\alpha$-$C_\beta)$ (ppm)**
Ala	12	1	56.1	19.0	0.1	-0.1	0.2
Arg	2	1	57.2	30.5	0.4	-0.1	0.5
			56.1	42.0	1.4	1.1	0.3
			54.3	41.0	-0.4	0.1	-0.5
Asp/Asn	24	5	53.0	38.4	-1.6	-2.5	0.9
			55.8	40.3	2.3	1.6	0.7
			54.9	39.3	1.4	0.6	0.8
			44.4				
Gly	10	3	43.7				
			43.5				
Ile	7	1	62.2	38.5	0.6	-0.1	0.7
			64.8	31.8	1.5	-0.1	1.6
Pro	7	3	63.9	31.6	0.6	-0.3	0.9
			64.5	34.0	1.2	2.1	-0.9
			60.1	64.6	1.4	0.8	0.6
Ser	13	4	58.3	63.8	-0.4	0.0	-0.4
			57.5	63.2	-1.2	-0.6	-0.6
			59.1	62.9	0.4	-0.9	1.1
Thr	12	3	63.6	70.4	1.4	0.8	0.6
			61.8	69.6	-0.4	0.0	-0.4

			63.1	68.6	0.9	-1.0	1.9
			57.3	29.6	0.0	-0.5	0.5
Glu/Gln	13	3	58.0	30.9	0.7	0.8	-0.1
			57.1	30.3	-0.2	0.2	-0.4
Phe/Tyr	10	2	58.7	39.0	0.6	-1.0	1.6
			58.9	38.1	0.8	-1.3	2.1

Table 3.3: Secondary chemical shift analysis of the identified residue types from the homo-nuclear 2D ^{13}C-^{13}C INEPT-TOBSY spectrum from U[^{13}C,^{15}N\(K,V)]NP7-NO aggregates recorded at 10°C. Average random-coil chemical shift values were taken from BMRB[136].

	N	C'	C_α	C_β	C_γ	C_δ	C_ζ	N_ε	$N_{\eta1,2}$
R48 (CPMAS)	121.7	173.8	53.1	32.6	28.6	42.0	158.5	85.6	71.5
R141 (CPMAS)		176.5	57.3	31.7	24.4	42.1	156.9	81.6	69.5

Table 3.4: Chemical shift assignments of R48 and R141 based on CPMAS spectra of U[^{13}C,^{15}N\(K,V)]NP7-NO aggregates. Random coil chemical shifts from the BMRB are shown for a comparison.

	N	C'	C_α	C_β	C_γ	C_δ	C_ζ	N_ε	N_ε	$N_{\eta1,2}$	NH_ε	$NH_{\eta1,2}$
INEPTMAS		176.1	57.2	30.5	27.6	41.9		85.5	87.3	74.6	7.6, 6.4	5.5

Table 3.5: Observed chemical shifts of Arg residue based on INEPTMAS spectra from U[^{13}C,^{15}N\(K,V)]NP7-NO.

3.5 Conformational heterogeneity of arginine side chains

Out of the two Arg residues, the INEPT-TOBSY spectrum obtained at higher temperature (10°C) revealed signals only from one Arg residue with reduced secondary chemical shift. The observed C', C_α and C_δ chemical shifts were very much similar to that Arg141. However, a difference of 1.2 ppm and -3.2 ppm were observed in the case of C_β and C_γ chemical shifts respectively between the CPMAS and INEPTMAS spectra (Table 3.4, 3.5). INEPT based schemes are generally used to detect dynamic systems, so that average chemical shift values are observed due to motional averaging. Since the CPMAS spectra were recorded at -30°C and the INEPT-TOBSY spectrum at 10°C, the observed differences in chemical shifts for C_β and C_γ could be either due to temperature induced conformational changes upon freezing, or due to the presence of entirely different side-chain conformations.

Temperature induced chemical shift changes could be verified by monitoring the differences in C_β and C_γ chemical shifts upon decrease in temperature. Since the Arg C_β and C_γ chemical shifts were not well separated from the aliphatic chemical shifts from other amino acid residues, temperature dependent 1D ^{13}C CPMAS and 90° pulse spectra of the Arg C_ζ were recorded (fig. 3.11). As there are no directly bound protons to the Arg C_ζ carbon atom, INEPTMAS spectra did not reveal any C_ζ signals. The Arg C_ζ signals were further identified and confirmed from the rest of the Tyr C_ζ signals by comparing the spectra reverse labelled for Lys and aromatic residues (Phe and Tyr) termed U[^{13}C,^{15}N\(K,F,Y)]NP7 (fig. 3.12).

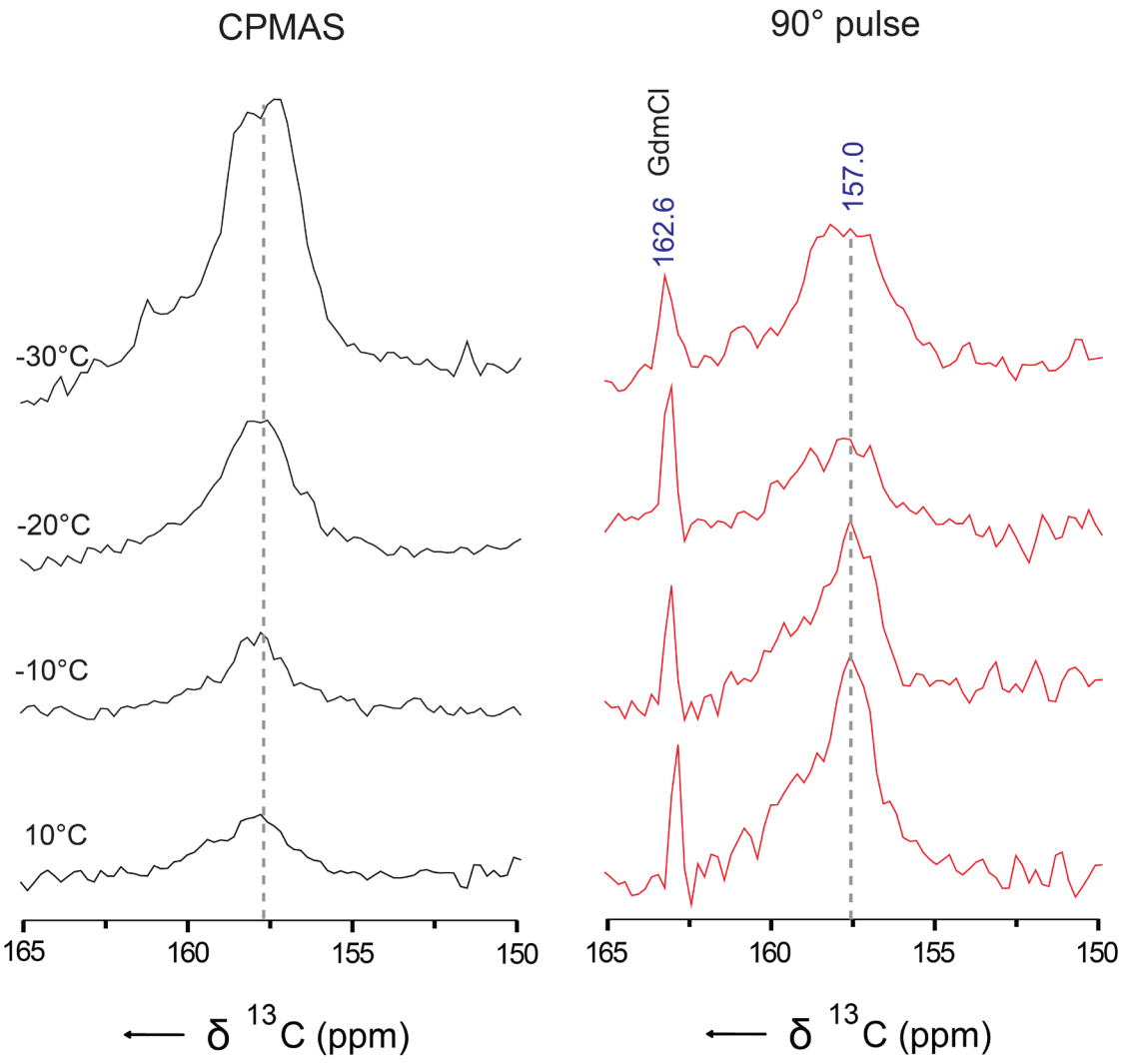

Fig. 3.11: Temperature dependent 1D ^{13}C CPMAS (left) and 90° pulse (right) spectra of (a) U[^{13}C,^{15}N\(K,V)]NP7-NO. Arg141 C_ζ peak in the 90° pulse experiment (red spectra, right) is shown by dotted grey line. The peak at 162.6 ppm appearing from Guanidinium chloride (GdmCl) is labeled.

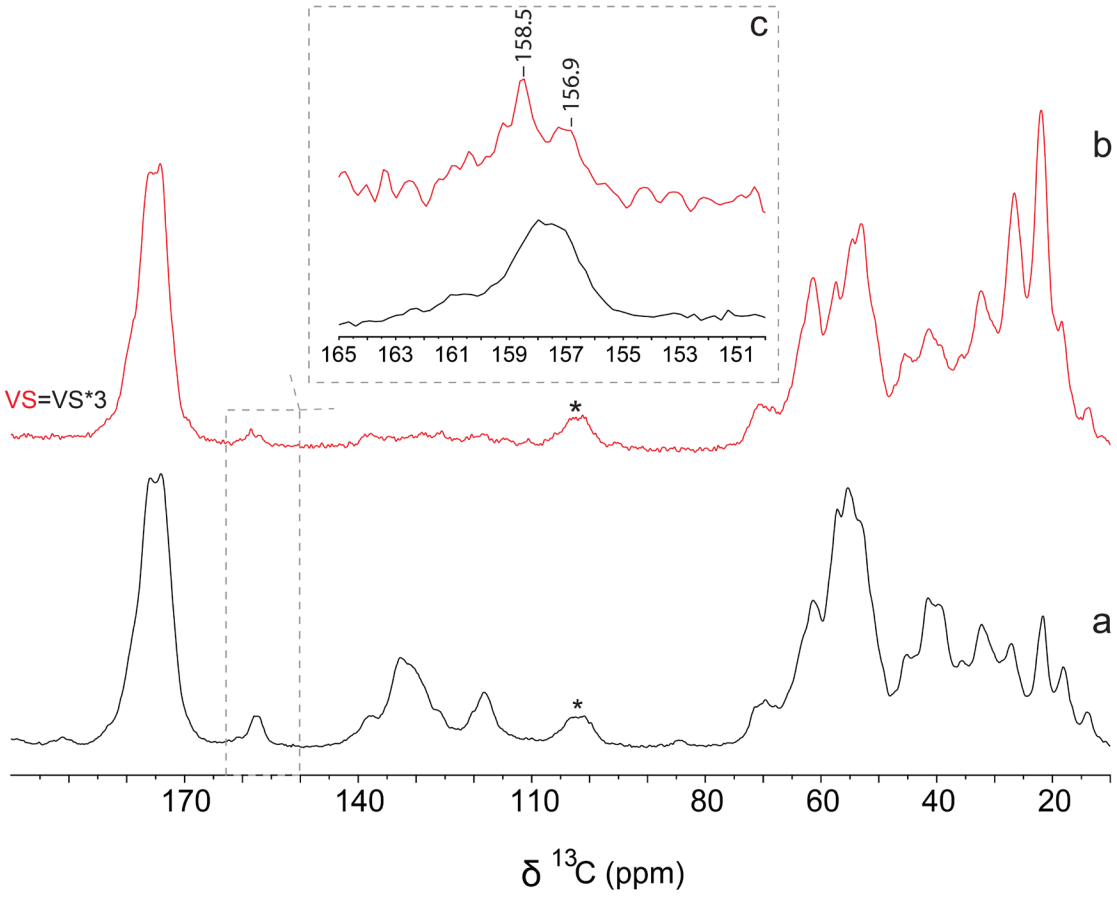

Fig. 3.12: 1D ^{13}C CPMAS spectra of (a) U[^{13}C,^{15}N\(K,V)]NP7 sample reversely labelled for Lys and Val (b) U[^{13}C,^{15}N\(K,F,Y)]NP7 sample reversely labelled for Lys, Phe and Tyr (c) zoomed in aromatic regions (150-165 ppm) from the Tyr and Arg residues. First order spinning side bands are shown by asterisks. Both the spectra were recorded at -30°C.

Compared to the CPMAS experiment which works efficiently for rigid samples with no or reduced mobility, 90° pulse excitation is not sensitive to mobility and can be used to excite both rigid and dynamic parts of the protein. This is evident from the 90° pulse spectra obtained at 10°C as it showed intense and sharp signal (4-fold) when compared to the CPMAS spectra obtained at the same temperature. In the case of 90° pulse spectra, no obvious chemical shift changes were observed for the R141 C_ζ peak at 157 ppm with respect to decrease in temperature from 10°C to -30°C. This observation is also in agreement with previous ssNMR studies about the activity of Arg in the proton-motive photocycle of bacteriorhodopsin, where the C_ζ carbon showed only a very small chemical shift range and a single resonance, even in cases where two

different crystal forms coexisted with different ε-^{15}N and η-^{15}N chemical shifts[138]. However it can be clearly seen that, the R141 C_ζ peak at ~157 ppm becomes broader and reduced in intensity with respect to decrease in temperature. This effect is significant below -10°C indicating a probable transition from disordered to ordered phase below this temperature. This is also in good agreement with the temperature dependent studies of the relative intensities from the representative regions (backbone C_α and side chain CH_3) of one-dimensional ^{13}C CPMAS and INEPTMAS spectra of [U-^{13}C,^{15}N\(K,V)]NP7-NO aggregates. The peak at 162.6 ppm which is not visible in the CPMAS spectrum could be probably arising from dynamic small molecules like Guanidinium chloride (GdmCl) did not show any significant line broadening between -10°C and -20°C. However, a reduction in intensity and line broadening could be observed at -30°C indicating a frozen state of the molecule. In the CPMAS spectra, the C_ζ peak of R141 at 157 ppm is not well separated from the rest of the C_ζ signals from tyrosine and arginine residues. However, the C_ζ peaks from the CPMAS spectra also became broader below -10°C and showed a 4-fold increase in intensity at -30°C when compared to the spectrum at 10°C. Similar behaviour of 4-fold increase in intensity of CPMAS signals was also observed in the case of temperature dependent studies indicating an onset of the quenching of local dynamics below -10°C.

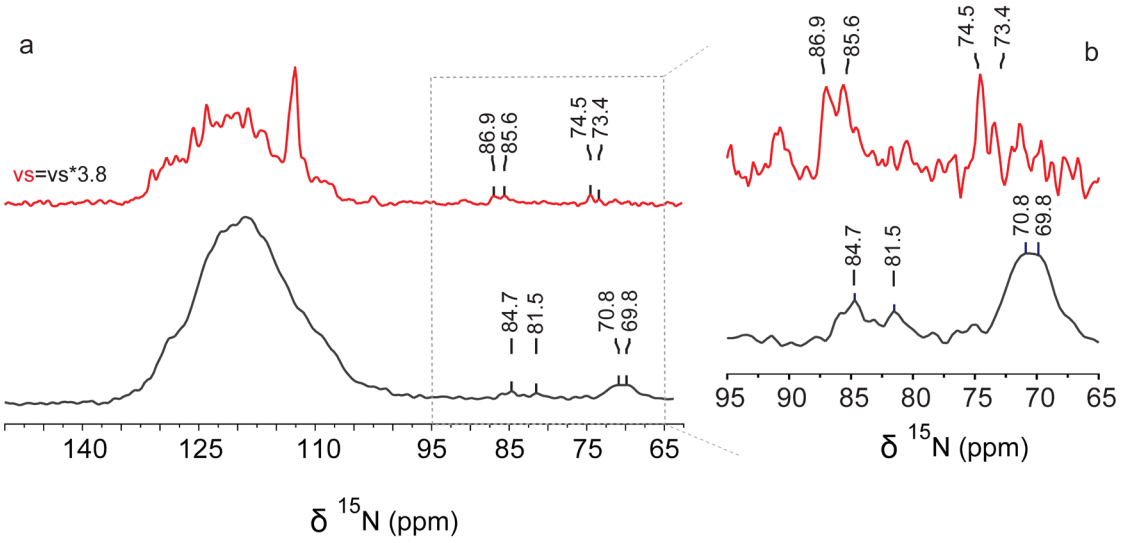

Fig. 3.13: 1D ^{15}N CPMAS (black) and INEPTMAS (red) spectra of (a) U[^{13}C,^{15}N\(K,V)]NP7-NO (b) zoomed in region (65-95 ppm) of the same spectra showing the ^{15}N chemical shifts from the Arg side chain guanidine groups. The CPMAS spectrum was recorded at -30°C and the INEPTMAS spectrum at 10°C.

To further cross check whether guanidinium groups of the Arg residues are involved in H-bonding, temperature dependent CPMAS and INEPTMAS spectra of ^{15}N chemical shifts from the guanidinium groups were compared (fig. 3.13). A comparison of the 1D ^{15}N INEPTMAS and CPMAS spectra of NP7 aggregates showed chemical shift difference between the nitrogen atoms from the guanidino groups. The INEPTMAS spectrum was recorded at 10°C and the CPMAS spectrum was recorded at -30°C. When compared to the broad ^{15}N backbone amide region (100 to 140 ppm) of the CPMAS spectrum, the INEPTMAS spectrum is characterised by the presence of well resolved signals as anisotropic interactions are completely averaged due to high mobility and due to magic angle spinning. However, a comparison of the ^{15}N chemical shifts from the guanidinium group of the Arg side chains based on the 1D ^{15}N CPMAS and INEPTMAS

revealed differences in chemical shifts. The ^{15}N chemical shift assignments based on the INEPTMAS spectra are summarized in table 3.5.

Single crystal X-ray diffraction (XRD) studies of pure L-arginine have not yet been reported. However, single-crystal XRD studies of L-arginine hydrochloride (L-arginine·HCl) have revealed the existence of two forms with two crystallographically inequivalent molecules (anhydrous L-arginine·HCl and the monohydrate L-arginine·HCl·H_2O) per asymmetric unit cell[139]. The conformation of the backbone comprising the C' and C_α carbons were nearly the same in the two forms, while the side-chain conformations were found to be entirely different, projecting out in two nearly perpendicular directions[139].

Previous ssNMR studies on L-arginine·HCl show that either one[140] or two sets[69,141,142] of ^{13}C resonances could be observed. The co-existence of two sets of ^{13}C resonances was ascribed either to two crystallographically inequivalent molecules in the asymmetric unit cell or due to two different crystal forms of L-arginine·HCl. Recently, two crystallographically and magnetically inequivalent molecules of L-arginine·HCl per asymmetric unit cell were disentangled using ssNMR by exploiting differential proton T_1 relaxation in conjunction with CP and dipolar ^{13}C-^{13}C and ^{15}N-^{15}N 2D correlation experiments[11]. Very recently, crystal structure of L-Arginine has been reported based on powder XRD data[143]. The lack of single crystal X-ray structure of pure L-Arginine was ascribed to the difficulties in obtaining crystals of sufficient size and quality for single-crystal XRD studies[143]. Based on the powder XRD data, two crystallographically independent molecules with very similar conformations were reported. This was further supported by ^{13}C CPMAS ssNMR spectrum in which C' (~178 ppm) and C_β (~30 ppm) were in different environments, showing two peaks (in approximately 1:1 intensity ratio),

suggesting the co-existence of two crystallographically independent molecules in the asymmetric unit cell.

Previous reports based on the X-ray crystal structure of L-arginine·HCl revealed that the Arg molecule is free to adopt a variety of conformations according to the available hydrogen bonding partners in the near vicinity[139,143]. Solution state NMR studies on ^{15}N chemical shifts of guanidinium and guanidino forms of L-arginine·HCl revealed that the rotation about the C_ζ-N_ε bond is rapid at room temperature, so that a single averaged chemical shift is normally observed for N_η nitrogen atoms[144]. However, isomerization was found to be slowed at very low temperatures (-52° C) and the chemical shift differences between the two non equivalent N_η nitrogens were found to be as large as 40 ppm[144]. Furthermore, ssNMR studies by Petkova et al. have shown that nitrogen atoms of the guanidyl group of the protonated Arg side chains were found to participate in H-bonds and exhibited a wide range of chemical shifts[138]. The chemical shifts of the N_ε nitrogens were found to vary from 68.9 to 56.3 ppm, while the N_η chemical shifts varied from 62.0 to 45.6 ppm for the downfield resonance and from 46.8 to 34.2 ppm for the upfield resonance[138].

The preliminary X-ray structure of NP7[35] shows a moderate H-bond (2.8 Å) between $N_{\eta 1}$ of R141 and the backbone carbonyl group of S22 (fig. 3.14). Similarly, H-bonds could also be observed for $N_{\eta 1}$ of R48 and the backbone carbonyl groups of G23 (2.8 Å) and P47 (2.9 Å). Therefore, observed differences in changes in chemical shift of ^{15}N from the guanidino groups of Arg could be ascribed to the formation of H-bonds between the nearby acceptor groups upon freezing. This could be further confirmed by checking the temperature induced changes in ^{15}N chemical shifts using 90° pulse experiments. However, 90° pulse experiments on ^{15}N were not successful. Since X-ray crystal structure of NP7 is obtained at cryogenic temperatures and differs from the temperatures employed during the NMR studies, dynamic information about the

formation and breaking of H-bonds could be gained from MD simulations and would be rewarding in this context.

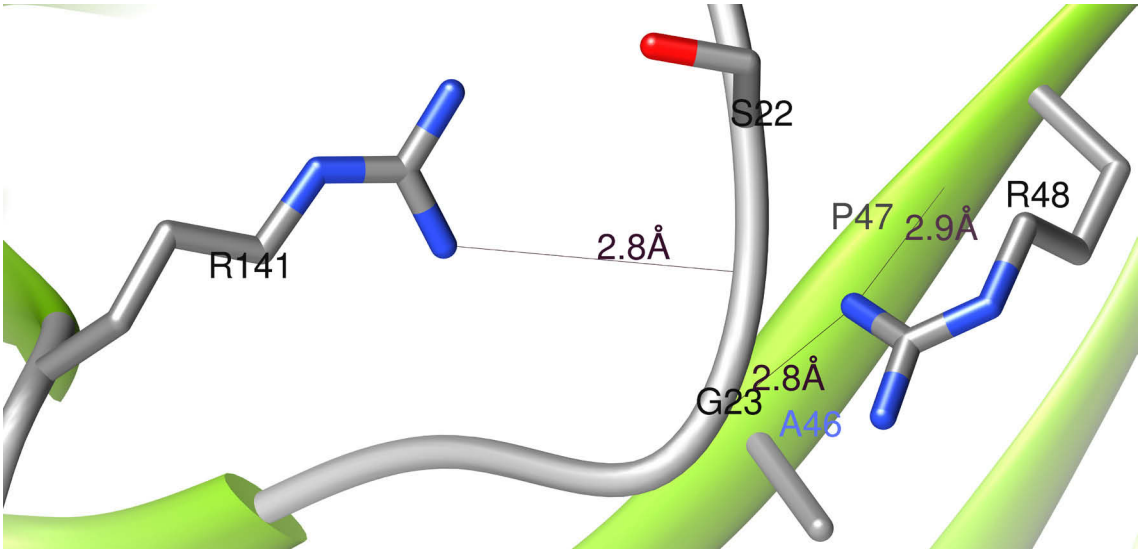

Fig. 3.14: H-bonding between $N_{\eta 1}$ of R141 and the backbone carbonyl group of S22. Similarly, H-bonding between $N_{\eta 1}$ of R48 and the backbone carbonyl groups of G23 and P47.

Conformational heterogeneity of side chains from R141 is also evident from the relatively broad R141 C_ζ-C_α crosspeak observed in the 2D ^{13}C-^{13}C PDSD spectra, when compared to the C_ζ-C_α cross peak from R48 (fig. 3.10). Previous reports based on DLS (dynamic light scattering) measurements revealed that in solution, NP7 contained a large fraction of oligomers. The apparent hydrodynamic diameters of the oligomers were of the order of ~250 - 400 Å, which corresponds to oligomers of approximately 6 to 10 units[36]. This was also evident from the distribution of signals with different diffusion coefficients observed from the solution state DOSY measurements indicating a heterogeneous mixture of oligomers (fig. 3.3).

3.6 Resonance assignments and comparison to data from X-ray crystallography

For the diamagnetic sample, we obtained site-specific assignments for 22 residues from a set of 2D ^{13}C-^{13}C (PDSD, DREAM, DQ-SQ), 2D ^{15}N-^{13}C (NCA, NCO, NCACB, NCACX, NCOCX) and 3D ^{15}N-^{13}C (NCACB, NCACX and NCOCX) correlation spectra. Furthermore, we could identify and assign residue specific spin systems for 78 amino acids: 12×Ala, 2×Arg, 10×Asp/Asn, 1×Cys, 8×Glu/Gln, 9×Gly, 2×His, 5×Ile, 11×Phe/Tyr, 4×Pro, 6×Ser, and 8×Thr. The amino acid type specific intra-residual assignments were first established from a series of 2D ^{13}C-^{13}C, 2D and 3D ^{15}N-^{13}C (NCACB, NCACX) correlation spectra (Fig. 3.8, 3.10). An example for intra-residual NCACB correlations for two distinct Ala and one Thr residues is shown (Fig. 3.8).

Inter-residual site-specific assignments were established by linking ^{15}N chemical shifts of the i^{th} amino acid residue to the COCX of the previous residue $(i-1)^{th}$ using 2D and 3D NCOCX spectra with the summary of the identified chemical shifts (Fig. 3.15, Table 3.6). Site specific information was also obtained from inter-residual cross peaks in spin diffusion spectra (Fig. 3.16) recorded at longer spin diffusion mixing times (100 ms) under weak coupling conditions[145].

Since ssNMR and X-ray crystallography can act as complementary techniques[11,146], some conclusions can be drawn based on the preliminary crystal structure of NP7 (resolution 1.8 Å)[35]. To gain further insights about the rigid and flexible regions, crystallographic B-factor (Debye-Waller factor)[147,148] values of the backbone C_α atoms along the NP7 residues were analysed (fig. 3.17a). Schematic representation of the NP7 secondary structure is displayed on the top (fig. 3.17c) indicating eight β-strands (A-H) along with two major α-helices (α1, α2) according to the

convention based on Kondrashov et. al[30]. Our resonance assignments agree reasonably well with the preliminary X-ray crystal structure of NP7 (resolution 1.8 Å) (Fig. 3.17c).

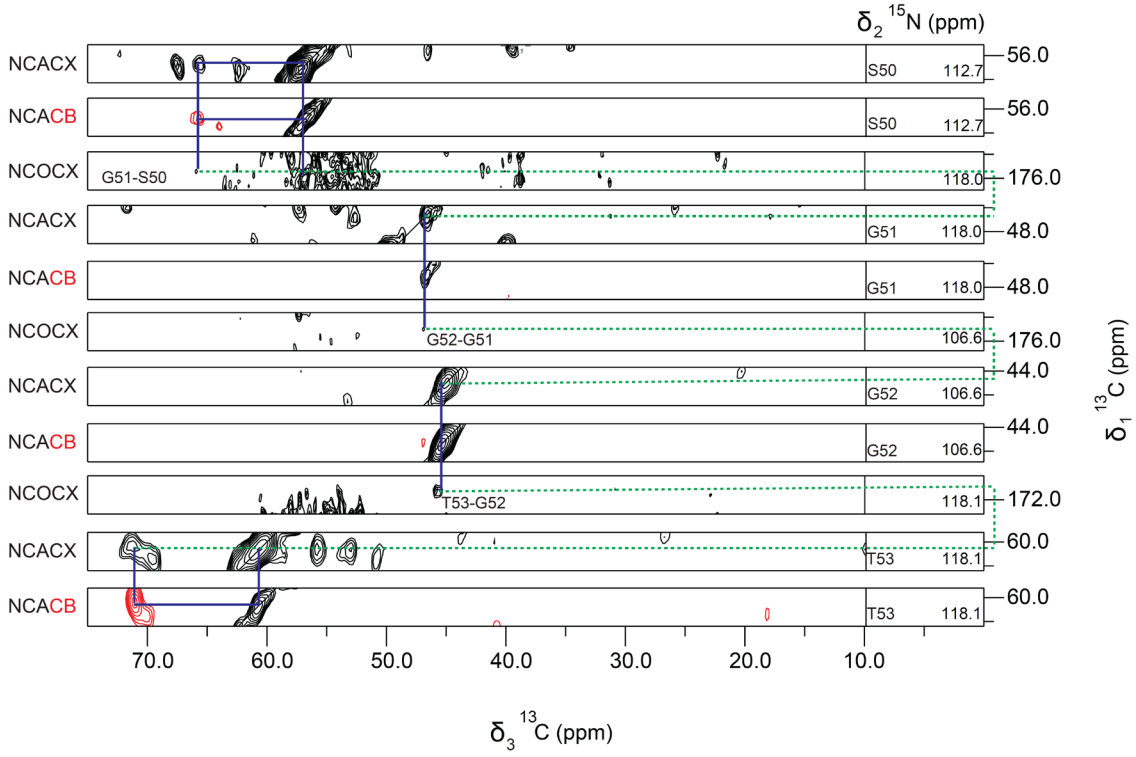

Fig. 3.15: Strip plot showing the sequential assignments from T53 to S50. Intra-residual assignments are shown by blue lines and inter-residual assignments are shown by dotted green lines. The 3D NCACB spectrum was obtained using 512 number of scans with 3.3 ms acquisition time in the in the first indirect dimension, 4 ms in the second indirect dimension and 13 ms in the direct dimension. The data were processed using a combination of an exponential (-150, -150, -50 Hz) and a Gaussian function (Gaussian factor 0.2, 0.2, 0.2) in the direct dimension, first indirect dimension and second indirect dimension respectively. The 3D NCACX spectrum was obtained using 400 number of scans with 3.3 ms acquisition time in the in the first indirect dimension, 4 ms in the second indirect dimension and 13 ms in the direct dimension. The data were processed using a combination of an exponential (-150, -50, -50 Hz) and a Gaussian

function (Gaussian factor 0.2, 0.2, 0.2) in the direct dimension, first indirect dimension and second indirect dimension respectively. The 3D NCOCX spectrum was obtained using 512 number of scans with 4 ms acquisition time in the in the first indirect dimension, 3 ms in the second indirect dimension and 13 ms in the direct dimension. The data were processed using a combination of an exponential (-50, -50, -50 Hz) and a Gaussian function (Gaussian factor 0.2, 0.2, 0.2) in the direct dimension, first indirect dimension and second indirect dimension respectively.

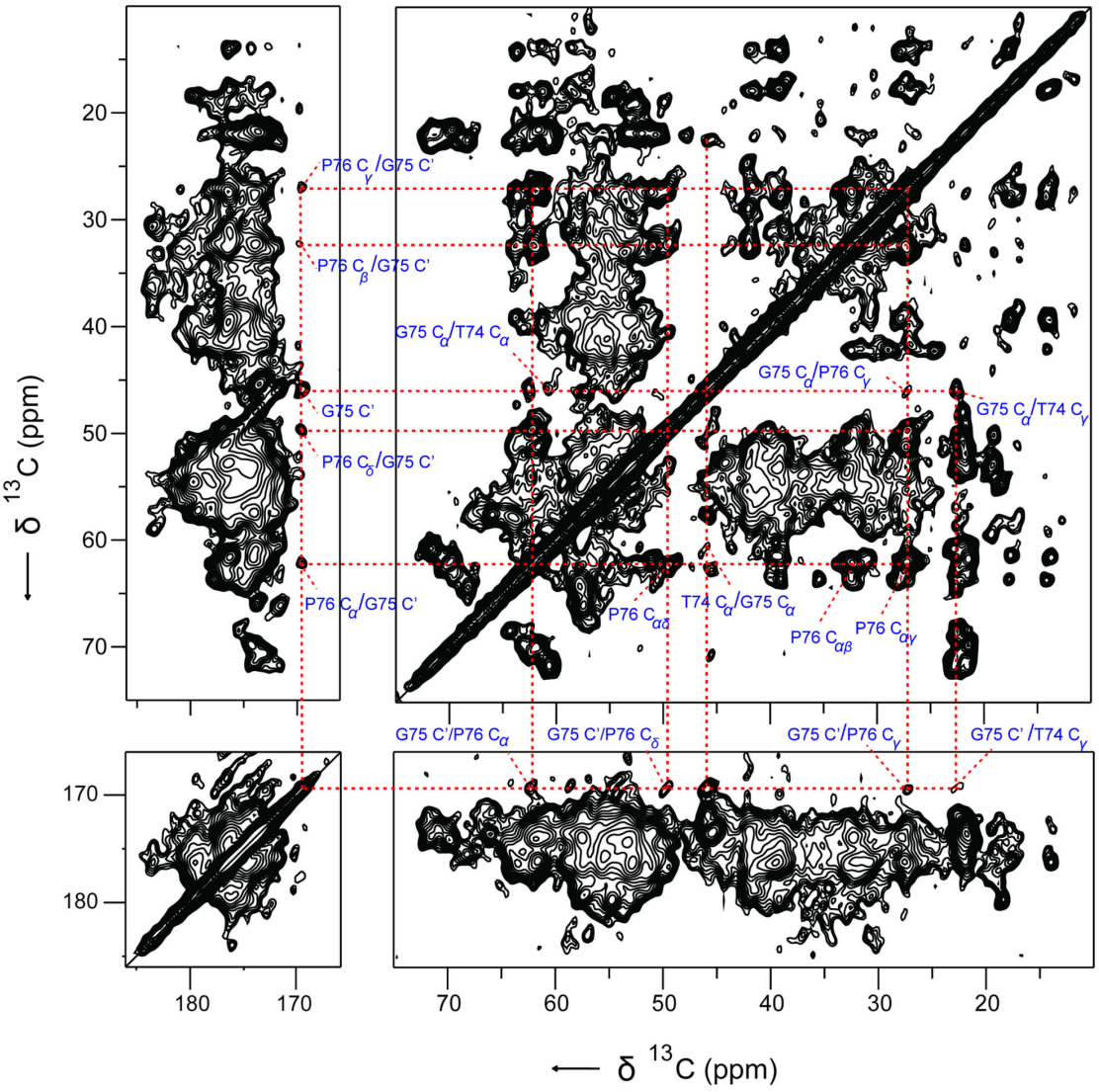

Fig. 3.16: Selected regions of the 2D ^{13}C-^{13}C PDSD spectra of [U-^{13}C,^{15}N\(K,V)]NP7-NO with a spin diffusion mixing time of 100 ms. The spectrum was recorded at a ^{1}H Larmor frequency of 600 MHz (14.1 T) at 11 kHz MAS and at -30°C. The data were processed with combination of an exponential and a Gaussian function (-150 Hz exponential, Gaussian factor 0.2). Inter-residual cross peaks from the unique pairs (G75-P76) from the NP7 sequence are labelled in blue.

	N	**C'**	**C_α**	**C_β**	**C_γ**	**C_δ**	**C_ε**	**C_ζ**	**N_ε**	**$N_{\eta 1,2}$**
S22	113.1	173.6	57.3	65.8						
G23	106.8	173.5	45.3							
T24	119.3	174.1	61.4	70.4	22.1					
F45		172.3	56.1	41.4	134.3	132.1	129.0			
A46	121.7	174.0	52.8	22.3						
P47	135.4	177.1	61.9	32.4	27.1	51.0				
R48	121.7	173.8	53.1	32.6	28.6	42.0		158.5	85.6	71.5
E49	121.8	173.1	56.0	31.7	36.5	181.6				
S50	112.7	175.1	57.5	63.9						
G51	118.0	174.8	46.8							
G52	106.6	171.3	45.3							
T53	118.1	173.9	60.4	71.2	22.3					
T72		175.1	60.5	71.1	22.0					
G73	116.6	171.4	45.8							
T74	117.4	173.3	60.4	71.5	22.6					

G75	116.1	169.5	46.0						
P76	131.8	177.6	62.2	32.1	27.1	49.5			
I112	128.4	176.4	63.4	38.8	27.8/17.6	14.1			
E113	114.4	176.7	53.7	32.9	36.8	180.6			
A114	126.2	174.4	50.7	21.8					
R141		176.5	57.3	31.7	24.4	42.1	156.9	81.6	69.5
N142	122.1		55.4	39.4					

Table 3.6: List of chemical shift assignments from the diamagnetic [U-^{13}C,^{15}N\(K,V)]NP7-NO sample.

NP7 contains a β-barrel made up of eight anti parallel β-strands consisting of 79 residues in total, and two main α-helices (α1, α2) in the C-terminus comprising 16 residues. Secondary chemical shifts of the site-specifically assigned residues based on CPMAS spectra show predominantly β-strand character (Fig. 3.17b). Previous reports on other nitrophorins (NP1-4) have revealed that eight anti parallel β-strands are the best ordered in the structure while the connecting loops showed high flexibility[26,30,31,36,127,149-155]. Furthermore, an apo structure of rNP4 at 1.11 Å resolution revealed the beta-barrel of rNP4 remains a rigid structure even in the absence of its heme cofactor and is similar to that of holo rNP4[31]. Flexibility and functionality of the loop regions of nitrophorins (NP1-4) had also been studied extensively based on several biophysical methods[30,36,149,151-153,156-159]. A comparison of the 2D ^{13}C-^{13}C DREAM spectrum with the chemical shifts predicted using SHIFTX2 using the preliminary X-ray structure are in good agreement (Fig. 3.9). This indicates that even though we are looking at insoluble precipitates, the native fold of the protein is found to be well preserved.

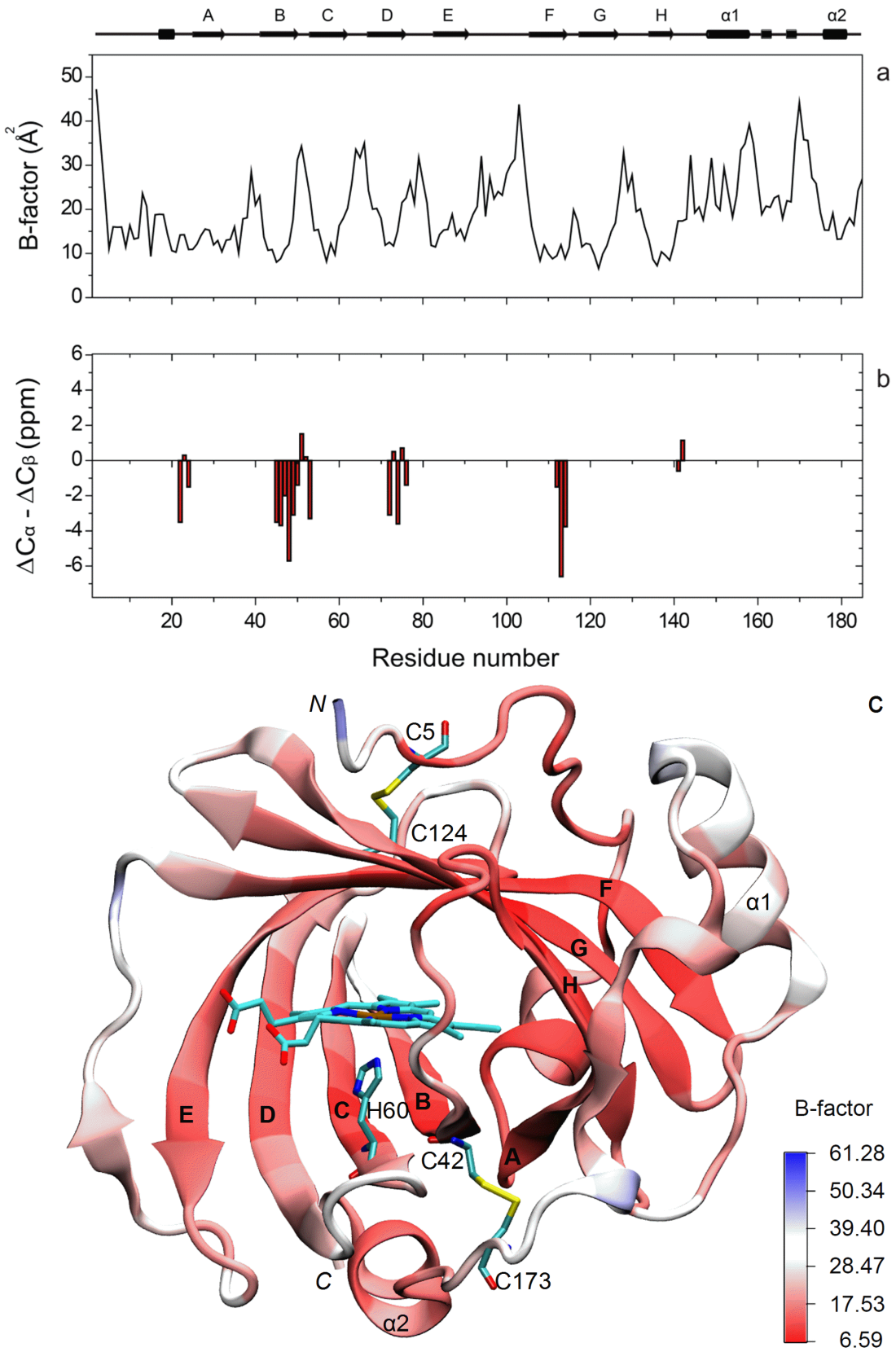
A
B
C
D
E
F
G
H
α1
α2
a
B-factor (Å²)
50
40
30
20
10
0
b
ΔCα - ΔCβ (ppm)
6
4
2
0
-2
-4
-6
20
40
60
80
100
120
140
160
180
Residue number
c
N
C5
C124
F
α1
G
H
E
D
C
H60
B
C42
A
C
C173
α2
B-factor
61.28
50.34
39.40
28.47
17.53
6.59

Fig. 3.17: (a) The X-ray crystallographic B-factor values of the backbone C_α atoms along the NP7 residues. Schematic representation of the NP7 secondary structure based on STRIDE secondary structure analysis is displayed on the top. (b) ^{13}C secondary chemical shifts of NP7 based on site specific sequential assignments. The secondary chemical shifts based on sequential assignments are calculated as, ΔC_α = C_α (Experimental) - C_α (BMRB) and ΔC_β = C_β (Experimental) - C_β (BMRB). (c) Modified cartoon representation of NP7 (P2-K185) crystal structure. In agreement with fig. 3.17(a), colouring scheme is based on the X-ray crystallographic B-factor values. The main β-strands are designated from A to H in bold letters along with two main α-helices. The N- and C-termini are designated with italic letters. The four disulfide-forming Cys residues, the heme cofactor, and the proximal His-60 are displayed by "Licorice" drawing scheme. Fig. 3.17(c) was rendered using VMD.

3.7 Pseudocontact shifts

Depending on the ligand bound to the heme centre, NP7 can adopt different electronic spin states. Fig. 3.18 displays an overlay of the aliphatic regions of the 2D ^{13}C-^{13}C DREAM[57] spectra of LS [U-^{13}C,^{15}N\(K,V)]NP7-ImH (black) and diamagnetic [U-^{13}C,^{15}N\(K,V)]NP7-NO (red). The spectra were optimized for efficient ^{13}C-^{13}C transfer in the aliphatic region by setting the carrier frequency at 57 ppm and were recorded under identical experimental conditions. The spectra obtained from both electronic spin states are well resolved and are almost identical. However, minor differences occur for some resonances in the 2D ^{13}C-^{13}C DREAM spectra, which can potentially be ascribed to PCS[160-163]. For example, high-frequency shifts of 0.8 and 3.2 ppm for C_β resonances of two Ile residues are observed in the spectrum of the LS form (Fig. 3.18c). PCSs can be approximated[94] (Eqn. 1.19, Chapter 1) from the main values of the *g*-tensor[36], the orientation of the g-tensor within the molecular frame[164] and respect to the heme

group and the X-ray crystal structure[35]. For a nucleus at a distance of 12 Å from the electron spin will range between 1.3 and -1.0 ppm, for a nucleus at a distance of 6.8 Å between 7.9 and -6.7 ppm. In total, 3 Ile residues (Ile 121, Ile 123 and Ile 132) are in close enough proximity (Table 3.7 and 3.8) to the heme centre to explain for these shift differences. The z-axis of the g-tensor was found close to perpendicular to the heme plane. For Ile123 and Ile 132, positive PCS can be expected, whereas for Ile 121 the PCS should be negative. Thus, the two positively shifted cross-peaks may be tentatively assigned to Ile123 and Ile 132. Negative PCS could, however, not be observed, which may be due to signal overlap.

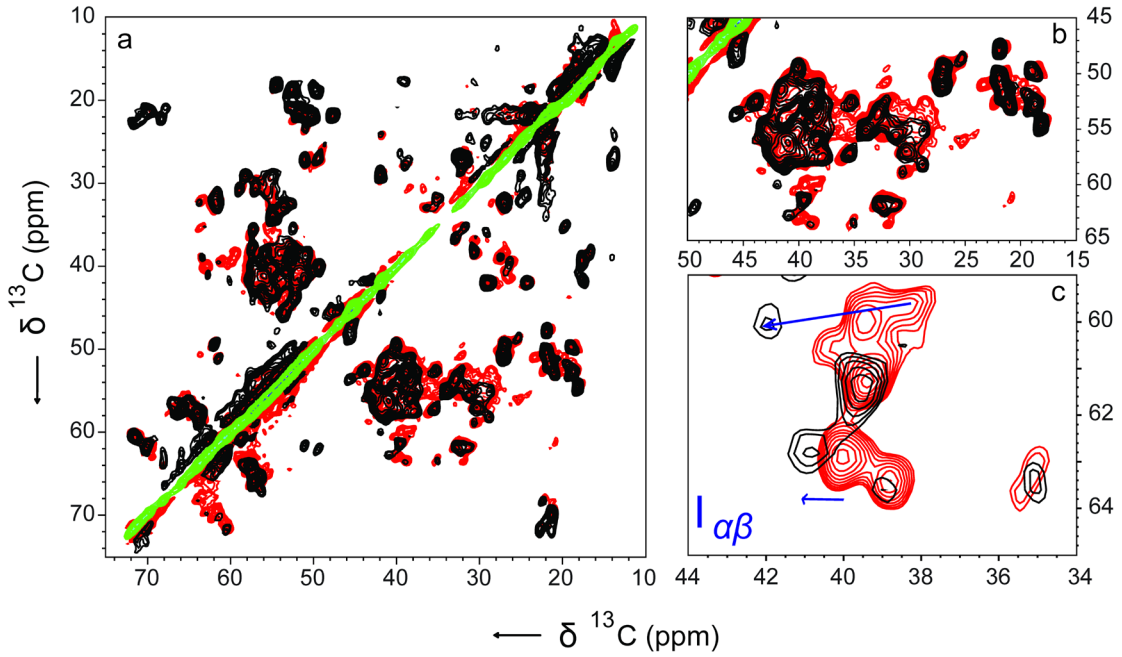

Fig. 3.18: Overlay of the aliphatic region of the 2D ^{13}C-^{13}C DREAM correlation spectra of [U-^{13}C,^{15}N\(K,V)]NP7-ImH (black) [U-^{13}C,^{15}N\(K,V)]NP7-NO (red) recorded using a spinning frequency of 15 kHz and at -30°C. The selected regions of the same spectra correspond to (b) aliphatic C_α-C_β and (c) Ile C_α-C_β. The DREAM transfer during the mixing unit was set to 1.6 ms. The other acquisition parameters are 0.3 ms ^{1}H-^{13}C CP contact time, 83 kHz ^{1}H SPINAL decoupling, 5 ms acquisition time in the indirect dimension with States detection, 13 ms

acquisition time in the direct dimension, 2 s recycle delay. The data were processed with a combination of an exponential and a Gaussian function (-150 Hz exponential, Gaussian factor 0.2), and zero filled to 512 (F2) x 4096 (F1) complex points.

Residue Type	Residue Number	Distance from the Fe^{III} centre and C_β of Ile residues (Å)	Secondary structure (STRIDE)
Ile	10	21.2	random coil
	98	17.6	β-strand
	112	16.6	β-strand
	121	11.0	β-strand
	123	6.8	β-strand
	132	12.2	β-strand
	151	19.0	α-helix

Table 3.7: Distance measurements of Ile residues based on the preliminary X-ray crystal structure coordinates. STRIDE[137] secondary structure is based on the available crystal structure of NP7[35].

Residue Number	Distance from the Fe^{III} centre and C_β of Ile residues (Å)	Angle (θ) between the Fe^{III}-Ile distance vector and g_z axis	δpcs, Calculated (ppm)
Ile 121	11.09	76°	-1.36 to -0.16
Ile 123	6.85	45°	0.6 to 3.3
Ile 132	12.27	28°	0.73 to 0.92

Table 3.8: Estimation of PCSs for Ile residues based on the preliminary X-ray crystal structure coordinates.

4 Role of Highly Dynamic Residues in the High Molecular Weight Aggregates of the Membrane Binding Heme Protein Nitrophorin 7: A solid-state NMR study

When compared to other nitrophorins (NP1-4), NP7 was found to bind to l-α-phosphatidyl-l-serine (PS) containing phospholipid membranes which were not observed in the case of other nitrophorins (NP1–4) . However atomistic details of the membrane binding events and the relevant structural changes responsible for the membrane binding were not well understood. In this regard, ssNMR is an ideal tool to understand the structural changes of NP7 upon liposome binding, since it can provide atomic-resolution structural details under near physiological conditions without the need for crystals or soluble proteins. In this chapter, we report a comparative study of the liposome bound and unbound NP7 aggregates using high resolution ssNMR spectroscopy.

4.1 Absence of dynamic residues in liposome bound NP7

Fig. 4.1 shows the temperature dependent one-dimensional ^{13}C spectra of liposome bound U[^{13}C,^{15}N\(K,V)]NP7-NO recorded using CP (black) and refocused INEPT[75] (red) based methods with and without MAS. In the case of NP7 aggregates, at a nominal temperature of 10°C, the spectra are characterized by the presence of both rigid and flexible residues. However, under the same experimental conditions, the spectra from the liposome bound form of NP7 are characterized only by the presence of CP signals (fig. 4.1). The sharp INEPT signals around 65 and 75 ppm originate from glycerol and the peak at around 4 ppm originates from the rotor spacer. The peak appearing around 4 ppm, originating from the material of the rotor spacer was further confirmed by recording the spectrum under the same conditions with an empty rotor.

A further decrease in temperature from 10°C to -10°C did not show significant influence in signal intensities for both sample states for CP and INEPT based methods. However, in the case of NP7 aggregates, the CP spectra recorded at -30°C showed intense CP signals (4-fold) in the absence and presence of MAS within the temperature regime of -10°C to -30°C. The INEPT spectra of NP7 aggregates recorded at -30°C were devoid of any signals from the protein indicating the absence of any dynamic residues at this temperature. The absence of dynamic residues in the liposome bound NP7 could give a preliminary hint that the dynamic residues observed in the NP7 aggregates might have significant influence in membrane binding. MAS at 11 kHz improved the spectral resolution significantly for both CPMAS and INEPTMAS, as anisotropic interactions were efficiently averaged to yield well resolved resonance lines.

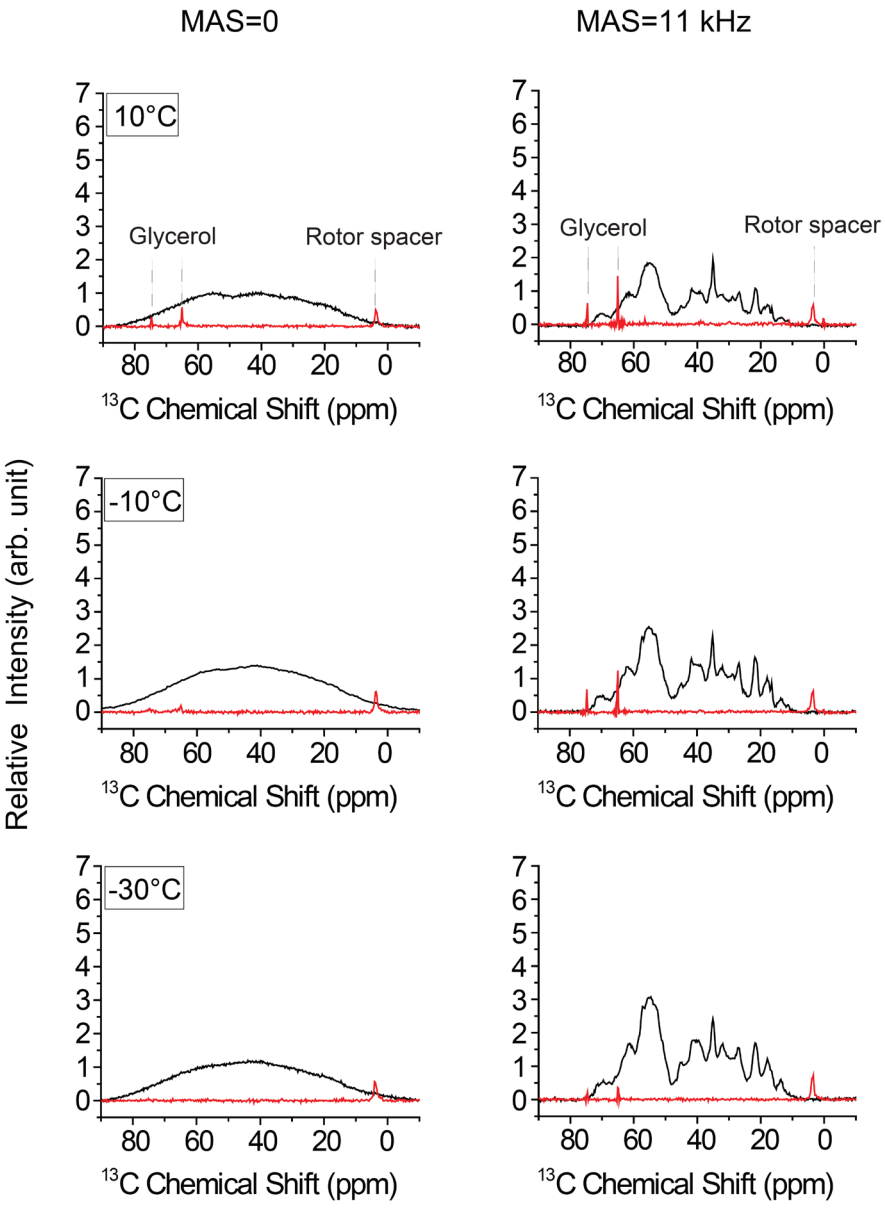

Fig. 4.1: Temperature dependent 1D ^{13}C spectra of liposome bound U[^{13}C,^{15}N\(K,V)]NP7-NO recorded using CP (black) and INEPT (red) based methods with and without MAS. All the spectra were recorded at a ^{1}H Larmor frequency of 600 MHz and temperature was decreased from 10°C down to -30°C. For the INEPT based experiments, ^{1}H-^{13}C dephasing delay was set to 1.725 ms. All the spectra were processed with 10 Hz of line broadening.

4.2 Temperature dependent cross polarization transfer efficiency

When compared to the liposome bound NP7, in the case of NP7 aggregates, a 4-fold increase in CP signal intensity from the backbone C_α atoms could be observed with respect to decrease in temperature (fig. 3.7, Chapter 3). To further investigate the temperature dependent dynamics of NP7 aggregates and the liposome bound NP7, ^{1}H-^{13}C cross-polarization build-up experiments were conducted at 11 kHz MAS (fig. 4.2). The temperature was decreased from 10°C to -30°C in steps of 10°C, and ^{1}H to ^{13}C CP build up curves were monitored and compared for the NP7 aggregates and the liposome bound NP7. The Hartmann-Hahn cross polarization conditions were optimized (n=1 condition) for respective temperatures, and ^{1}H to ^{13}C contact times were incremented from 0 to 2 ms in steps of 20 μs. A comparison between liposome bound NP7 and the aggregates revealed similar buildup rates. For each temperature, an optimal H_α-C_α transfer was observed around 80 μs for both sample states. This behavior is expected for rigid solids indicating that NP7 aggregates undergo restricted rotational diffusion similar to that of liposome bound NP7. Liposome bound state of NP7 did not show any dramatic increase in ^{1}H to ^{13}C polarization transfer with decrease in temperature. However in the case of NP7 aggregates, a 4-fold increase in ^{1}H to^{13}C polarization transfer can be observed at -30°C. This effect is significant below -10°C and could be potentially ascribed to the quenching of local dynamics and thereby contributing to the CPMAS spectra. This also stems from the fact that, the resonance frequency of the signals observed in the INEPT-TOBSY spectra were completely different to those found in the CPMAS spectra. This indicates that at higher temperatures, NP7 aggregates are characterized by the presence of highly dynamic residues which were found to be completely absent in the liposome bound NP7 further validating that these dynamic residues might have significant influence in liposome binding.

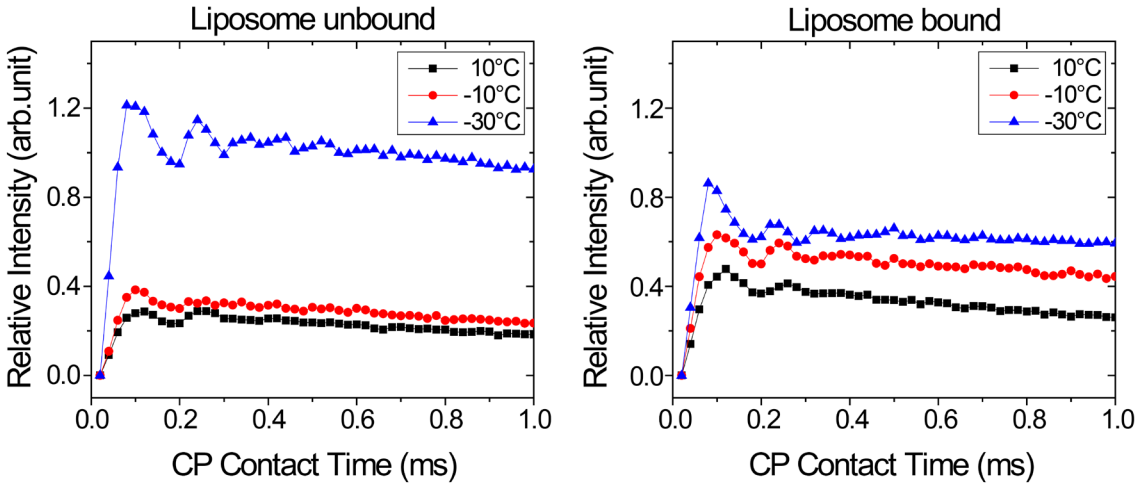

Fig. 4.2: ^{1}H to $^{13}C_{\alpha}$ cross polarization magic angle spinning (CPMAS) build up curves for the liposome unbound aggregates (left) and the liposome bound state (right) of U[^{13}C,^{15}N\(K,V)]NP7-NO. The Hartmann-Hahn conditions were matched to the n=1 conditions at 11 kHz MAS. The ^{1}H to ^{13}C contact time was increased from 0 to 2.0 ms in steps of 20 µs.

4.3 Induced conformational changes upon liposome binding

1D ^{13}C spectra of liposome bound NP7 and the aggregates recorded under identical experimental conditions were almost identical (fig. 4.3). The presence of sharp peak around 35 ppm in the liposome bound NP7 originates from the lipid head groups, which was further confirmed by recording a spectrum of liposomes in the absence of NP7. Previous reports on NP-liposome interaction studies have revealed that all net-negatively charged liposomes were aggregated by NP7, whereas the neutral ones were not[24]. Even though any biological significances of liposome aggregation were not reported, connecting ('gluing') properties of NP7 with liposomes was postulated by the possible existence of a second site of interaction with liposomes[24]. This hypothesis was further supported by the previously reported biphasic binding kinetics toward PC:PS (3:1) monolayers showing low K_d values of 4.8 and 755 × 10^{-9} M[23].

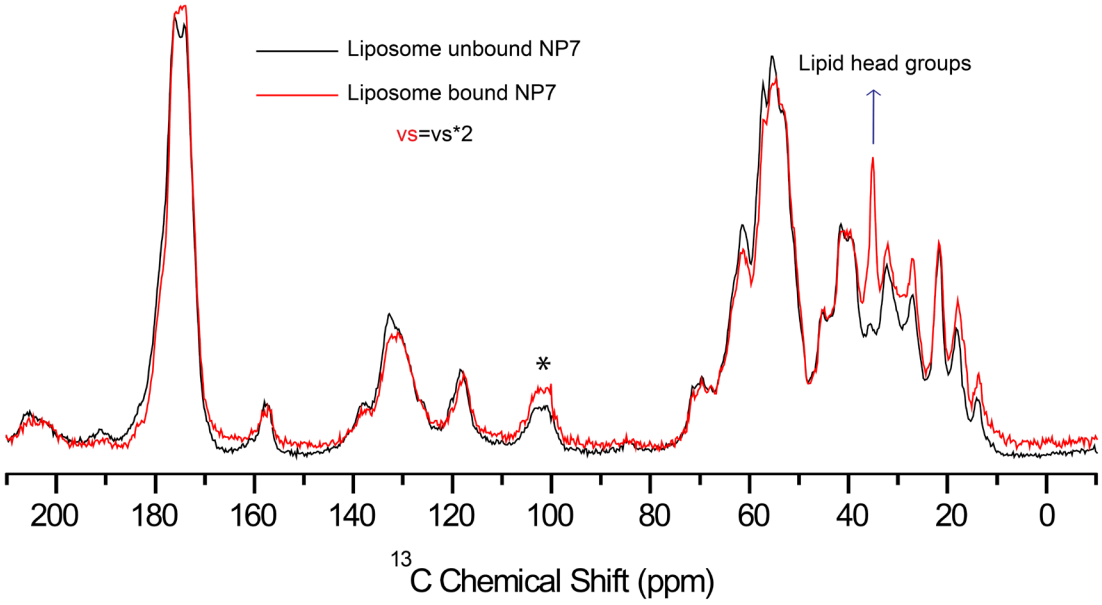

Fig. 4.3: 1D ^{13}C spectra from the liposome bound (red) and liposome unbound aggregates (black) of U[^{13}C,^{15}N\(K,V)]NP7-NO. Data were processed with 10 Hz of line broadening and were fit to the same height. The presence of lipid head groups around ~35 ppm in the liposome bound NP7 is represented by a blue arrow. First order carbonyl spinning side bands are shown by asterisks.

To gain further insights from the 1D ^{13}C spectra, a comparison was made between the 2D ^{13}C-^{13}C PDSD[60] (*p*roton *d*riven *s*pin *d*iffusion) correlation spectra between the liposome bound and unbound NP7 (fig. 4.4). A comparison between the two spectra obtained under identical conditions was almost identical, indicating that the overall NP7 structure is basically the same in both preparations. However, chemical shift perturbations could be observed for certain residues in the liposome bound NP7 spectrum probably due to induced conformational changes upon liposome binding. It is worth noting that the liposome bound NP7 was devoid of any INEPT signals from the protein while the liposome unbound NP7 showed highly dynamic residues. The presence of highly dynamic residues in the NP7 aggregates and the absence of these residues in the liposome bound state could indicate that these dynamic residues could be responsible for liposome binding.

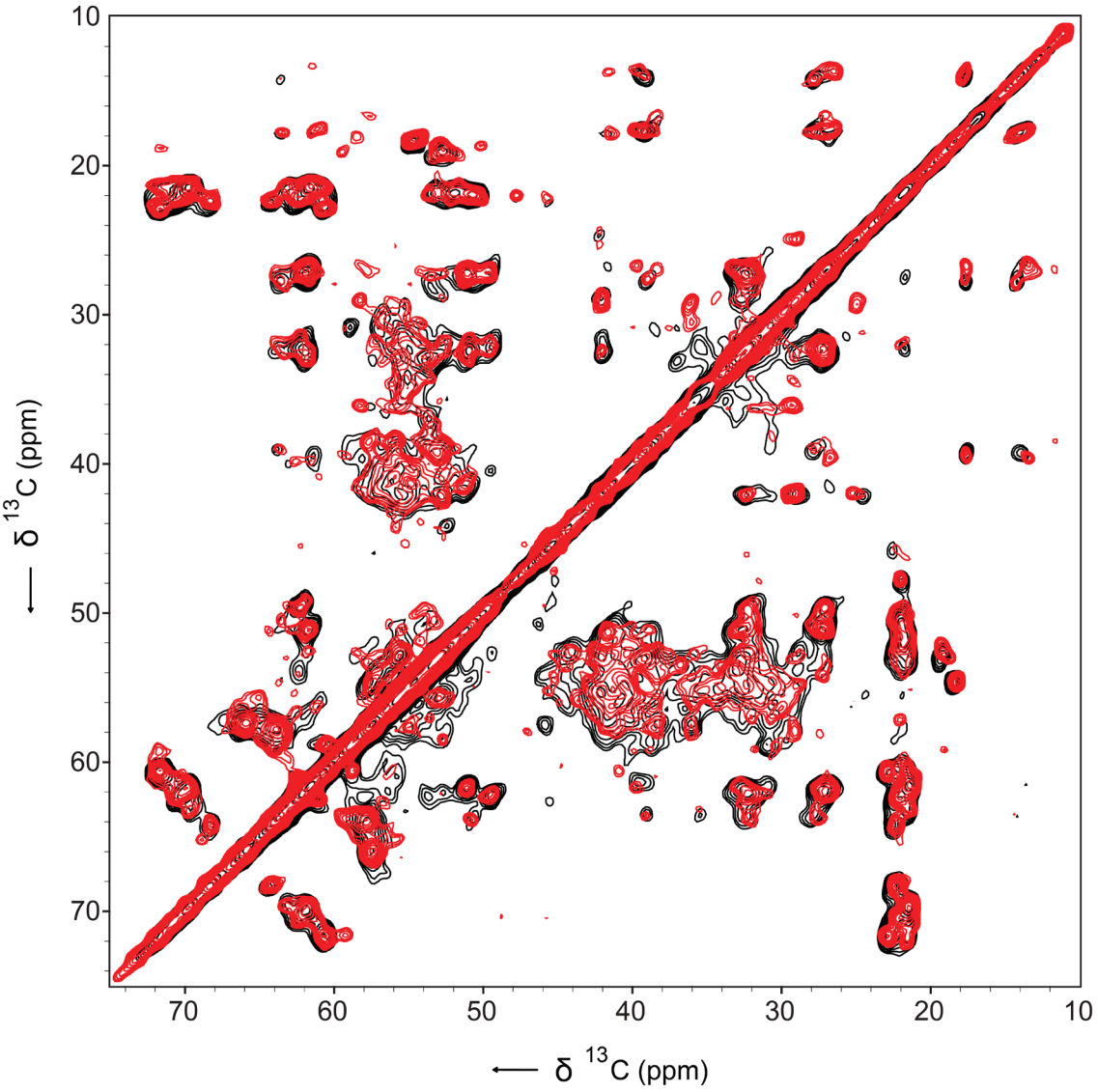

Fig. 4.4: Overlay of the aliphatic regions of the 2D ^{13}C-^{13}C PDSD spectra of U[^{13}C,^{15}N\(K,V)] NP7-NO in the liposome bound (red) and the aggregates (black). Both the spectra were recorded at a ^{1}H Larmor frequency of 600 MHz (14.1 T) at 11 kHz MAS and at -30°C. Both the data were processed with combination of an exponential and a Gaussian function (-150 Hz exponential, Gaussian factor 0.2).

4.4 Role of dynamic residues in liposome binding

To check whether the dynamic residues have any significant influence in liposome binding, a comparison was made between the 2D ^{13}C-^{13}C INEPT-TOBSY (*i*nsensitive *n*uclei *e*nhanced *p*olarization *t*ransfer-*t*hrough *b*ond correlation *s*pectroscop*y*)[69,71,76] spectrum with the 2D ^{13}C-^{13}C PDSD spectra from the liposome bound NP7 and from the NP7 aggregates. Fig. 4.5 shows overlays of the selected aliphatic regions of the 2D ^{13}C-^{13}C INEPT-TOBSY spectrum (blue) of the NP7 aggregates with 2D ^{13}C-^{13}C PDSD spectrum from the liposome bound NP7 (red) and the liposome unbound state (black). Secondary chemical shift analysis of the identified residue types from the 2D ^{13}C-^{13}C INEPT-TOBSY spectrum are mainly characteristic of random coil conformation indicating that these residues arise from the unstructured parts of the protein (Table 4.1).

From fig. 4.5(a) it can be seen that the β-strand regions from the Ala C_α-C_β region are least effected upon liposome binding, while chemical shift perturbations could be clearly observed for Ala residues with random coil (A145) and α-helical (A154) secondary structure. For A154, chemical shift differences of 0.5 ppm for the C_α, 0.6 ppm for the C' and 0.2 ppm for the C_β carbon atoms could be observed between the liposome bound and the unbound state. In the case of A145, chemical shift differences of -0.6 ppm for the C_α and 0.5 ppm for C' carbon atoms could be observed.

A comparison between the Arg side chain C_δ-C_β and C_δ-C_γ cross peak region show chemical shift differences mainly for Arg141 residue (fig. 4.5c). These regions are also characterized by the presence of C_β-C_γ and C_β-C_δ crosspeaks from Leu residues and are labelled in green. Since the biosynthesis of Leu involves Val as a precursor, thus resulting in deficient labelling of Leu, the observed cross peaks from the Leu side chains could be ascribed to isotropic scrambling[125,165]. Among the two Arg residues in the whole NP7 sequence, R141 which is found to be in the loop region between β-strand H and the α-helix showed chemical shift differences of 0.7 ppm for the C_γ and -0.25 ppm for the C_δ between the liposome bound and the unbound state.

However, no significant chemical shift changes were observed for the C_γ and C_δ resonances for R48 which is located in the β-strand B.

Similarly, chemical shift differences for proline with random coil chemical shifts could also be observed upon liposome binding, while proline from the β-strand regions did not show any significant changes (fig. 4.5d and 4.5e). For P147, chemical shift differences of 0.4 ppm for the C_α, -0.2 ppm for the C_β, -0.3 ppm for the C_γ and 0.3 ppm for the C_δ carbon atoms could be observed between the liposome bound and the unbound state. This small, but significant difference in chemical shift changes of proline residues could be ascribed to the structural rigidity of the proline ring system, when compared to the Arg residues having comparatively long and flexible side chains. Furthermore, when compared to the guanidino groups of Arg residues which can act as hydrogen bond donors with phosphorous atoms of the lipid head groups, proline cannot act as hydrogen bond donor. Since arginine is one of the most hydrophilic amino acid and are usually found near the surfaces of proteins[166], role of R141 is particularly interesting. Furthermore, five-nitrogen bonded protons are capable of forming extensive hydrogen bond network and are often found to be involved in molecular recognition sites for phosphate-containing substrates[167]. Based on the above observations it could be concluded that, β-strand regions are the least affected while dynamic loop (between β-strand H and α-helix) and the α-helix near the C-terminus have significant influence in NP7-liposome interactions.

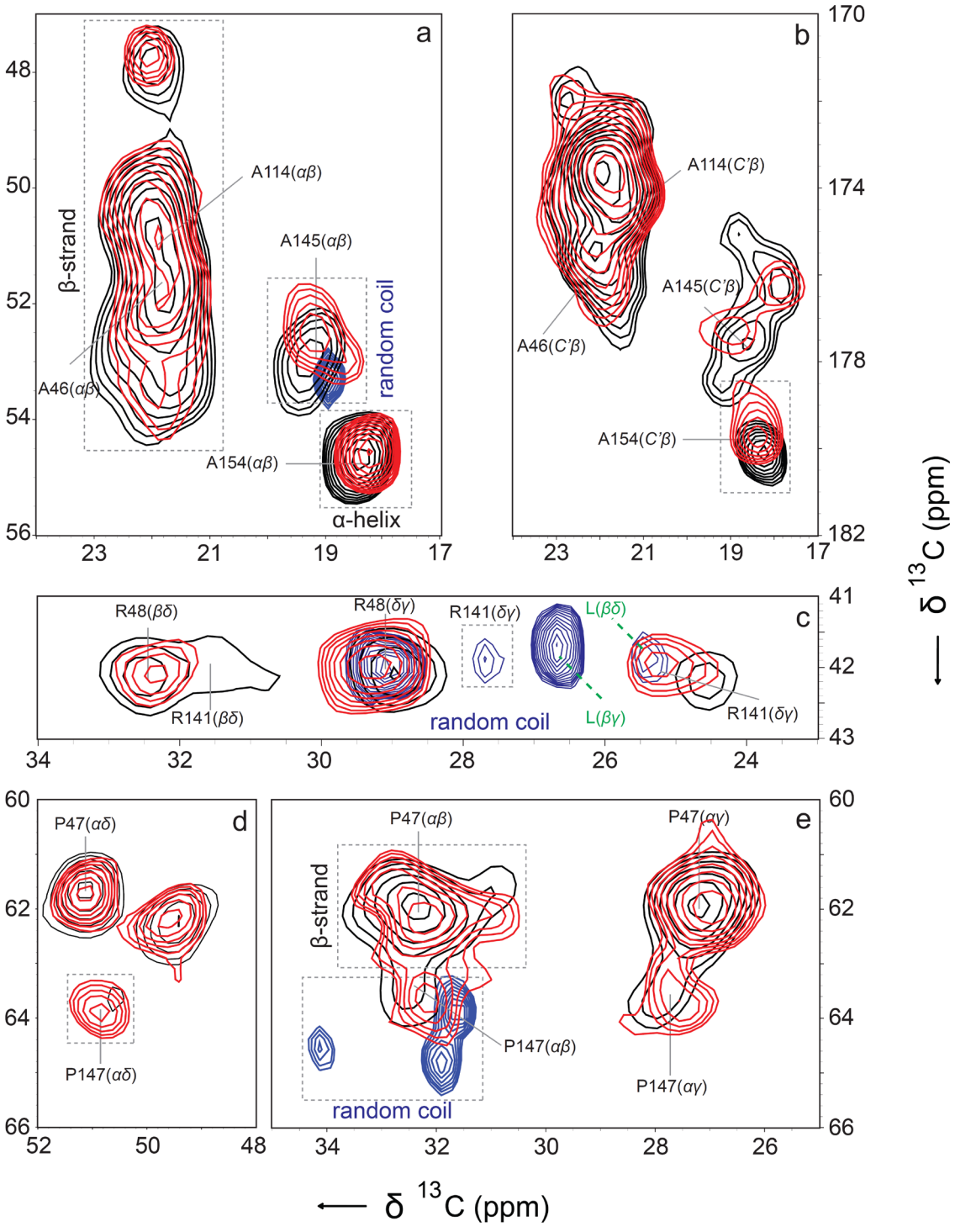

Fig. 4.5: Overlays of the aliphatic regions from the 2D ^{13}C-^{13}C INEPT-TOBSY (blue), onto 2D ^{13}C-^{13}C PDSD spectra of the liposome unbound (black) and bound state (red) of U[^{13}C,^{15}N\(K,V)]NP7-NO. Representative regions from the same spectra showing (a) Ala C_α-C_β

(b) Ala C'-C_β (c) Arg C_δ-C_γ (d) Pro C_α-C_δ and (e) Pro C_α-$C_{\beta,\gamma}$. Random coil chemical shift for the C_γ of R141 (27.6 ppm) is shown in dotted blue rectangle and the cross peaks from Leu side chains are labelled in green.

Based on a molecular model of NP7 (homology model), the interaction site for the preferential binding was found to be an α-helix comprising five Lys residues lying outside the lipocalin β-barrel structure[23]. Sedimentation assay studies with a mutant of NP7 in which Lys 179 was replaced by Ala against 3:1 PC/PS vesicles showed a substantial reduction (by a factor of 3) in liposome binding when compared to the wild-type protein[23]. Further more, NP7 interaction with liposome was reported to result in vesicle aggregation which was not observed in the case of other NPs (NP1-4)[24]. Taken together, our results are in good agreement with the previously reported studies for the preferential binding of NP7 towards phosphatidylserine containing phospholipids which was not observed for other NPs (NP1-4)[24,36].

Even though nitrophorins (NP1-4) have been structurally and functionally well studied using various biophysical methods, it is still unclear why the insect uses a cocktail of NPs in the various stages of its life[169]. Since the physiological concentration of NPs in the saliva of "kissing bug" *Rhodnius Prolixus* is several hundreds of micromolar to few millimolar[170], protein-protein interactions might play a crucial role in vivo. Even though in vivo significance of NP7 aggregates have not yet been reported, a literature search shows that oligomerization of NPs might have physiological implications in facilitating the efficient storage and release of the highly reactive NO in the insect saliva[171]. Under these circumstances, the high protein concentration in near physiological conditions (~2 mM, pH 5) used in this study seems to mimic the native system rather well.

5 Conclusions & outlook

5.1 NP7 and ssNMR

The improvement of existing protocol for the expression and purification of the heme protein NP7 in the isotopically labeled form [U-^{13}C,^{15}N\(K,V)]NP7 enabled us to record ssNMR spectra. For today's development of ssNMR spectroscopy the size of the protein (21 kDa) still resembles a challenge for full structural determination. Thus, the reverse labeling of some of the most abundant amino acid residues simplified the spectrum such that type specific and site specific assignments are possible. Furthermore, the use of the two electronic spin states $S = 0$ and $S = {}^1/_2$ of the ferriheme allows the identification of residues due to paramagnetic shifting induced through PCS and PRE which is demonstrated here for the proximal heme pocket residues Ile121 and Ile123. These techniques were proposed previously to help the assignment of residues. However, in all previous cases of reported examples of ssNMR on metalloproteins, the respective X-ray structure was available which provided the basis of the assignment. In the case of NP7, diffracting crystals are available and are published[35]; however, disorder in the structure complicates the process of structural refinement. An important outcome of the ssNMR study is the detailed investigation of the NP7 oligomerization state, which was previously reported, but the effects on the structure could not be predicted. It is clear now that at concentrations of approx. 0.1 to 2 mM oligomers are in equilibrium with monomers. Furthermore, the protein oligomerizes preferably in units of trimers, hexamers, and higher oligomeric states of unidentified composition. However, the fact that monomers are not visible in the INEPT-TOBSY spectra demonstrates that at the concentrations required for ssNMR (>2mM) oligomers form a precipitate that does not dissolve into monomers again. However, we ascribe this effect to the high concentrations of protein required for NMR spectroscopy and not to have any biological

meaning because at protein concentrations relevant in vivo the protein is mostly monomeric. In this respect, a very important result derived from ssNMR spectroscopy, which was not clear from solution NMR, is that the overall structure of the protein is not affected by the precipitation, and structure elucidation of the protein at high concentration is feasible.

We have also shown that ssNMR spectroscopy can be successfully employed to gain atomic level structural insights from high molecular weight aggregates of NP7 in the liposome bound and unbound state. The spectra obtained from the liposome bound NP7 and the aggregates are well resolved and almost identical, indicating that overall structure of NP7 is basically the same in both cases. Since the basic structures of NP7 in both sample states are almost the same, oligomerization of NP7 around the liposomes is also suspected, which is also in good agreement with the previous studies on NP7-liposomal interactions. Highly dynamic residues observed in the NP7 aggregates are not due to the overall mobility of the monomers in solution, but due to the local flexibility. The presence of highly dynamic residues in the NP7 aggregates and the systematic absence of the same in the liposome bound state indicate that these residues have significant influence in liposome binding. Well resolved resonances observed in the INEPT spectra, even in the absence of MAS indicate that anisotropic interactions are sufficiently averaged, further validating our results. Our results are in good agreement with the previously reported studies of other nitrophorins (NP1-4), where β-strand regions were found to be highly ordered in structure, while the connecting loops showed high flexibility. Based on the chemical shift perturbations observed for certain subset of residues, NP7-membrane interaction was found to be mediated by the rear end of the heme pocket. In a broader sense, NP7-liposome interaction studies could also provide atomic level insights for other membrane binding proteins and/or for proteins with a lipocalin fold.

Similar to solution-state NMR, complete site-specific assignments of the resonances is a fundamental prerequisite for 3D structural calculations. However, ssNMR studies on relatively large biomacromolecules are always complicated due to problems arising from low resolution, reduced sensitivity and spectral crowding which hamper the site-specific resonance assignments. Based on multi dimensional homonuclear ^{13}C-^{13}C and heteronuclear ^{15}N-^{13}C correlation spectra, intra-residual assignments could be accomplished for the 17 amino acid residue types. The missing three amino acid types arise from Lys, Val and Leu due to reverse labeling. Secondary chemical shift analysis of the identified resonances based on the CPMAS spectra predominantly showed β-strand character indicating that they mainly originate from the rigid β-sheet regions. Furthermore, secondary structure analysis of the site-specifically assigned resonances also showed predominantly β-strand character. The incompleteness of the sequential assignments from NP7 aggregates using ssNMR mainly stems from the following reasons.

5.2 Sequential assignments

Based on the available homology model[36] and the available crystal structure of NP7[35], it could be clearly seen that β-barrel region of the protein is made up of eight anti-parallel β-strands comprising 79 residues. These β-strand regions are connected to each other by means of unstructured loop regions and were found to be highly dynamic. Furthermore, the N-terminus and the C-terminus of NP7 were also found to be mobile, indicating that more than one half of the protein is dynamic at higher temperatures. This is further supported from the observed cross peaks from the 2D ^{13}C-^{13}C INEPT-TOBSY spectrum as they were completely different as that observed from the dipolar based CPMAS spectra.

Since in ssNMR, coherence transfer is mainly based on dipolar couplings, any dynamic process that might average out the dipolar couplings could also hamper the polarization transfer. The

situation is even worsened in the case of NCOCX spectra as the polarization transfer mainly involves a backbone $N_{(i)}$-$C'_{(i-1)}$ transfer and could suffer from low signal to noise, in addition to conformational heterogeneity caused by the dynamic residues upon freezing. The oligomerization and aggregation of NP7 is a random process resulting in a polydisperse mixture of NP7 complexes, which upon freezing in the ssNMR rotors results in a variety of conformers. Even though, this does not adversely affected spectral resolution in the 3D NCACB spectrum, poor signal to noise ratio (S/N) could be observed in the case of NCOCX spectrum, in addition to the overlapping resonances resulting in ambiguous sequential assignment possibilities.

Since the NP7 samples used in this present research work were reverse labeled for Lys and Val, the resulting spectra were found to be devoid of Lys, Val and Leu resonances. The NP7 sequence contains 27*Lys, 13*Val and 15*Leu residues, indicating that 55 residues will be systematically absent from the intra-residual assignments. Furthermore, sequential assignments from residues flanked by these residues ($(i-1)^{th}$ and $(i+1)^{th}$) could not be accomplished as the NCOCX spectra used for sequential assignments is mainly dependent on $N_{(i)}$-$C'_{(i-1)}$ magnetization transfer.

5.3 Towards complete sequential assignments

The complete sequential assignments towards structural calculations could be possible, provided the following methods are employed with respect to the sample state and pulse sequences.

5.3.1 ssNMR on NP7 crystals

Recently, crystallization conditions for NP7 which yields well defined diffractable crystals have been established[35]. In the light of this, the problems arising from structural and conformational heterogeneity could be alleviated to a greater extent by measuring ssNMR spectra from the isotopically labeled NP7 crystals or micro crystals.

5.3.2 Isotopic labeling schemes

Reverse labeling for Lys and Val resulted in masking one-third of the residues (~55 residues including Leu) and sequential information could not be achieved from other amino acids flanked by these residues. Complete sequential assignments using ssNMR is feasible using other isotopic labeling schemes such as triple labeling[172,173] or by expressing the protein using [1,3-^{13}C]glycerol or [2-^{13}C]glycerol as the carbon sources[10,174-176]. Triple labeling involves expressing the protein from *E. coli* which are grown on minimal medium supplemented with $^{15}NH_4Cl$ and ^{13}C-glucose and using D_2O instead of H_2O resulting in 70-80% deuteration of the side chains. Even though relatively expensive, higher levels of deuteration (~95%) can also be achieved by using $^{13}C,^{2}H$-glucose as the carbon source. Deuteration and back-substitution of exchangeable protons in proteins have been successfully demonstrated in ssNMR, allowing sensitive detection of protons[177-179], determination of long range ^{1}H-^{1}H distances[180-182], localizing mobile water molecules in protein structure[183] and also in probing side chain dynamics[184-187]. On the other hand, [1,3-^{13}C]- and [2-^{13}C]-glycerol labeled samples are found to have the following advantages. (1) reduced spectral overlap, (2) suppression of J-couplings resulting in resolved peaks, (3) alleviation of dipolar truncation effects. Furthermore, characteristic labeling pattern for each amino acid can also be exploited in obtaining site-specific sequential information.

5.3.3 Selective magnetization transfer schemes for sequential assignments

NCOCX spectra used for sequential assignments are mainly based on spin diffusion between the C'-C_x nuclei and magnetization transfer could not be controlled in a preferred manner resulting in spectral overlapping with increased ambiguity in sequential assignments. Even though NCOCACB spectra based on $C'_{(i)}$-$C_{\alpha(i-1)}$ DREAM transfer were also attempted, the problems arising from chemical shift anisotropy from the carbonyl carbon and C'-C_α offset effects prevented in obtaining well resolved spectra. However the C'-C_α DREAM transfer could be

circumvented by other selective mixing schemes such as SPC-5 recoupling[55] and could result in reduced spectral overlap and could provide a way to unambiguous sequential assignments.

5.3.4 Inter-residual sequential links

2D ^{13}C-^{13}C Proton driven spin diffusion (PDSD) spectra obtained from the NP7 aggregates were found to have inter-residual cross peaks at a mixing time of 100 ms. Based on the unique amino acid pairs in the sequence and based on their characteristic chemical shifts these cross peaks could be tentatively assigned. At longer mixing times, more inter-residual cross peaks could be revealed and more sequential information could be gained.

5.3.5 Identifying the dynamic residues

NP7 aggregates were found to have a subset of highly dynamic residues with reduced secondary chemical shifts as evident from the 2D ^{13}C-^{13}C INEPT-TOBSY spectra. A subset of these residues was found to have significant influence in liposome binding. Even though these regions could be identified based on certain set of observations supported by paramagnetic effects, site specific resonance assignments are still missing for these residues. Since these residues were found to be dynamic even in the absence of MAS, it would be worthwhile to check the dynamics in the absence of heteronuclear dipolar decoupling to reduce the problems arising from sample heating. In the absence of heteronuclear decoupling, it would be also challenging and rewarding to check whether longer mixing times could lead to inter-residual cross peaks for obtaining sequential information. Sequential information could also be gained from refocused INEPT based heteronuclear (^{15}N-^{13}C) correlation experiments and has been demonstrated successfully in the case of other proteins[77,188-191].

5.4 NP7-membrane interactions

Arg and Lys residues are mainly found at the surface of the proteins and are found to have significant influence in molecular recognition and membrane interactions. Furthermore, the role of Lys and Arg residues in membrane interactions and the possible formation of H-bonds between side chain nitrogen atoms and the phosphorous atoms of the lipid head groups had been extensively studied using ssNMR and MD simulations[138,192-196]. However, since the NP7 sample used in this study is reverse labeled for Lys and Val, the significance of Lys residues in membrane interaction could not be well studied. The formation of H-bonds between the Lys and Arg residues with the phosphorus atoms of the lipid head groups could be studied by ssNMR by using heteronuclear recoupling methods like REDOR and could be of immense help in understanding the depth of insertion and orientation of NP7 in the membranes.

5.5 Paramagnetic effects

Paramagnetic effects arising in the form of pseudocontact shifts (PCS) and relaxation enhancements (PRE) could be observed from the high molecular weight aggregates of NP7. Based on the preliminary X-ray structure and by the quantification of the PCSs, two Ile residues (Ile121 and 123) near the heme pocket could be identified and assigned from the NP7 aggregates. Very recently, with 3 mg of sample and a with small set of experiments, several hundred PCSs were measured and assigned, and these PCSs were subsequently used in combination with $^{1}H–^{1}H$ distance and dihedral angle restraints to determine the protein backbone geometry with high precision along with information about the active site from a large metalloprotein, Co^{2+}-substituted superoxide dismutase (Co^{2+}-SOD)[197]. In the context of isotopically labeled NP7 crystals and in the regime of very fast MAS frequencies (>30 kHz), a wealth of information could be obtained including the residues close to the heme centre.

5.6 Hybrid approach of ssNMR and solution-state NMR

ssNMR is a robust tool for gaining atomic level structural insights from complicated and challenging biomolecular systems which cannot be addressed by solution-state NMR and X-ray crystallography. However, gaining structural information from these complex systems is a challenging task and might need extensive isotopic labeling schemes. In this scenario, a hybrid approach of solution-state NMR and ssNMR could be of immense help as both could act as complementary techniques to each other. Unfortunately solution-state NMR studies on NP7 were not successful due to the irreversible precipitation of the protein in NMR sample tubes. Since NP7 has high affinity binding to membranes, aggregation effects in solution could be minimized by attaching to micelles or lipodisq[198,199]. The attachment of protein to the above mentioned membrane mimicking systems would result in the systematic absence of certain set of resonances due to the lack of dynamics indicating the residues responsible for membrane binding. On the other hand, well resolved signals could be observed from the unbound dynamic residues. The systematic absence of resonance from the bound interface of the protein from solution-state NMR could be compared with the results from ssNMR providing additional proof for membrane interaction. Furthermore, complete site-specific resonance assignments could be obtained with well established solution-state NMR pulse programs and could support the wealth of information obtained from ssNMR results.

6 References

1 Verlinde, C. L. M. J. & Hol, W. G. J. Structure-based drug design: progress, results and challenges. *Structure* **2**, 577-587, (1994).

2 Berman, H. M., Westbrook, J., Feng, Z., Gilliland, G., Bhat, T. N., Weissig, H., Shindyalov, I. N. & Bourne, P. E. The Protein Data Bank. *Nucleic Acids Research* **28**, 235-242, (2000).

3 Kay, L. E. & Gardner, K. H. Solution NMR spectroscopy beyond 25 kDa. *Current Opinion in Structural Biology* **7**, 722-731, (1997).

4 Pervushin, K., Riek, R., Wider, G. & Wüthrich, K. Attenuated T_2 relaxation by mutual cancellation of dipole–dipole coupling and chemical shift anisotropy indicates an avenue to NMR structures of very large biological macromolecules in solution. *Proceedings of the National Academy of Sciences* **94**, 12366-12371, (1997).

5 Chiti, F. & Dobson, C. M. Protein Misfolding, Functional Amyloid, and Human Disease. *Annual Review of Biochemistry* **75**, 333-366, (2006).

6 Bucciantini, M., Giannoni, E., Chiti, F., Baroni, F., Formigli, L., Zurdo, J., Taddei, N., Ramponi, G., Dobson, C. M. & Stefani, M. Inherent toxicity of aggregates implies a common mechanism for protein misfolding diseases. *Nature* **416**, 507-511, (2002).

7 Heise, H. Solid-State NMR Spectroscopy of Amyloid Proteins. *ChemBioChem* **9**, 179-189, (2008).

8 Tycko, R. Solid-state nuclear magnetic resonance techniques for structural studies of amyloid fibrils. *Nuclear Magnetic Resonance of Biological Macromolecules, Pt B* **339**, 390-413, (2001).

9 McDermott, A. Structure and Dynamics of Membrane Proteins by Magic Angle Spinning Solid-State NMR. *Annual Review of Biophysics* **38**, 385-403, (2009).

10 Castellani, F., van Rossum, B., Diehl, A., Schubert, M., Rehbein, K. & Oschkinat, H. Structure of a protein determined by solid-state magic-angle-spinning NMR spectroscopy. *Nature* **420**, 98-102, (2002).

11 Herbert-Pucheta, J.-E., Colaux, H., Bodenhausen, G. & Tekely, P. Disentangling Crystallographic Inequivalence and Crystallographic Forms of l-Arginine by One- and Two-Dimensional Solid-State NMR Spectroscopy. *The Journal of Physical Chemistry B* **115**, 15415-15421, (2011).

12 Bertini, I., Luchinat, C., Parigi, G., Ravera, E., Reif, B. & Turano, P. Solid-state NMR of proteins sedimented by ultracentrifugation. *Proceedings of the National Academy of Sciences*, (2011).

13 Zeri, A. C., Mesleh, M. F., Nevzorov, A. A. & Opella, S. J. Structure of the coat protein in fd filamentous bacteriophage particles determined by solid-state NMR spectroscopy. *Proceedings of the National Academy of Sciences* **100**, 6458-6463, (2003).

14 Straus, S., Scott, W., Schwieters, C. & Marvin, D. Consensus structure of Pf1 filamentous bacteriophage from X-ray fibre diffraction and solid-state NMR. *European Biophysics Journal* **40**, 221-234, (2011).

15 Holland, G. P., Creager, M. S., Jenkins, J. E., Lewis, R. V. & Yarger, J. L. Determining Secondary Structure in Spider Dragline Silk by Carbon−Carbon Correlation Solid -State NMR Spectroscopy. *Journal of the American Chemical Society* **130**, 9871-9877, (2008).

16 Alam, T. M. & Drobny, G. P. Solid-state NMR studies of DNA structure and dynamics. *Chemical Reviews* **91**, 1545-1590, (1991).

17 Andrew, E. R., Bradbury, A. & Eades, R. G. Nuclear Magnetic Resonance Spectra from a Crystal rotated at High Speed. *Nature* **182**, 1659-1659, (1958).

18 Lowe, I. J. Free Induction Decays of Rotating Solids. *Physical Review Letters* **2**, 285-287, (1959).

19 Pines, A., Gibby, M. G. & Waugh, J. S. Proton-enhanced NMR of dilute spins in solids. *The Journal of Chemical Physics* **59**, 569-590, (1973).

20 Knipp, M. & He, C. Nitrophorins: Nitrite disproportionation reaction and other novel functionalities of insect heme-based nitric oxide transport proteins. *IUBMB Life* **63**, 304-312, (2012).

21 Champagne, D. E., Nussenzveig, R. H. & Ribeiro, J. M. C. Purification, Partial Characterization, and Cloning of Nitric Oxide-carrying Heme Proteins (Nitrophorins) from Salivary Glands of the Blood-sucking Insect Rhodnius prolixus. *Journal of Biological Chemistry* **270**, 8691-8695, (1995).

22 Ribeiro, J. M. C., Andersen, J., Silva-Neto, M. A. C., Pham, V. M., Garfield, M. K. & Valenzuela, J. G. Exploring the sialome of the blood-sucking bug Rhodnius prolixus. *Insect Biochemistry and Molecular Biology* **34**, 61-79, (2004).

23 Andersen, J. F., Gudderra, N. P., Francischetti, I. M. B., Valenzuela, J. G. & Ribeiro, J. M. C. Recognition of Anionic Phospholipid Membranes by an Antihemostatic Protein from a Blood-Feeding Insect. *Biochemistry* **43**, 6987-6994, (2004).

24 Knipp, M., Zhang, H., Berry, R. E. & Walker, F. A. Overexpression in Escherichia coli and functional reconstitution of the liposome binding ferriheme protein nitrophorin 7 from the bloodsucking bug Rhodnius prolixus. *Protein Expr. Purif.* **54**, 183-191, (2007).

25 Ann Walker, F. & Montfort, W. R. in *Advances in Inorganic Chemistry* Vol. Volume 51 295-358 (Academic Press, 2000).

26 Andersen, J. F., Weichsel, A., Balfour, C. A., Champagne, D. E. & Montfort, W. R. The crystal structure of nitrophorin 4 at 1.5 å resolution: transport of nitric oxide by a lipocalin-based heme protein. *Structure* **6**, 1315-1327, (1998).

27 Flower, D. R. Multiple molecular recognition properties of the lipocalin protein family. *Journal of Molecular Recognition* **8**, 185-195, (1995).

28 Flower, D. R., North, A. C. T. & Sansom, C. E. The lipocalin protein family: structural and sequence overview. *Biochimica et Biophysica Acta (BBA) - Protein Structure and Molecular Enzymology* **1482**, 9-24, (2000).

29 Ignarro, L. J. Biosynthesis and Metabolism of Endothelium-Derived Nitric Oxide. *Annual Review of Pharmacology and Toxicology* **30**, 535-560, (1990).

30 Kondrashov, D. A., Roberts, S. A., Weichsel, A. & Montfort, W. R. Protein Functional Cycle Viewed at Atomic Resolution: Conformational Change and Mobility in Nitrophorin 4 as a Function of pH and NO Binding. *Biochemistry* **43**, 13637-13647, (2004).

31 Amoia, A. M. & Montfort, W. R. Apo-nitrophorin 4 at atomic resolution. *Protein Science* **16**, 2076-2081, (2007).

32 Ribeiro, J. M. & Walker, F. A. High affinity histamine-binding and antihistaminic activity of the salivary nitric oxide-carrying heme protein (nitrophorin) of Rhodnius prolixus. *The Journal of Experimental Medicine* **180**, 2251-2257, (1994).

33 Lehane, M. J. *The biology of blood-sucking in insects*. (Cambridge Univ Pr, 2005).

34 Knipp, M., Soares, R. P. & Pereira, M. H. Identification of the native N-terminus of the membrane attaching ferriheme protein nitrophorin 7 from Rhodnius prolixus. *Anal. Biochem.* **424**, 79-81, (2012).

35 Ogata, H. & Knipp, M. Crystallization and preliminary X-ray crystallographic analysis of the membrane-binding haemprotein nitrophorin 7 from Rhodnius prolixus. *Acta Crystallographica Section F* **68**, 37-40, (2012).

36 Knipp, M., Yang, F., Berry, R. E., Zhang, H., Shokhirev, M. N. & Walker, F. A. Spectroscopic and Functional Characterization of Nitrophorin 7 from the Blood-Feeding Insect Rhodnius prolixus Reveals an Important Role of Its Isoform-Specific N-Terminus for Proper Protein Function. *Biochemistry* **46**, 13254-13268, (2007).

37 Yang, F., Zhang, H. & Knipp, M. A One-Residue Switch Reverses the Orientation of a Heme b Cofactor. Investigations of the Ferriheme NO Transporters Nitrophorin 2 and 7 from the Blood-Feeding Insect Rhodnius prolixus. *Biochemistry* **48**, 235-241, (2008).

38 Rabi, I. I., Zacharias, J. R., Millman, S. & Kusch, P. A New Method of Measuring Nuclear Magnetic Moment. *Physical Review* **53**, 318-318, (1938).

39 Purcell, E. M., Torrey, H. C. & Pound, R. V. Resonance Absorption by Nuclear Magnetic Moments in a Solid. *Physical Review* **69**, 37-38, (1946).

40 Bloch, F. Nuclear Induction. *Physical Review* **70**, 460-474, (1946).

41 Zeeman., P. The effect of magnetisation on the nature of light emitted by a substance. *Nature* **55**, 347, (1897).

42 Keeler, J. *Understanding NMR Spectroscopy*. (Wiley, Chichester, 2011).

43 Levitt, M. H. *Spin dynamics : basics of nuclear magnetic resonance*. (Wiley, 2001).

44 Duer, M. J. *Solid-state NMR spectroscopy : principles and applications*. (Blackwell Science, 2002).

45 Mason, J. Conventions for the reporting of nuclear magnetic shielding (or shift) tensors suggested by participants in the NATO ARW on NMR shielding constants at the University of Maryland, College Park, July 1992. *Solid State Nuclear Magnetic Resonance* **2**, 285-288, (1993).

46 Bak, M., Rasmussen, J. T. & Nielsen, N. C. SIMPSON: A General Simulation Program for Solid-State NMR Spectroscopy. *Journal of Magnetic Resonance* **147**, 296-330, (2000).

47 Pake, G. E. Nuclear Resonance Absorption in Hydrated Crystals: Fine Structure of the Proton Line. *The Journal of Chemical Physics* **16**, 327-336, (1948).

48 Stejskal, E. O., Schaefer, J. & Waugh, J. S. Magic-angle spinning and polarization transfer in proton-enhanced NMR. *Journal of Magnetic Resonance* **28**, 105-112, (1977).

49 Hartmann, S. R. & Hahn, E. L. Nuclear Double Resonance in the Rotating Frame. *Phys. Rev.* **128**, 2042-2053, (1962).

50 Kolodziejski, W. & Klinowski, J. Kinetics of Cross-Polarization in Solid-State NMR: A Guide for Chemists. *Chemical Reviews* **102**, 613-628, (2002).

51 Bennett, A. E., Rienstra, C. M., Auger, M., Lakshmi, K. V. & Griffin, R. G. Heteronuclear decoupling in rotating solids. *The Journal of Chemical Physics* **103**, 6951-6958, (1995).

52 Fung, B. M., Khitrin, A. K. & Ermolaev, K. An Improved Broadband Decoupling Sequence for Liquid Crystals and Solids. *Journal of Magnetic Resonance* **142**, 97-101, (2000).

53 Andrew, E. R., Bradbury, A., Eades, R. G. & Wynn, V. T. Nuclear cross-relaxation induced by specimen rotation. *Physics Letters* **4**, 99-100, (1963).

54 Raleigh, D. P., Levitt, M. H. & Griffin, R. G. Rotational resonance in solid state NMR. *Chemical Physics Letters* **146**, 71-76, (1988).

55 Hohwy, M., Rienstra, C. M., Jaroniec, C. P. & Griffin, R. G. Fivefold symmetric homonuclear dipolar recoupling in rotating solids: Application to double quantum spectroscopy. *The Journal of Chemical Physics* **110**, 7983-7992, (1999).

56 Verel, R., Baldus, M., Ernst, M. & Meier, B. H. A homonuclear spin-pair filter for solid-state NMR based on adiabatic-passage techniques. *Chemical Physics Letters* **287**, 421-428, (1998).

57 Verel, R., Ernst, M. & Meier, B. H. Adiabatic Dipolar Recoupling in Solid-State NMR: The DREAM Scheme. *Journal of Magnetic Resonance* **150**, 81-99, (2001).

58 Nielsen, N. C., Bildsoe, H., Jakobsen, H. J. & Levitt, M. H. Double-quantum homonuclear rotary resonance: Efficient dipolar recovery in magic-angle spinning nuclear magnetic resonance. *The Journal of Chemical Physics* **101**, 1805-1812, (1994).

59 Gullion, T. Rotational-echo double-resonance NMR. *Journal of magnetic resonance. Series A* **81**, 196-200, (1989).

60 Bloembergen, N. On the interaction of nuclear spins in a crystalline lattice. *Physica* **15**, 386-426, (1949).

61 Suter, D. & Ernst, R. R. Spectral spin diffusion in the presence of an extraneous dipolar reservoir. *Physical Review B* **25**, 6038-6041, (1982).

62 Suter, D. & Ernst, R. R. Spin diffusion in resolved solid-state NMR spectra. *Physical Review B* **32**, 5608-5627, (1985).

63 Grommek, A., Meier, B. H. & Ernst, M. Distance information from proton-driven spin diffusion under MAS. *Chemical Physics Letters* **427**, 404-409, (2006).

64 Takegoshi, K., Nakamura, S. & Terao, T. 13C–1H dipolar-assisted rotational resonance in magic-angle spinning NMR. *Chemical Physics Letters* **344**, 631-637, (2001).

65 Takegoshi, K., Nakamura, S. & Terao, T. ^{13}C-^{1}H dipolar-driven ^{13}C-^{13}C recoupling without ^{13}C rf irradiation in nuclear magnetic resonance of rotating solids. *The Journal of Chemical Physics* **118**, 2325-2341, (2003).

66 Hohwy, M., Rienstra, C. M. & Griffin, R. G. Band-selective homonuclear dipolar recoupling in rotating solids. *The Journal of Chemical Physics* **117**, 4973-4987, (2002).

67 Brinkmann, A. & Levitt, M. H. Symmetry principles in the nuclear magnetic resonance of spinning solids: Heteronuclear recoupling by generalized Hartmann-Hahn sequences. *The Journal of Chemical Physics* **115**, 357-384, (2001).

68 Shaka, A. J., Keeler, J. & Freeman, R. Evaluation of a new broadband decoupling sequence: WALTZ-16. *Journal of Magnetic Resonance* **53**, 313-340, (1983).

69 Baldus, M. & Meier, B. H. Total Correlation Spectroscopy in the Solid State. The Use of Scalar Couplings to Determine the Through-Bond Connectivity. *J. Magn. Reson. A* **121**, 65-69, (1996).

70 Baldus, M., Iuliucci, R. J. & Meier, B. H. Probing Through-Bond Connectivities and Through-Space Distances in Solids by Magic-Angle-Spinning Nuclear Magnetic Resonance. *J. Am. Chem. Soc.* **119**, 1121-1124, (1997).

71 Hardy, E. H., Verel, R. & Meier, B. H. Fast MAS Total Through-Bond Correlation Spectroscopy. *Journal of Magnetic Resonance* **148**, 459-464, (2001).

72 Heindrichs, A. S. D., Geen, H., Giordani, C. & Titman, J. J. Improved scalar shift correlation NMR spectroscopy in solids. *Chemical Physics Letters* **335**, 89-96, (2001).

73 Chan, J. C. C. & Brunklaus, G. R sequences for the scalar-coupling mediated homonuclear correlation spectroscopy under fast magic-angle spinning. *Chemical Physics Letters* **349**, 104-112, (2001).

74 Hardy, E. H., Detken, A. & Meier, B. H. Fast-MAS total through-bond correlation spectroscopy using adiabatic pulses. *Journal of Magnetic Resonance* **165**, 208-218, (2003).

75 Morris, G. A. & Freeman, R. Enhancement of nuclear magnetic resonance signals by polarization transfer. *J. Am. Chem. Soc.* **101**, 760-762, (1979).

76 Andronesi, O. C., Becker, S., Seidel, K., Heise, H., Young, H. S. & Baldus, M. Determination of Membrane Protein Structure and Dynamics by Magic-Angle-Spinning Solid-State NMR Spectroscopy. *J. Am. Chem. Soc.* **127**, 12965-12974, (2005).

77 Siemer, A. B., Arnold, A. A., Ritter, C., Westfeld, T., Ernst, M., Riek, R. & Meier, B. H. Observation of Highly Flexible Residues in Amyloid Fibrils of the HET-s Prion. *J. Am. Chem. Soc.* **128**, 13224-13228, (2006).

78 Wishart, D. S., Sykes, B. D. & Richards, F. M. Relationship between nuclear magnetic resonance chemical shift and protein secondary structure. *Journal of Molecular Biology* **222**, 311-333, (1991).

79 Luca, S., Filippov, D. V., van Boom, J. H., Oschkinat, H., de Groot, H. J. M. & Baldus, M. Secondary chemical shifts in immobilized peptides and proteins: A qualitative basis for structure refinement under Magic Angle Spinning. *Journal of Biomolecular NMR* **20**, 325-331, (2001).

80 Markley, J., Ulrich, E., Berman, H., Henrick, K., Nakamura, H. & Akutsu, H. BioMagResBank (BMRB) as a partner in the Worldwide Protein Data Bank (wwPDB): new policies affecting biomolecular NMR depositions. *Journal of Biomolecular NMR* **40**, 153-155, (2008).

81 Zhang, H., Neal, S. & Wishart, D. S. RefDB: A database of uniformly referenced protein chemical shifts. *Journal of Biomolecular NMR* **25**, 173-195, (2003).

82 Nilges, M., Malliavin, T. & Bardiaux, B. in *Encyclopedia of Magnetic Resonance* (John Wiley & Sons, Ltd, 2007).

83 Manolikas, T., Herrmann, T. & Meier, B. H. Protein Structure Determination from 13C Spin-Diffusion Solid-State NMR Spectroscopy. *Journal of the American Chemical Society* **130**, 3959-3966, (2008).

84 Loquet, A., Bardiaux, B., Gardiennet, C., Blanchet, C., Baldus, M., Nilges, M., Malliavin, T. & Böckmann, A. 3D Structure Determination of the Crh Protein from Highly Ambiguous Solid-State NMR Restraints. *Journal of the American Chemical Society* **130**, 3579-3589, (2008).

85 Bertini, I., Luchinat, C. & Parigi, G. *Solution NMR of Paramagnetic Molecules*. (Elsevier, 2001).

86 Bertini, I., Luchinat, C., Parigi, G. & Pierattelli, R. NMR Spectroscopy of Paramagnetic Metalloproteins. *Chembiochem* **6**, 1536-1549, (2005).

87 Jaroniec, C. P. Solid-state nuclear magnetic resonance structural studies of proteins using paramagnetic probes. *Solid State Nucl Magn Reson* **43-44**, 1-13, (2012).

88 Bertini, I., Luchinat, C. & Parigi, G. (Elsevier Science Ltd., 2001).

89 Fermi, E. Über die magnetischen Momente der Atomkerne. *Zeitschrift für Physik A Hadrons and Nuclei* **60**, 320-333, (1930).

90 McConnell, H. M. & Robertson, R. E. Isotropic Nuclear Resonance Shifts. *The Journal of Chemical Physics* **29**, 1361-1365, (1958).

91 Solomon, I. Relaxation Processes in a System of Two Spins. *Physical Review* **99**, 559-565, (1955).

92 Clore, G. M. & Iwahara, J. Theory, Practice, and Applications of Paramagnetic Relaxation Enhancement for the Characterization of Transient Low-Population States of Biological Macromolecules and Their Complexes. *Chem. Rev.* **109**, 4108-4139, (2009).

93 in *Current Methods in Inorganic Chemistry* Vol. Volume 2 (eds Claudio Luchinot Ivono Bertini & Parigi Giacomo) 29-73 (Elsevier, 2001).

94 Kurland, R. J. & McGarvey, B. R. Isotropic NMR shifts in transition metal complexes: The calculation of the fermi contact and pseudocontact terms. *Journal of Magnetic Resonance (1969)* **2**, 286-301, (1970).

95 Gueron, M. Nuclear relaxation in macromolecules by paramagnetic ions: a novel mechanism. *Journal of Magnetic Resonance (1969)* **19**, 58-66, (1975).

96 Kervern, G., Steuernagel, S., Engelke, F., Pintacuda, G. & Emsley, L. Absence of Curie Relaxation in Paramagnetic Solids Yields Long ^{1}H Coherence Lifetimes. *Journal of the American Chemical Society* **129**, 14118-14119, (2007).

97 Bloembergen, N. Proton Relaxation Times in Paramagnetic Solutions. *The Journal of Chemical Physics* **27**, 572-573, (1957).

98 Bloembergen, N. & Morgan, L. O. Proton Relaxation Times in Paramagnetic Solutions. Effects of Electron Spin Relaxation. *The Journal of Chemical Physics* **34**, 842-850, (1961).

99 Nadaud, P. S., Helmus, J. J., Kall, S. L. & Jaroniec, C. P. Paramagnetic Ions Enable Tuning of Nuclear Relaxation Rates and Provide Long-Range Structural Restraints in Solid-State NMR of Proteins. *J. Am. Chem. Soc.* **131**, 8108-8120, (2009).

100 Yang, F., Knipp, M., Shokhireva, T., Berry, R., Zhang, H. & Walker, F. ^{1}H and ^{13}C NMR spectroscopic studies of the ferriheme resonances of three low-spin complexes of wild-type nitrophorin 2 and nitrophorin 2(V24E) as a function of pH. *J. Biol. Inorg. Chem.* **14**, 1077-1095, (2009).

101 Shokhireva, T. & Walker, F. Assignment of ferriheme resonances for high- and low-spin forms of nitrophorin 3 by ^{1}H and ^{13}C NMR spectroscopy and comparison to nitrophorin 2: Heme pocket structural similarities and differences. *J. Biol. Inorg. Chem.* **17**, 911-926, (2012).

102 Shokhireva, T. K., Berry, R. E., Uno, E., Balfour, C. A., Zhang, H. & Walker, F. A. Electrochemical and NMR spectroscopic studies of distal pocket mutants of nitrophorin 2: Stability, structure, and dynamics of axial ligand complexes. *Proc. Natl. Acad. Sci. U.S.A.* **100**, 3778-3783, (2003).

103 Shokhireva, T. K., Weichsel, A., Smith, K. M., Berry, R. E., Shokhirev, N. V., Balfour, C. A., Zhang, H., Montfort, W. R. & Walker, F. A. Assignment of the Ferriheme Resonances of the Low-Spin Complexes of Nitrophorins 1 and 4 by ^{1}H and ^{13}C NMR Spectroscopy: Comparison to Structural Data Obtained from X-ray Crystallography. *Inorganic Chemistry* **46**, 2041-2056, (2007).

104 Shokhireva, T. K., Shokhirev, N. V. & Walker, F. A. Assignment of Heme Resonances and Determination of the Electronic Structures of High- and Low-Spin Nitrophorin 2 by ^{1}H and ^{13}C NMR Spectroscopy: An Explanation of the Order of Heme Methyl Resonances in High-Spin Ferriheme Proteins. *Biochemistry* **42**, 679-693, (2002).

105 Marassi, F. M., Ramamoorthy, A. & Opella, S. J. Complete resolution of the solid-state NMR spectrum of a uniformly ^{15}N-labeled membrane protein in phospholipid bilayers. *Proc. Natl. Acad. Sci. U.S.A.* **94**, 8551-8556, (1997).

106 McIntosh, L. P. & Dahlquist, F. W. Biosynthetic Incorporation of ^{15}N and ^{13}C for Assignment and Interpretation of Nuclear Magnetic Resonance Spectra of Proteins. *Quarterly Reviews of Biophysics* **23**, 1-38, (1990).

107 Heise, H., Hoyer, W., Becker, S., Andronesi, O. C., Riedel, D. & Baldus, M. Molecular-level secondary structure, polymorphism, and dynamics of full-length α-synuclein fibrils studied by solid-state NMR. *Proceedings of the National Academy of Sciences of the United States of America* **102**, 15871-15876, (2005).

108 Schneider, R., Ader, C., Lange, A., Giller, K., Hornig, S., Pongs, O., Becker, S. & Baldus, M. Solid-State NMR Spectroscopy Applied to a Chimeric Potassium Channel in Lipid Bilayers. *Journal of the American Chemical Society* **130**, 7427-7435, (2008).

109 Brand, T., Cabrita, E. J., Morris, G. A., Günther, R., Hofmann, H.-J. & Berger, S. Residue-specific NH exchange rates studied by NMR diffusion experiments. *J. Magn. Reson.* **187**, 97-104, (2007).

110 Wu, D. H., Chen, A. D. & Johnson, C. S. An Improved Diffusion-Ordered Spectroscopy Experiment Incorporating Bipolar-Gradient Pulses. *J. Magn. Reson. A* **115**, 260-264, (1995).

111 Price, W. S. Pulsed-field gradient nuclear magnetic resonance as a tool for studying translational diffusion: Part II. Experimental aspects. *Concepts Magn Reson* **10**, 197-237, (1998).

112 Antalek, B. Using pulsed gradient spin echo NMR for chemical mixture analysis: How to obtain optimum results. *Concepts Magn Reson* **14**, 225-258, (2002).

113 Price, W. S., Elwinger, F., Vigouroux, C. & Stilbs, P. PGSE-WATERGATE, a new tool for NMR diffusion-based studies of ligand–macromolecule binding. *Magn Reson Chem* **40**, 391-395, (2002).

114 Price, W. S. Pulsed-field gradient nuclear magnetic resonance as a tool for studying translational diffusion: Part 1. Basic theory. *Concepts Magn Reson* **9**, 299-336, (1997).

115 Brand, T., Cabrita, E. J., Berger, S. & Webb, G. A. 135-143 (Springer Netherlands, 2006).

116 Delaglio, F., Grzesiek, S., Vuister, G. W., Zhu, G., Pfeifer, J. & Bax, A. NMRPIPE - A MULTIDIMENSIONAL SPECTRAL PROCESSING SYSTEM BASED ON UNIX PIPES. *J. Biomol. NMR* **6**, 277-293, (1995).

117 Morcombe, C. R. & Zilm, K. W. Chemical shift referencing in MAS solid state NMR. *Journal of Magnetic Resonance* **162**, 479-486, (2003).

118 Heise, H., Köhler, F. H. & Xie, X. Solid-State NMR Spectroscopy of Paramagnetic Metallocenes. *J. Magn. Reson.* **150**, 198-206, (2001).

119 Vranken, W. F., Boucher, W., Stevens, T. J., Fogh, R. H., Pajon, A., Llinas, M., Ulrich, E. L., Markley, J. L., Ionides, J. & Laue, E. D. The CCPN data model for NMR spectroscopy: Development of a software pipeline. *Proteins: Structure, Function, and Bioinformatics* **59**, 687-696, (2005).

120 Fogh, R., Ionides, J., Ulrich, E., Boucher, W., Vranken, W., Linge, J. P., Habeck, M., Rieping, W., Bhat, T. & Westbrook, J. The CCPN project: an interim report on a data model for the NMR community. *nature structural biology* **9**, 416-418, (2002).

121 Baldus, M., Petkova, A. T., Herzfeld, J. & Griffin, R. G. Cross polarization in the tilted frame: assignment and spectral simplification in heteronuclear spin systems. *Molecular Physics* **95**, 1197-1207, (1998).

122 Petkova, A. T., Baldus, M., Belenky, M., Hong, M., Griffin, R. G. & Herzfeld, J. Backbone and side chain assignment strategies for multiply labeled membrane peptides and proteins in the solid state. *Journal of Magnetic Resonance* **160**, 1-12, (2003).

123 Franks, W. T., Kloepper, K., Wylie, B. & Rienstra, C. Four-dimensional heteronuclear correlation experiments for chemical shift assignment of solid proteins. *J. Biomol. NMR* **39**, 107-131, (2007).

124 Seidel, K., Lange, A., Becker, S., Hughes, C. E., Heise, H. & Baldus, M. Protein solid-state NMR resonance assignments from (^{13}C,^{13}C) correlation spectroscopy. *Physical Chemistry Chemical Physics* **6**, 5090-5093, (2004).

125 Waugh, D. S. Genetic tools for selective labeling of proteins with α-^{15}N-amino acids. *Journal of Biomolecular NMR* **8**, 184-192, (1996).

126 He, C., Ogata, H. & Knipp, M. Formation of the Complex of Nitrite with the Ferriheme b β-Barrel Proteins Nitrophorin 4 and Nitrophorin 7. *Biochemistry* **49**, 5841-5851, (2010).

127 Abbruzzetti, S., He, C., Ogata, H., Bruno, S., Viappiani, C. & Knipp, M. Heterogeneous Kinetics of the Carbon Monoxide Association and Dissociation Reaction to Nitrophorin 4 and 7 Coincide with Structural Heterogeneity of the Gate-Loop. *Journal of the American Chemical Society* **134**, 9986-9998, (2012).

128 Johnson Jr, C. S. Diffusion ordered nuclear magnetic resonance spectroscopy: principles and applications. *Prog Nucl Magn Reson Spectrosc* **34**, 203-256, (1999).

129 Jerschow, A. & Müller, N. Suppression of Convection Artifacts in Stimulated-Echo Diffusion Experiments. Double-Stimulated-Echo Experiments. *J. Magn. Reson.* **125**, 372-375, (1997).

130 Hua, Q.-x., Dementieva, I. S., Walsh, M. A., Hallenga, K., Weiss, M. A. & Joachimiak, A. A thermophilic mini-chaperonin contains a conserved polypeptide-binding surface: combined crystallographic and NMR studies of the GroEL apical domain with implications for substrate interactions. *J. Mol. Biol.* **306**, 513-525, (2001).

131 Sprangers, R. & Kay, L. E. Quantitative dynamics and binding studies of the 20S proteasome by NMR. *Nature* **445**, 618-622, (2007).

132 Sylvester, S. R. & Stevens, C. M. Stereospecificity of the reductoisomerase-catalyzed step in the pathway of biosynthesis of valine and leucine. *Biochemistry* **18**, 4529-4531, (1979).

133 Neri, D., Szyperski, T., Otting, G., Senn, H. & Wuethrich, K. Stereospecific nuclear magnetic resonance assignments of the methyl groups of valine and leucine in the DNA-binding domain of the 434 repressor by biosynthetically directed fractional carbon-13 labeling. *Biochemistry* **28**, 7510-7516, (1989).

134 Tugarinov, V. & Kay, L. E. Ile, Leu, and Val Methyl Assignments of the 723-Residue Malate Synthase G Using a New Labeling Strategy and Novel NMR Methods. *J. Am. Chem. Soc.* **125**, 13868-13878, (2003).

135 Han, B., Liu, Y., Ginzinger, S. & Wishart, D. SHIFTX2: significantly improved protein chemical shift prediction. *J. Biomol. NMR* **50**, 43-57, (2011).

136 Ulrich, E. L., Akutsu, H., Doreleijers, J. F., Harano, Y., Ioannidis, Y. E., Lin, J., Livny, M., Mading, S., Maziuk, D., Miller, Z., Nakatani, E., Schulte, C. F., Tolmie, D. E., Kent Wenger, R., Yao, H. & Markley, J. L. BioMagResBank. *Nucleic Acids Research* **36**, D402-D408, (2008).

137 Heinig, M. & Frishman, D. STRIDE: a web server for secondary structure assignment from known atomic coordinates of proteins. *Nucleic Acids Research* **32**, W500-W502, (2004).

138 Petkova, A. T., Hu, J. G., Bizounok, M., Simpson, M., Griffin, R. G. & Herzfeld, J. Arginine Activity in the Proton-Motive Photocycle of Bacteriorhodopsin: Solid-State NMR Studies of the Wild-Type and D85N Proteins. *Biochemistry* **38**, 1562-1572, (1999).

139 Ramachandran, G. N., Mazumdar, S. K., Venkatesan, K. & Lakshminarayanan, A. V. Conformation of the arginine side-group and its variations. *Journal of Molecular Biology* **15**, 232-242, (1966).

140 Sun, B. Q., Costa, P. R. & Griffin, R. G. Heteronuclear Polarization Transfer by Radiofrequency-Driven Dipolar Recoupling Under Magic-Angle Spinning. *Journal of Magnetic Resonance, Series A* **112**, 191-198, (1995).

141 Straus, S. K., Bremi, T. & Ernst, R. R. Resolution enhancement by homonuclear J decoupling in solid-state MAS NMR. *Chemical Physics Letters* **262**, 709-715, (1996).

142 Leppert, J., Ohlenschlager, O., Gorlach, M. & Ramachandran, R. Adiabatic TOBSY in rotating solids. *Journal of Biomolecular NMR* **29**, 167-173, (2004).

143 Courvoisier, E., Williams, P. A., Lim, G. K., Hughes, C. E. & Harris, K. D. M. The crystal structure of l-arginine. *Chemical Communications* **48**, 2761-2763, (2012).

144 Kanamori, K. & Roberts, J. D. A nitrogen-15 NMR study of the barriers to isomerization about guanidinium and guanidino carbon-nitrogen bonds in L-arginine. *Journal of the American Chemical Society* **105**, 4698-4701, (1983).

145 Seidel, K., Lange, A., Becker, S., Hughes, C. E., Heise, H. & Baldus, M. Protein solid-state NMR resonance assignments from (13C, 13C) correlation spectroscopy. *Physical Chemistry Chemical Physics* **6**, 5090-5093, (2004).

146 Harris, R. K., Wasylishen, R. E. & Duer, M. J. *NMR crystallography*. (John Wiley, 2010).

147 Waller, I. Zur Frage der Einwirkung der Wärmebewegung auf die Interferenz von Röntgenstrahlen. *Zeitschrift für Physik A Hadrons and Nuclei* **17**, 398-408, (1923).

148 Debye, P. Interferenz von Röntgenstrahlen und Wärmebewegung. *Annalen der Physik* **348**, 49-92, (1913).

149 Roberts, S. A., Weichsel, A., Qiu, Y., Shelnutt, J. A., Walker, F. A. & Montfort, W. R. Ligand-Induced Heme Ruffling and Bent NO Geometry in Ultra-High-Resolution Structures of Nitrophorin 4. *Biochemistry* **40**, 11327-11337, (2001).

150 Weichsel, A., Andersen, J. F., Roberts, S. A. & Montfort, W. R. Nitric oxide binding to nitrophorin 4 induces complete distal pocket burial. *Nature Structural Biology* **7**, 551-554, (2000).

151 Maes, E. M., Weichsel, A., Andersen, J. F., Shepley, D. & Montfort, W. R. Role of Binding Site Loops in Controlling Nitric Oxide Release: Structure and Kinetics of Mutant Forms of Nitrophorin 4. *Biochemistry* **43**, 6679-6690, (2004).

152 Nienhaus, K., Maes, E. M., Weichsel, A., Montfort, W. R. & Nienhaus, G. U. Structural Dynamics Controls Nitric Oxide Affinity in Nitrophorin 4. *Journal of Biological Chemistry* **279**, 39401-39407, (2004).

153 Benabbas, A., Ye, X., Kubo, M., Zhang, Z., Maes, E. M., Montfort, W. R. & Champion, P. M. Ultrafast Dynamics of Diatomic Ligand Binding to Nitrophorin 4. *J. Am. Chem. Soc.* **132**, 2811-2820, (2010).

154 Maes, E. M., Roberts, S. A., Weichsel, A. & Montfort, W. R. Ultrahigh Resolution Structures of Nitrophorin 4: Heme Distortion in Ferrous CO and NO Complexes. *Biochemistry* **44**, 12690-12699, (2005).

155 Andersen, J. F. & Montfort, W. R. The Crystal Structure of Nitrophorin 2. *Journal of Biological Chemistry* **275**, 30496-30503, (2000).

156 Andersen, J. F., Ding, X. D., Balfour, C., Shokhireva, T. K., Champagne, D. E., Walker, F. A. & Montfort, W. R. Kinetics and Equilibria in Ligand Binding by Nitrophorins 1-4: Evidence for Stabilization of a Nitric Oxide-Ferriheme Complex through a Ligand-Induced Conformational Trap. *Biochemistry* **39**, 10118-10131, (2000).

157 Ascenzi, P., Nardini, M., Bolognesi, M. & Montfort, W. R. Nitrophorins: Lipocalin-based heme proteins transporting nitric oxide. *Biochem Mol Biol Educ* **30**, 68-71, (2002).

158 Martí, M. A., Estrin, D. A. & Roitberg, A. n. E. Molecular Basis for the pH Dependent Structural Transition of Nitrophorin 4. *J Phys Chem B* **113**, 2135-2142, (2009).

159 Menyhárd, D. K. & Keserü, G. M. Protonation state of Asp30 exerts crucial influence over surface loop rearrangements responsible for NO release in nitrophorin 4. *FEBS Letters* **579**, 5392-5398, (2005).

160 Bertini, I., Luchinat, C. & Parigi, G. Paramagnetic constraints: An aid for quick solution structure determination of paramagnetic metalloproteins. *Concepts Magn Reson* **14**, 259-286, (2002).

161 Pintacuda, G., John, M., Su, X.-C. & Otting, G. NMR Structure Determination of Protein-Ligand Complexes by Lanthanide Labeling. *Acc. Chem. Res.* **40**, 206-212, (2007).

162 Mayo, B. C. Lanthanide shift reagents in nuclear magnetic resonance spectroscopy. *Chem Soc Rev* **2**, 49-74, (1973).

163 Harden, M. M. & Richard, E. R. Isotropic Nuclear Resonance Shifts. *J Chem Phys* **29**, 1361-1365, (1958).

164 Astashkin, A. V., Raitsimring, A. M. & Walker, F. A. Two- and four-pulse ESEEM studies of the heme binding center of a low-spin ferriheme protein: the importance of a multi-frequency approach. *Chemical Physics Letters* **306**, 9-17, (1999).

165 Muchmore, D. C., McIntosh, L. P., Russell, C. B., Anderson, D. E., Dahlquist, F. W., Norman, J. O. & Thomas, L. J. in *Methods in Enzymology* Vol. Volume 177 44-73 (Academic Press, 1989).

166 Kumar, S. & Bansal, M. Geometrical and Sequence Characteristics of α-Helices in Globular Proteins. *Biophysical Journal* **75**, 1935-1944, (1998).

167 Riordan, J., McElvany, K. & Borders, C. Arginyl residues: anion recognition sites in enzymes. *Science* **195**, 884-886, (1977).

168 Habenstein, B., Wasmer, C., Bousset, L., Sourigues, Y., Schütz, A., Loquet, A., Meier, B., Melki, R. & Böckmann, A. Extensive de novo solid-state NMR assignments of the 33 kDa C-terminal domain of the Ure2 prion. *Journal of Biomolecular NMR* **51**, 235-243, (2011).

169 Moreira, M. n. F., Coelho, H. S. L., Zingali, R. B., Oliveira, P. L. & Masuda, H. Changes in salivary nitrophorin profile during the life cycle of the blood-sucking bug Rhodnius prolixus. *Insect Biochemistry and Molecular Biology* **33**, 23-28, (2003).

170 Ribeiro, J. M. C. & Garcia, E. S. The Role of the Salivary Glands in Feeding in Rhodnius Prolixus. *Journal of Experimental Biology* **94**, 219-230, (1981).

171 Ambrus, A., Friedrich, K. & Somogyi, Á. Oligomerization of nitrophorins. *Anal. Biochem.* **352**, 286-295, (2006).

172 LeMaster, D. M. Deuterium labelling in NMR structural analysis of larger proteins. *Quarterly Reviews of Biophysics* **23**, 133-174, (1990).

173 Otten, R., Chu, B., Krewulak, K. D., Vogel, H. J. & Mulder, F. A. A. Comprehensive and Cost-Effective NMR Spectroscopy of Methyl Groups in Large Proteins. *Journal of the American Chemical Society* **132**, 2952-2960, (2010).

174 LeMaster, D. M. & Kushlan, D. M. Dynamical Mapping of E. coli Thioredoxin via ^{13}C NMR Relaxation Analysis. *Journal of the American Chemical Society* **118**, 9255-9264, (1996).

175 Hong, M. & Jakes, K. Selective and extensive ^{13}C labeling of a membrane protein for solid-state NMR investigations. *Journal of Biomolecular NMR* **14**, 71-74, (1999).

176 Higman, V., Flinders, J., Hiller, M., Jehle, S., Markovic, S., Fiedler, S., van Rossum, B.-J. & Oschkinat, H. Assigning large proteins in the solid state: a MAS NMR resonance assignment strategy using selectively and extensively ^{13}C-labelled proteins. *Journal of Biomolecular NMR* **44**, 245-260, (2009).

177 Reif, B. & Griffin, R. G. ^{1}H detected ^{1}H,^{15}N correlation spectroscopy in rotating solids. *Journal of Magnetic Resonance* **160**, 78-83, (2003).

178 Chevelkov, V., van Rossum, B. J., Castellani, F., Rehbein, K., Diehl, A., Hohwy, M., Steuernagel, S., Engelke, F., Oschkinat, H. & Reif, B. ^{1}H Detection in MAS Solid-State NMR Spectroscopy of Biomacromolecules Employing Pulsed Field Gradients for Residual Solvent Suppression. *Journal of the American Chemical Society* **125**, 7788-7789, (2003).

179 Paulson, E. K., Morcombe, C. R., Gaponenko, V., Dancheck, B., Byrd, R. A. & Zilm, K. W. Sensitive High Resolution Inverse Detection NMR Spectroscopy of Proteins in the Solid State. *Journal of the American Chemical Society* **125**, 15831-15836, (2003).

180 Reif, B., Jaroniec, C. P., Rienstra, C. M., Hohwy, M. & Griffin, R. G. ^{1}H-^{1}H MAS correlation spectroscopy and distance measurements in a deuterated peptide. *Journal of Magnetic Resonance* **151**, 320-327, (2001).

181 Reif, B., van Rossum, B. J., Castellani, F., Rehbein, K., Diehl, A. & Oschkinat, H. Characterization of ^{1}H−^{1}H Distances in a Uniformly 2H,15N-Labeled SH3 Domain by MAS Solid-State NMR Spectroscopy. *Journal of the American Chemical Society* **125**, 1488-1489, (2003).

182 Paulson, E. K., Morcombe, C. R., Gaponenko, V., Dancheck, B., Byrd, R. A. & Zilm, K. W. High-Sensitivity Observation of Dipolar Exchange and NOEs between Exchangeable Protons in Proteins by 3D Solid-State NMR Spectroscopy. *Journal of the American Chemical Society* **125**, 14222-14223, (2003).

183 Chevelkov, V., Faelber, K., Diehl, A., Heinemann, U., Oschkinat, H. & Reif, B. Detection of dynamic water molecules in a microcrystalline sample of the SH3 domain of α-spectrin by MAS solid-state NMR. *Journal of Biomolecular NMR* **31**, 295-310, (2005).

184 Hologne, M., Faelber, K., Diehl, A. & Reif, B. Characterization of Dynamics of Perdeuterated Proteins by MAS Solid-State NMR. *Journal of the American Chemical Society* **127**, 11208-11209, (2005).

185 Hologne, M., Chen, Z. & Reif, B. Characterization of dynamic processes using deuterium in uniformly ^{2}H,^{13}C,^{15}N enriched peptides by MAS solid-state NMR. *Journal of Magnetic Resonance* **179**, 20-28, (2006).

186 Reif, B., Xue, Y., Agarwal, V., Pavlova, M. S., Hologne, M., Diehl, A., Ryabov, Y. E. & Skrynnikov, N. R. Protein Side-Chain Dynamics Observed by Solution- and Solid-State NMR: Comparative Analysis of Methyl ^{2}H Relaxation Data. *Journal of the American Chemical Society* **128**, 12354-12355, (2006).

187 Hologne, M., Chevelkov, V. & Reif, B. Deuterated peptides and proteins in MAS solid-state NMR. *Progress in Nuclear Magnetic Resonance Spectroscopy* **48**, 211-232, (2006).

188 Linser, R., Fink, U. & Reif, B. Assignment of Dynamic Regions in Biological Solids Enabled by Spin-State Selective NMR Experiments. *Journal of the American Chemical Society* **132**, 8891-8893, (2010).

189 Etzkorn, M., Martell, S., Andronesi, O. C., Seidel, K., Engelhard, M. & Baldus, M. Secondary Structure, Dynamics, and Topology of a Seven-Helix Receptor in Native Membranes, Studied by Solid-State NMR Spectroscopy. *Angewandte Chemie International Edition* **46**, 459-462, (2007).

190 Tian, Y., Chen, L., Niks, D., Kaiser, J. M., Lai, J., Rienstra, C. M., Dunn, M. F. & Mueller, L. J. J-Based 3D sidechain correlation in solid-state proteins. *Physical Chemistry Chemical Physics* **11**, 7078-7086, (2009).

191 Chen, L., Kaiser, J. M., Polenova, T., Yang, J., Rienstra, C. M. & Mueller, L. J. Backbone Assignments in Solid-State Proteins Using J-Based 3D Heteronuclear Correlation Spectroscopy. *Journal of the American Chemical Society* **129**, 10650-10651, (2007).

192 Tang, M., Waring, A. J., Lehrer, R. I. & Hong, M. Effects of Guanidinium–Phosphate Hydrogen Bonding on the Membrane-Bound Structure and Activity of an Arginine-Rich Membrane Peptide from Solid-State NMR Spectroscopy. *Angewandte Chemie International Edition* **47**, 3202-3205, (2008).

193 Tang, M., Waring, A. J. & Hong, M. Arginine Dynamics in a Membrane-Bound Cationic Beta-Hairpin Peptide from Solid-State NMR. *ChemBioChem* **9**, 1487-1492, (2008).

194 Tang, M., Waring, A. J. & Hong, M. Phosphate-Mediated Arginine Insertion into Lipid Membranes and Pore Formation by a Cationic Membrane Peptide from Solid-State NMR. *Journal of the American Chemical Society* **129**, 11438-11446, (2007).

195 Herce, H. D. & Garcia, A. E. Molecular dynamics simulations suggest a mechanism for translocation of the HIV-1 TAT peptide across lipid membranes. *Proceedings of the National Academy of Sciences* **104**, 20805-20810, (2007).

196 Tang, M., Waring, A. J. & Hong, M. Effects of arginine density on the membrane-bound structure of a cationic antimicrobial peptide from solid-state NMR. *Biochimica et Biophysica Acta (BBA) - Biomembranes* **1788**, 514-521, (2009).

197 Knight, M. J., Felli, I. C., Pierattelli, R., Bertini, I., Emsley, L., Herrmann, T. & Pintacuda, G. Rapid Measurement of Pseudocontact Shifts in Metalloproteins by Proton-Detected Solid-State NMR Spectroscopy. *Journal of the American Chemical Society* **134**, 14730-14733, (2012).

198 Orwick, M. C., Judge, P. J., Procek, J., Lindholm, L., Graziadei, A., Engel, A., Gröbner, G. & Watts, A. Detergent-Free Formation and Physicochemical Characterization of Nanosized Lipid–

Polymer Complexes: Lipodisq. *Angewandte Chemie International Edition* **51**, 4653-4657, (2012).

199 Orwick-Rydmark, M., Lovett, J. E., Graziadei, A., Lindholm, L., Hicks, M. R. & Watts, A. Detergent-Free Incorporation of a Seven-Transmembrane Receptor Protein into Nanosized Bilayer Lipodisq Particles for Functional and Biophysical Studies. *Nano Letters* **12**, 4687-4692, (2012).

7 Acknowledgements

I would like to express my sincere and heartfelt acknowledgments to all the people who have been with me during my doctoral research life.

First of all, I would like to express my sincere gratitude to Prof. Dr. Henrike Heise who introduced me to the world of NMR, especially in the area of solid-state NMR. I am thankful to her for the courage and trust that she has shown to me for welcoming me as a newbie to the solid-state NMR group and sharing her in-depth knowledge in the various fields of NMR. She taught me the very basics of NMR, and I will always be respectful for her sincere efforts for helping me to broaden my knowledge in the field of biomolecular solid-state NMR. Her guidance and supervision has always helped me during my entire research life to be an independent researcher.

I would also like to thank Prof. Dr. Jörg Pietruszka and the rest of the members of my Ph.D examination committee Prof. Dr. Claus Seidel, Dr. Birgit Strodel and Dr. Jörg Labahn for the careful and thorough evaluation of my Ph. D thesis.

I would like to thank Dr. Markus Knipp from the “Max Planck Institute for Bioinorganic Chemistry” for sharing his profound knowledge in heme proteins, especially in the case of Nitrophorin 7 and also for allowing me to work under his guidance in MPI. He was always patient enough to answer my questions related to nitrophorins and has helped me a lot to gain more knowledge about NP7. At this point, I express my gratitude to Chunmao He, Johanna Taing and Yvonne Brandenburger for their technical assistance during my visit at the MPI for sample preparation.

Many thanks to Prof. Dr. Dieter Willbold for giving me an opportunity to be a part of his group and allowing me to collaborate with the members of the solution-state NMR. Here, I would also like to thank rest of the members of the solution-state NMR group especially Dr. Rudolf Hartmann for helping me with his technical and scientific experience in the field of

NMR. I would also like to thank Dr. Victor Pacheco for the DOSY measurements and also for helping with the interpretation of the DOSY results. I would also like to thank the rest of the members of the solution-state NMR, especially Dr. Justin Lecher for his technical assistance in solving software related problems.

I would also like to thank all the members of the "Familie Heise" Henrik, Santhosh, Timo, Hoa, Lisa and Claudia for sharing their scientific knowledge and also for creating a nice family atmosphere. Special thanks to my office mates Henrik and Timo for their sincere efforts to improve my communication skills in Deutsch. I would also like to thank the new member of the family, Dr. Manuel Etzkorn for sharing his experiences and knowledge in the areas of biomolecular NMR.

Many thanks to Forschungszentrum Juelich and Heinrich-Heine Universität Düsseldorf for providing me the financial support and lab space for conducting my research work in an ambient scientific atmosphere.

Words and pages would not be sufficient enough to express my sincere thanks to all my friends who have been with me during my difficult timings. Here, I express my sincere thanks to all my friends who helped me with their kind words and deeds.

I am grateful to my parents for the constant support and care that they have showered on me during the different stages of my life. I am deeply indebted to my brothers Jose and especially Babu for his continuous support and motivation in the pursuit of my scientific research in the absence of my father. I am also thankful to my sisters for their prayers and moral support.

Above all, the proper folding and functioning of a protein requires the interplay between various counteracting forces and I will be always thankful to an omnipotent force which governs the stability and the dynamics of this entire Omniverse.

Declaration

I hereby declare that this dissertation was produced autonomously and independently and without using any unauthorized help. This dissertation has not been handed in another institution or university. I do not have any unsuccessful attempts of obtaining a doctoral degree.

Sabu Varghese,
Juelich, 22.11.2012